University of Alberta

Weibull Analysis of Loading Rate Effect on
the Toughening Mechanisms of ABS

by

Jie Xu

A thesis submitted to the Faculty of Graduate Studies and Research
in partial fulfillment of the requirements for the degree of

Master of Science

Department of Mechanical Engineering

Fall, 2009
Edmonton, Alberta

Examining Committee

Supervisor

Dr. P.-Y. Ben Jar, Mechanical Engineering

Committee Chair

Dr. Xiaodong Wang, Mechanical Engineering

Committee Members

Dr. Tian Tang, Mechanical Engineering

Dr. Derek Martin, Civil Engineering

ABSTRACT

Rubber-toughened polymers have extensive applications due to excellent mechanical performances. However, the toughening mechanisms are not completely understood, as current study approaches are too localized for quantitative analysis and deviation from mechanical testing has rarely been taken into consideration.

In this study, Weibull statistics is applied to quantify the involvement of crazing and shear yielding mechanisms in poly(acrylonitrile butadiene styrene) (ABS) under tensile loading. Different loading rates were used to vary the involvement of each mechanism. In monotonic loading tests, the dominant deformation mechanism switches from crazing to shear yielding with the increase of crosshead speed. Crazing-dominant toughness values show narrow data scattering while those for shear yielding a broad distribution. The involvement of the deformation mechanisms can be varied through multi-stage loading at different crosshead speeds. Results from the study suggested that the Weibull analysis has the potential for quantifying the roles of various mechanisms in the deformation process.

ACKNOWLEDGEMENTS

I am particularly indebted to my supervisor Dr. P.-Y. Ben Jar for the guidance and financial support throughout this study.

I also would like to thank Mr. Bernie Faulkner and Ms. Tuula Hilvo for their constant technical supports, help in the lab and some valuable discussions.

Appreciation is extended to group members and ex-members of the Failure and Material Engineering Lab: Chengye Fan, Tik Man Dick, Riski Adianto, Paul Khosathit and Souvenir Muhammad for their friendship and the positive group environment.

Special thanks go to “The 2009 Joint ASCE-ASME-SES Conference on Mechanics and Materials” for the opportunity to present the research outcome, and to Department of Mechanical Engineering, Graduate Students’ Association and Faculty of Graduate Studies and Research for the financial assistance on the research and on the conference travel.

Finally, gratitude is given to my parents, Zongzheng Xu and Shumin Tian, for their care and support throughout my study.

TABLE OF CONTENT

LIST OF TABLES

LIST OF FIGURES

Chapter 1 Introduction

A polymer molecule is composed of repeating structural units typically connected by covalent bonds with molecular weight over 10,000 g/mol. Ever since early 19th century, the works on polymer science and engineering revolve modification and enhancement of natural and synthetic polymers. The understanding of microstructure and its strong influence on the bulk material properties were of interest, too. Till today, most commercially important polymers are entirely synthetic, which find applications in nearly every area of industry, such as construction components, aircraft, home appliance, semiconductors, adhesives, lubricants, etc.

One common classification of polymers is to divide them into thermoplastics and thermosets. A thermoplastic is a polymer that turns to liquid when heated, and freezes to a very glassy state when cooled sufficiently. A thermosetting polymer, on the other hand, forms covalent bonds through a cross-linking process known as a curing process, and cannot be remelted and remoulded.

Polymers are also defined as “brittle” or “ductile” considering the amount of deformation upon failure. Brittle polymers show limited deformation before failure and their load-displacement curves usually exhibit a proportional relationship. Brittle failures involve little plastic deformation, thus absorb a very low level of energy. On the other hand, ductile polymers have the ability to undergo significant deformation and absorb a large amount of energy before failure. However, the definition of “brittle” or “ductile” is not absolute for a polymer. Generally, a ductile-brittle transition temperature (DBTT) exists for a polymer, representing the temperature at which the deformation or fracture energy changes dramatically due to change of the deformation behaviour. For amorphous and semi-crystalline thermoplastics, the concept of DBTT can be understood in light of the glass transition temperature, T_g, below which the polymer is in a glassy state with relatively large stiffness. When T_g is approached or exceeded, the polymer chains can stretch or slide easily under loading, thus increasing the level of deformation and ductility.

In load-bearing applications, ductility and extensive plastic deformation are valued. Therefore, brittle polymers such as thermoplastics below their T_g need to be engineered to enhance their toughness. A good way of achieving this is to copolymerize elastomeric chains in the form of a dispersed phase. The technique is known as rubber toughening. Since modulus of the rubber component is usually much lower than the glassy thermoplastic, rubber toughening may come with a price of stiffness reduction.

This study is concerned about the deformation behaviour generated by a rubber-toughened polymer, poly(acrylonitrile butadiene styrene) (ABS). A method that quantifies the deformation mechanisms involved in the fracture process, thus the change of ductility, is developed from this study.

In this thesis, Chapter 1 provides an introduction and motivation to the study. This chapter contains literature review of related topics, toughening mechanisms of rubber-toughened polymers, loading rate effect and conventional study techniques. Chapter 2 provides knowledge background of the most important analysis tool in this study, i.e. Weibull distributions, which includes their formulation, determination of the parameters in the distribution models and the effects of those parameters. Chapter 3 describes experimental details. The material ABS will be further introduced. The test and specimen specifications follow ASTM standard for tensile tests of plastic materials. The operation and control of the material testing system (MTS) and the test procedures are given in details. In Chapter 4, test results are presented and discussed, followed by Weibull analysis and results. The conclusions of the study, as well as the recommendations for the future study will be given in Chapter 5.

1.1 Literature Review

1.1.1 Toughening mechanisms of rubber-toughened polymers

Sultan and co-workers [1, 2] were among the first researchers to show that the toughness of a polymer could be improved by the incorporation of rubber particles.

The practice of rubber toughening of polymers has been successfully carried out since then and has led to many diverse engineering polymers.

The mechanisms involved in the deformation process of rubber-toughened polymers have long been studied and at least thirteen different toughening mechanisms have been proposed as being responsible for the toughness enhancement [3]. One of the most important toughening mechanisms is crazing [4-13]. Crazing is a frequent damage phenomenon in glassy thermoplastic polymers. It is the formation of crazes in regions of high hydrostatic stress status. Crazes are microvoids that contain small interconnected fibrils. This void-fibril structure was first visualized by Kambour and Russell [6] using transmission electron microscopy (TEM). Crazes are different from cracks in that the former can contribute to the load support. When strained sufficiently, the fibril bridges will elongate and break before the microvoids grow and coalesce to form cracks. Crazing, the process of craze formation and growth, effectively absorbs a great amount of energy, therefore increasing the toughness of the polymer. Crazing does precede fracture in some glassy thermoplastic polymers, but only to a limited extent. The existence of the rubber particles provides numerous spots associated with stress concentrations and flaws, thus promoting craze formation to increase the energy absorption in the fracture process. Another important mechanism involved in the deformation process of rubber-toughened polymers is shear yielding [1, 14-19]. In this case, when global yielding occurs, deformation will develop in the form of shear flow in an inclined direction with respect to the applied tensile or compressive loading. One of the main differences between shear yielding and crazing is that the former does not change overall volume while the latter increases the volume. In addition, a typical phenomenon associated with shear yielding is “local thinning” or “necking”, while crazing tends to spread relatively uniformly throughout the material. Furthermore, since crazes break down to form cracks rather easily, the crazing-dominant failures tend to show a brittle response. On the other hand, shear yielding is usually associated with ductile behaviour. Other mechanisms such as rubber particle cavitation [20-26], energy absorption through rubber deformation [27, 28], crack branching caused by rubber particles [29] and crack termination at rubber

particles [30] were also observed in the rubber-toughened polymers and new deformation mechanisms are still being discovered [31].

For many rubber-toughened polymers, more than one toughening mechanisms may be involved in the deformation process. They interact with each other, sometimes with the dominant mechanism changing from one to another, by a series of factors, from test conditions such as temperature and strain rate, to material compositions such as particle size and distribution [30]. A huge amount of research works have been done in this field. Bucknall and Smith [5] showed that crazing in the polystyrene phase is the main mechanism of energy absorption in high-impact polystyrene (HIPS) while shear yielding and crazing both contribute to the toughness of ABS [30]. Bucknall also provided a framework of rubber toughening mechanisms through review of the existing models for rubber particle cavitation, shear yielding and craze growth in polymers [32]. Takahashi [33] revealed the craze healing stages in ABS/MMA sheets and indicated that the healing rate was influenced by the magnitude of plastic strain to which the specimens were subjected. Cheng et al. [34] studied the cooperative cavitation behaviour of rubber-toughened polycarbonate and found that the growth of the cavitation domain could be arrested when shear yielding of the matrix provides an alternative mechanism for relief of strain energy. Jansen et al. [35] investigated the influence of strain rate on the microscopic deformation mechanisms of a rubber/PMMA system and pointed out that the key for toughness improvement is the degree of cavitation formation, which induces shear yielding. An optimum amount of cavitation was identified with the variation of strain rate. Jang [36] examined the temperature and deformation rate effects on crazing and shear-type yielding damage in rubber-modified polypropylene (PP) and showed that the ductility and toughness lie in the competition between catastrophic crack propagation and the degree of plastic deformation through crazing and shear yielding. Wellinghoff and Baer [37] observed a “shear to craze” transition as a function of temperature in a number of vinyl polymers and arylene polymers, with crazing being favoured at elevated temperatures. Starke et al. [38] also studied the deformation mechanisms in rubber-toughened PSAN with core-shell particles over a range of temperatures, and

discovered that a transition in the deformation behavior from crazing to shear yielding occurs as the temperature increases. Jar et al. [39] suggested that for styrene-N-phenylmaleimide-modified ABS the rubber particle cavitation and matrix shear deformation are the main deformation mechanisms in the tensile testing. But for the Izod specimens, extensive crazing replaces the shear deformation to be the dominant matrix deformation mechanism. Jansen et al. [40] studied the mode of microscopic deformation in rubber-modified poly(methyl methacrylate) (PMMA) during tensile deformation, and pointed out that the transition from crazing to shear yielding takes place as the rubber content increases. Zhou et al. [41] found that the deformation mechanisms involved in polymer blends depend on the composition of the blends. There exists a deformation transition from crazing to shear yielding with the change of PVC/SAN ratio. The blend with a SAN-rich system deforms via the formation of crazes while the blend of a PVC-rich system deforms via shear yielding. The transition from crazing to shear yielding results in the improvement of toughness. A study by He and Donald [42] showed that the rubber particle concentration has a significant influence on the craze density in rubber-toughened PMMA. The wealth of literature on the subject suggests that the microscopic deformation behaviour in rubber-toughened polymers is very complex. Although it has been studied by many groups for a few decades, the understanding of the level of toughening mechanisms involved in the fracture process is still ambiguous, and sometimes results reported are contradictory to each other.

1.1.2 Loading rate effect

Loading rate is one of the important factors to evaluate mechanical performance of polymers [43-51]. For example, in 1993, Cardwell and Yee [43], based on their study on a rubber-modified epoxy, found that not only the fracture toughness is rate-dependent, but also, an activation energy could be determined to predict the variation of fracture toughness with each temperature. In 2000, an unusual failure mode transition from brittle to ductile under a combined pressure and shear loading

was observed in polycarbonate (PC) and poly(methyl methacrylate) (PMMA) by Ravi-Chandar and co-workers [46], with a normal-stress dominated fracture mode at low loading rates and a shear-stress dominated shear band failure at high strain rates. Park et al. [50] studied the rate-dependent mode I fracture behavior of the amorphous poly(lactic acid) and found that the static toughness was higher than the impact counterpart, mainly owing to extensive multiple craze formation at the static rate.

For rubber-toughened polymers, loading rate has been found to affect the brittle-ductile transition process and the associated deformation mechanisms, thus having a major influence on the toughening phenomenon [32, 35, 52-54]. For instance, Beguelin and Kausch [53] pointed out that for the rubber-toughened PMMA, the deformation involves cavitation and the amount of cavitation increases with the increase of strain rate. Raghavan et al. [54] measured the fracture energy over a wide range of crosshead speeds, and found that the viscoelastic characteristics of the rubber-toughened polymers allow more crack-tip deformation at lower loading rate, thus increasing the toughness. Lowering the loading rate also increases stability of the crack growth, but this transition occurs over a very small range of the loading rate.

In some studies, the loading rate effect was found to be coupled with the temperature effect, especially at high loading rate, due to the involvement of glass transition. Williams and Hodgkinson [55] believed that the toughening effect at high loading rate is a result of heating of the material due to energy dissipation by the plastic deformation. Vukhanh and Yu's work [56] on the brittle-ductile transition in HIPS and Zytel ST-801 found that the change of loading rate affects the molecular relaxation process and the brittle-ductile transition temperature. The correlation between temperature and loading rate seems to be controlled by the molecular relaxation according to the Arrhenius equation [56, 57]. On the other hand, some researchers, such as Ravi-Chandar et al. [46], believed that thermal effect may not play a significant role in the failure mode transitions in polymers.

The maximum crosshead speed applied in our study, is 60mm/min (10^{-3}m/s), equivalent to a strain rate of 0.02s^{-1} considering the gauge length of our specimens. According to the investigation by Inberg et al. [58], this loading rate is insufficient to

cause any noticeable temperature increase in the specimens, and the maximum temperature measured was far from approaching the glass transition temperature of ABS [59]. This has been supported by Steenbrink et al. [60] who reported that the specimens fractured at this loading rate did not show any relaxation on the fracture surface. Therefore, we believe that the loading rate used in this study is low enough to exclude any possibility of significant adiabatic heating.

1.1.3 Conventional techniques

For the purpose of understanding the microstructure and deformation behaviour, the experimental studies on the rubber-toughened polymers and relevant composite materials rely largely on microscopy, including optical microscopy (OM), transmission electron microscopy (TEM) and scanning electron microscopy (SEM) [38, 53, 61-69]. The latter two techniques form images of high resolution from interaction of the electrons with the specimen. The first observations on the toughening mechanisms in multiphase plastics were made by Bucknall and Smith in 1965 [5], who used transmission optical microscopy of thin films to study the deformation behaviour of HIPS. Chen and Jan [62] studied the microstructure and the fracture behaviour of the rubber-toughened epoxy resin by both TEM and SEM. Moskala [63] identified the debonding of the rubber particles from matrix using SEM, and suggested that this dilatational process would relieve the triaxial stresses and enhance shear yielding of the matrix. Bernal et al. [65] investigated the toughening mechanisms of ABS under both static and dynamic loading conditions by SEM and TEM. Xu et al. [66] through in-situ TEM observations on polystyrene/low-density polyethylene (PS/LDPE) blends, found that multiple-crazing is the main deformation mechanism for toughening when LDPE constitutes the dispersed phase, whereas shear yielding becomes the major deformation mode when LDPE forms the continuous phase. Takahashi et al. [68] conducted impact tests on methylmethacrylate-butadiene-styrene resin and observed deformed rubber particles and voids in the TEM photographs of whitening area without any evidence of crazing.

The SEM analysis of Lach and co-workers [69] revealed three different types of deformation mechanisms in the poly(styrene-butadiene) block copolymer blends: coalescence of microvoids, shear flow and tearing. Other than OM, SEM and TEM, the atomic force microscopy (AFM) has also been applied to studying the morphology of rubber-toughened polymers [70-72].

The main concern of these microscopic observation techniques is that voids and other features might have been introduced when the sections were prepared from the test specimens, thus not representing true fracture behaviour. Another criticism is that the observation scope is too small to represent the general behaviour of bulk specimens. In order to counter these criticisms, other experimental techniques have been applied, such as small-angle X-ray scattering (SAXS) [26, 42, 73-80], volumetric strain measurements [22, 30, 81-86], light scattering [87, 88] and so on. SAXS is a technique to detect the shape and size of aggregates that cause scattering of the X-ray. In 1993, Ijichi et al. [74] used the technique and observed a diamond-like pattern in HIPS before the yield point. As the deformation proceeded beyond the yield point, a distinct streak perpendicular to the tensile direction arose and, therefore, the cross pattern was observed. Magalhaes and Borggreve [75] studied the deformation process in rubber-modified polystyrene by static SAXS on deformed tensile samples under loading. They found that matrix crazing has very minor contribution to the plastic deformation. With an increasing rubber content, the amount of crazing decreases significantly whereas the toughness increases. The main source of energy absorption for the plastic deformation might be cavitation-induced microscopic shear yielding. Sferrazza et al. [78] investigated in-situ tensile deformation of toughened PMMA by SAXS, and found that the dominant deformation mechanism depend on the concentration of the toughening particles. Jar et al. [79, 80] examined the deformation mechanisms in a high thermal resistant ABS using both TEM and SAXS, and provided new evidence for the coexistence of crazing and shear yielding. Since void-formation-associated deformation mechanisms such as crazing and particle cavitation induce dilatational volume change while shear yielding is believed to keep the volume constant, volumetric strain measurements, also known as dilatometry, was

used to quantitatively characterize the contribution of these deformation mechanisms in rubber-toughened polymers. In 1981, Maxwell and Yee [82] employed this technique in their study on the toughening mechanisms of rubber-modified polymers, and found that cavitation and shear yielding can both be observed over a range of strain rates, with the voiding being sensitive to the change of strain rate. The technique was also used in the work by Nair, Wong and Goettler [85] in order to understand the relative roles of cavitation and shear yielding in the blends of nylon 6, 6 and ABS. Xu and Tjong [86] obtained quantitative information through the dilatometric technique and found that there is a crazing-shear yielding transition with the increase of the HDPE content in the PS/HDPE blends.

The above techniques are able to provide information about deformation occurring in the bulk polymer, in the data form that represents the average behaviour over a large volume. In combination with the microscopic observations, they provide valuable insights to the deformation mechanisms involved in the rubber-toughened polymers. However, the uncertainties involved in the mechanical testing caused by either material defects or deviations of test conditions have rarely been concerned.

1.2 Objective and Scope of the Study

Due to possible defects and variation of testing conditions, the measured mechanical properties of rubber-toughened polymers often show some scattering. Sometimes, the data scattering is very large, thus accurate prediction on the mechanical performances becomes difficult. To this end, the idea of reliability must be introduced. Like the mechanical properties themselves, the reliability characteristics of the mechanical properties are of interest and the understanding of their relation with microstructure or microscopic deformation behaviour of the materials could be further pursued.

Overall, the objective of this study is to establish the effectiveness of using Weibull analysis to identify and quantify the contribution from each of multiple mechanisms in the deformation process of rubber-toughened polymers. The variation characteristics of material toughness will be determined for a rubber-toughened

polymer, poly(acrylonitrile butadiene styrene) (ABS), and their relation with the deformation mechanisms, crazing and shear yielding for ABS, will be investigated. For determining the variation features of material properties, repetitive tests have been done for each test condition. Different loading rate was applied to change the distribution characteristics of toughness in the monotonic tensile tests. Based on the results of monotonic tests, multi-stage tests were carried out to further demonstrate the ability of the proposed approach to quantify the contribution from each mechanism.

Chapter 2 Fundamentals of Weibull Distribution

Weibull distribution is a well known continuous probability distribution. It is also called the Rosin-Rammler distribution when used to describe the size distribution of particles. It was invented by Waloddi Weibull in 1937 and popularized by his significant works from 1939 to 1951. Weibull distribution is versatile, and its representation contains a good approximation of the normal distribution as well as the exact expressions of the exponential distribution and the Rayleigh distribution. Because Weibull distribution has the ability to provide reasonable accuracy with very small size of samples, it has a wide range of applications in life data analysis and engineering design. The fundamentals of Weibull distribution were well summarized in references [89, 93], which will be followed in this chapter up to section 2.5.

2.1 Formulations

The most commonly applied Weibull distribution is the two-parameter one, and its cumulative distribution function (CDF) is

$$F(t) = 1 - \exp\left[-\left(\frac{t}{\eta}\right)^{\beta}\right] \tag{2-1}$$

where $F(t)$ is the probability of failure up to lifetime t, or unreliability at t, in which $t \geq 0$ is the failure time. In our study, the ranges of material properties such as ultimate tensile strength, extension at break and material toughness are of interest, and they are the meaning of "lifetime" of the material. β and η are the shape and the scale parameters, respectively. The complement of the CDF is reliability, $R(t)$, expressed as

$$R(t) = \exp\left[-\left(\frac{t}{\eta}\right)^{\beta}\right] \tag{2-2}$$

By taking derivative of the CDF with respect to t, the probability density function

(PDF) can be determined

$$f(t)=\left(\frac{\beta}{\eta}\right)\left(\frac{t}{\eta}\right)^{\beta-1}\exp\left[-\left(\frac{t}{\eta}\right)^{\beta}\right] \tag{2-3}$$

The instantaneous failure rate (or hazard rate) is the rate of failure for the survivors up to t, and it can be defined as the ratio of PDF to reliability, namely

$$h(t)=\frac{f(t)}{R(t)}=\left(\frac{\beta}{\eta}\right)\left(\frac{t}{\eta}\right)^{\beta-1} \tag{2-4}$$

The shape parameter β controls the skewness of the probability density function of the Weibull distribution, and represents the slope in the Weibull probability plot, as to be discussed later. The scale parameter η represents the characteristic life of the Weibull distribution. By setting $t=\eta$ in the CDF,

$$F(t)=1-\exp\left[-\left(\frac{\eta}{\eta}\right)^{\beta}\right]=1-\exp(-1)=0.632$$

We see that η represents the time at which 63.2% of the sample units fail.

The Weibull mean μ, variance Var and standard deviation Std of the failure time can then be expressed in terms of the Weibull parameters

$$\mu=\eta\Gamma\left(1+\frac{1}{\beta}\right) \tag{2-5}$$

$$Var=\eta^2\left[\Gamma\left(1+\frac{2}{\beta}\right)-\Gamma^2\left(1+\frac{1}{\beta}\right)\right] \tag{2-6}$$

$$Std=\eta\left[\Gamma\left(1+\frac{2}{\beta}\right)-\Gamma^2\left(1+\frac{1}{\beta}\right)\right]^{1/2} \tag{2-7}$$

where the Gamma function is defined as

$$\Gamma(z)=\int_0^{\infty}y^{z-1}\exp(-y)\,dy \tag{2-8}$$

See Appendix 1 for the detailed derivation.

2.2 Median Ranks

For each failure time t_i from the ordered test data, a position of the corresponding unreliability F_i is needed for the Weibull analysis. However, its true percentage values are always unknown. If N is the sample size number and i the rank order number, the first attempt would be using i/N as an estimate. However, this will make the unreliability of the last point 100%. Alternative solutions such as $(i-1)/N$, $(i-0.5)/N$ and $i/(N+1)$ were also suggested.

Although all the estimates can be very close when the sample size number is reasonably large, the median ranks is the most popular approach for determining the plotting positions of F_i. The position given by the median ranks is the value that the true probability of failure should have at the ith failure out of a sample of N units at a confidence level of 50%, that is, the probability for at least the ith failure to have occurred is 50%. According to this definition, the estimate is based on a solution of a binomial equation and can be calculated for any confidence percentage, P, by solving the cumulative binomial equation for Z:

$$P = \sum_{k=i}^{N} \binom{N}{k} Z^k (1-Z)^{N-k} \tag{2-9}$$

The unreliability estimated by the median ranks is obtained by solving for Z at $P = 0.5$, namely

$$0.5 = \sum_{k=i}^{N} \binom{N}{k} Z^k (1-Z)^{N-k} \tag{2-10}$$

where $\binom{N}{k} = \frac{N!}{k!(N-k)!}$. The only input in the calculation above is the sample size number N and the rank order i, and the results for a variety of N and i and the confidence percentage P are well tabulated in relevant handbooks [89].

Solving the above cumulative binomial equation requires numerical methods due to the high order of the unknown variable. A straightforward and quick approximation

to the median ranks is suggested to be [90]

$$F_i = \frac{i - 0.3}{N + 0.4} \tag{2-11}$$

2.3 Parameter Determination

To determine the parameters β and η in the two-parameter Weibull distribution, Eqn. (2-1) is rearranged to a transformed scale to obtain a linear relation between $\ln\ln\left[\frac{1}{1-F(t)}\right]$ and $\ln(t)$:

$$F(t) = 1 - \exp\left[-\left(\frac{t}{\eta}\right)^{\beta}\right]$$

$$\frac{1}{(1-F(t))} = \exp\left[\left(\frac{t}{\eta}\right)^{\beta}\right]$$

$$\ln\left[\frac{1}{(1-F(t))}\right] = \left(\frac{t}{\eta}\right)^{\beta}$$

$$\ln\ln\left[\frac{1}{(1-F(t))}\right] = \beta\ln(t) - \beta\ln(\eta) \tag{2-12}$$

Denoting $\ln(t)$ as x, the scale on the abscissa, and $\ln\ln\left[\frac{1}{(1-F(t))}\right]$ as y, the scale on the ordinate, all data points (x_i, y_i) can be fitted using linear regression into a straight line on a x-y plot with the slope equal to β and intersect $-\beta\ln(\eta)$. Such a plot is called the Weibull probability plot.

Redefine the linear relation to be

$$x = ay + b \tag{2-13}$$

where the coefficients can be expressed in terms of the Weibull parameters as:

$$\begin{cases} a = \dfrac{1}{\beta} \\ b = \ln(\eta) \end{cases} \quad \text{or} \quad \begin{cases} \beta = \dfrac{1}{a} \\ \eta = \exp(b) \end{cases} \tag{2-14}$$

Minimum horizontal (vertical if regression on y) deviation of the data points from the straight line is pursued according to the least squares principle. Assume

$$x_i = ay_i + b + \varepsilon_i \tag{2-15}$$

and

$$\mathrm{E} = \sum_{i=1}^{N} \varepsilon_i^{\,2} = \sum_{i=1}^{N} \left(x_i - ay_i - b \right)^2 \tag{2-16}$$

To determine a and b for the minimum E value, E is differentiated with respect to a and b, respectively, and set equal to zero to yield

$$\begin{cases} \dfrac{\partial \mathrm{E}}{\partial a} = -2\sum\limits_{i=1}^{N} y_i \left(x_i - ay_i - b \right) = 0 \\ \dfrac{\partial \mathrm{E}}{\partial b} = -2\sum\limits_{i=1}^{N} \left(x_i - ay_i - b \right) = 0 \end{cases} \quad \text{or} \quad \begin{cases} \sum\limits_{i=1}^{N} y_i \left(x_i - ay_i - b \right) = 0 \\ \sum\limits_{i=1}^{N} \left(x_i - ay_i - b \right) = 0 \end{cases} \tag{2-17}$$

By solving the above equations simultaneously for the coefficients a and b, we have

$$a = \frac{N\sum\limits_{i=1}^{N} x_i y_i - \sum\limits_{i=1}^{N} x_i \sum\limits_{i=1}^{N} y_i}{N\sum\limits_{i=1}^{N} y_i^{\,2} - \left(\sum\limits_{i=1}^{N} y_i \right)^2} \tag{2-18}$$

$$b = \frac{\sum\limits_{i=1}^{N} x_i - a\sum\limits_{i=1}^{N} y_i}{N} \tag{2-19}$$

Hence β and η can be determined for the two-parameter Weibull distribution, and the correlation coefficient of the rank regression is given by [89]

$$\rho = \frac{N\sum\limits_{i=1}^{N} x_i y_i - \sum\limits_{i=1}^{N} x_i \sum\limits_{i=1}^{N} y_i}{\sqrt{N\sum\limits_{i=1}^{N} x_i^{\,2} - \left(\sum\limits_{i=1}^{N} x_i \right)^2} \sqrt{N\sum\limits_{i=1}^{N} y_i^{\,2} - \left(\sum\limits_{i=1}^{N} y_i \right)^2}} \tag{2-20}$$

in which ρ indicates the strength of linear relationship between the median ranks and the life data.

2.4 The Three-Parameter Weibull Distribution

In some cases, it may be physically impossible for the failure to occur early. A guaranteed failure free period exists within which the probability of failure is simply zero. Under such circumstances, the two-parameter Weibull distribution should be modified by introducing a location parameter (representing the guaranteed value or failure starting time) t_0 to form the three-parameter Weibull distribution. The CDF and the PDF of the three-parameter Weibull distribution are given by

$$F(t) = 1 - \exp\left[-\left(\frac{t-t_0}{\eta}\right)^{\beta}\right] \tag{2-21}$$

$$f(t) = \left(\frac{\beta}{\eta}\right)\left(\frac{t-t_0}{\eta}\right)^{\beta-1} \exp\left[-\left(\frac{t-t_0}{\eta}\right)^{\beta}\right] \tag{2-22}$$

for $t \geq t_0$. When $t_0 = 0$, these expressions reduce to those for the two-parameter Weibull distribution.

To determine the parameters, an appropriate correction of $x_i = \ln(t_i - t_0)$ is needed for the data points to acceptably fall on a straight line on the rectified Weibull probability plot. There are quite a few ways to estimate t_0 [91]. Here we follow the method given by Shigley [92] and introduce one of them in detail.

In order to determine the location parameter t_0 in the three-parameter Weibull distribution, $\ln\ln\left[\frac{1}{(1-F_i)}\right]$ is plotted against $\ln(t_i)$ in the Weibull probability plot, and a curve is drawn to fit the data points. Then, locations for three distinct points on the curve, (x_1, Y_1), (x_2, Y_2) and (x_3, Y_3), (note that they are not necessarily the data points) of equal space with respect to the ordinate are determined, as illustrated in Fig. 2.1. That is,

$$Y_2 - Y_1 = Y_3 - Y_2 = d \tag{2-23}$$

or

$$\ln\ln\left[\frac{1}{(1-F_2)}\right]-\ln\ln\left[\frac{1}{(1-F_1)}\right]=\ln\ln\left[\frac{1}{(1-F_3)}\right]-\ln\ln\left[\frac{1}{(1-F_2)}\right] \tag{2-24}$$

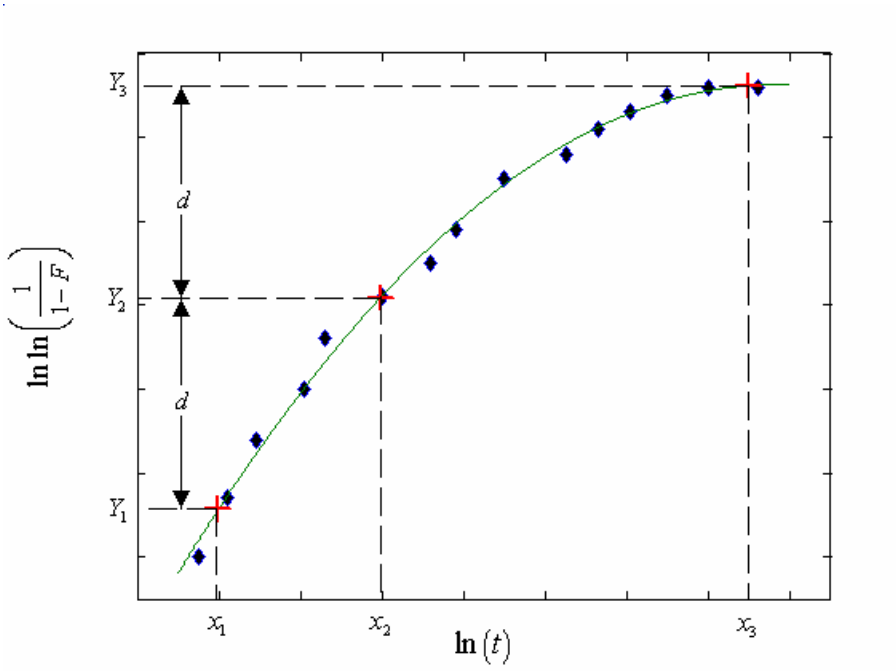

Fig. 2.1 Estimation of the location parameter t_0 for the three-parameter Weibull distribution

According to the relation implied by the three-parameter Weibull distribution

$$\ln\ln\left[\frac{1}{(1-F)}\right]=\beta\ln(t-t_0)-\beta\ln(\eta) \tag{2-25}$$

the abscissa of the three points should satisfy

$$\begin{aligned}&\left[\beta\ln(t_2-t_0)-\beta\ln(\eta)\right]-\left[\beta\ln(t_1-t_0)-\beta\ln(\eta)\right]\\&=\left[\beta\ln(t_3-t_0)-\beta\ln(\eta)\right]-\left[\beta\ln(t_2-t_0)-\beta\ln(\eta)\right]\end{aligned} \tag{2-26}$$

From this, through the following derivation, t_0 can be determined

$$\ln(t_2-t_0)-\ln(t_1-t_0)=\ln(t_3-t_0)-\ln(t_2-t_0)$$

$$\ln\left(\frac{t_2-t_0}{t_1-t_0}\right)=\ln\left(\frac{t_3-t_0}{t_2-t_0}\right)$$

$$\frac{t_2 - t_0}{t_1 - t_0} = \frac{t_3 - t_0}{t_2 - t_0}$$

$$t_0 = t_2 - \frac{(t_3 - t_2)(t_2 - t_1)}{(t_3 - t_2) - (t_2 - t_1)} = \frac{t_1 t_3 - t_2^{\,2}}{t_1 + t_3 - 2t_2} \tag{2-27}$$

After t_0 is determined, linear regression can be performed on

$$x_i = \ln(t_i - t_0)$$

$$y_i = \ln\ln\left(\frac{1}{1 - F_i}\right)$$

to determine the other two parameters, β and η. The procedure is exactly the same as that described for determining the parameters for the two-parameter Weibull distribution.

However, the above method for determining t_0 may be subjective due to the freedom of choosing curve and points, thus may not have sufficient accuracy. The calculation adopted by commercial softwares usually involves iteration on t_0 until the maximum correlation coefficient is reached. Weibull++ used in this study adopts the parameter iteration process of the three-parameter Weibull distribution based on an optimized Nelder-Mead algorithm [93, 94], and adjusts data points by this t_0 value to fall on a straight line.

2.5 Parameter Effect on the Weibull Distribution

2.5.1 Effect of the shape parameter β

The shape parameter β is dimensionless. It is also known as the slope in the Weibull probability plot. The value of β has a remarkable effect on the distribution behaviour. As a matter of fact, some values of β will reduce the Weibull distribution to other distributions. For example, when $\beta = 1$, the two-parameter Weibull

distribution becomes the one-parameter exponential distribution with the CDF being

$$F(t) = 1 - \exp\left(-\frac{t}{\eta}\right) \tag{2-28}$$

When $\beta = 2$, it is equivalent to the Rayleigh distribution. When the value of β is between 3 and 4, the PDF is approximately symmetric and it approaches the normal distribution. When β goes to infinity, the Weibull distribution approaches asymtotically to the Dirac delta function.

The following discussion on the effect of β is for values greater than 1, because if $\beta < 1$, the PDF $f(t) \to \infty$ as $t \to 0$ and with $\beta = 1$, $f(0)$ has a constant value of $\frac{1}{\eta}$.

The effects of the shape parameter β on the CDF, PDF and the failure rate function are illustrated in Fig. 2.2.

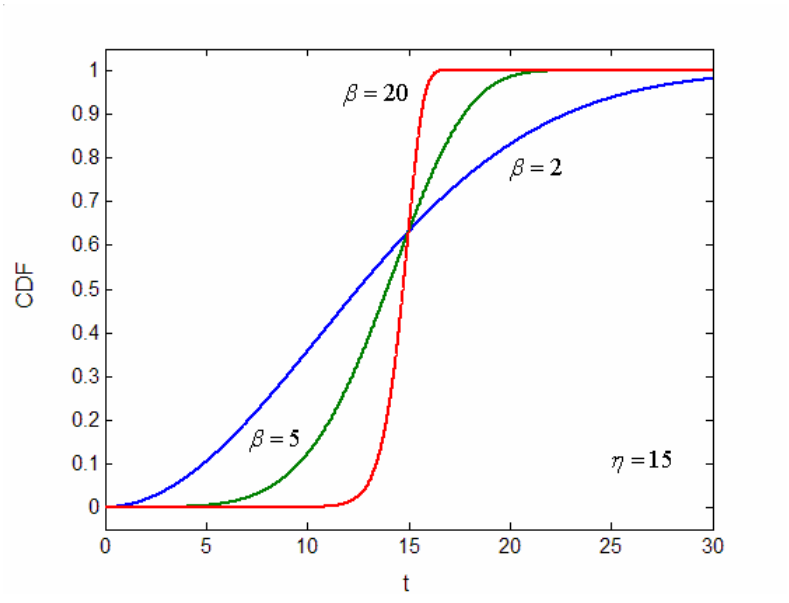

(a)

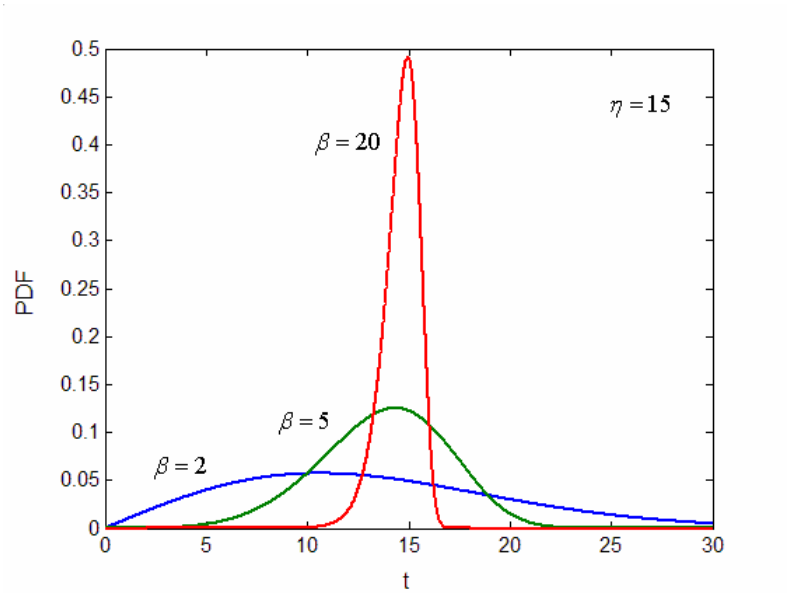

(b)

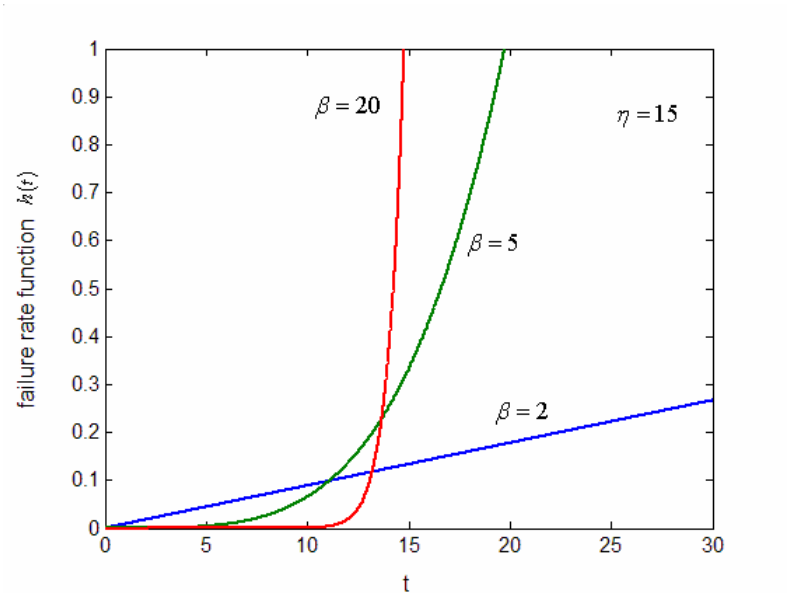

(c)

Fig. 2.2 Effects of the shape parameter β on (a) CDF, (b) PDF and (c) failure rate functions

As β increases, the steepness of the CDF curve rises with the point at CDF=0.632 fixed. With increase of β value, the peak of the PDF curve becomes high and

narrow. In addition, small β value results in the peak skewing to the left, and large β skews to the right. When β falls in the range between 2.6 and 3.7, the skewness of the PDF curve is approximately zero. One of the most important effects of β on the Weibull distribution is on the failure rate. Weibull distributions with $\beta < 1$ have a failure rate that decreases with time t, also known as infant or early-life failures. Weibull distributions with β close to or equal to 1 have a fairly constant failure rate, indicating useful life or random failures. Weibull distributions with $\beta > 1$ have a failure rate that increases with time, also known as wear-out failures. These comprise the three sections of the classic "bathtub curve" (Fig. 2.3). Note that in Fig. 2.3, the three sections of the "bathtub curve" do not necessarily share a continuous time scale. They simply represent the different failure features for the distributions corresponding to the different β values. For $\beta > 1$, the failure rate always increases with time t, indicating the mode of wear-out. When $\beta = 2$, the failure rate is positively proportional to t. When $\beta > 2$, the failure rate curve is convex, meaning the failure rate increases at an accelerating rate with t. As β increases further, the failure rate increases drastically. The failures can be further classified. When $1.0 < \beta < 4.0$, it implies early wear-out and when $\beta > 4.0$, it implies old age (rapid) wear-out. For the latter case, the CDF curve of the Weibull distribution is steep, and if the characteristic life is beyond the design life, the risk of failure before being worn out is much lowered. The extreme case where $\beta = \infty$ implies perfect design.

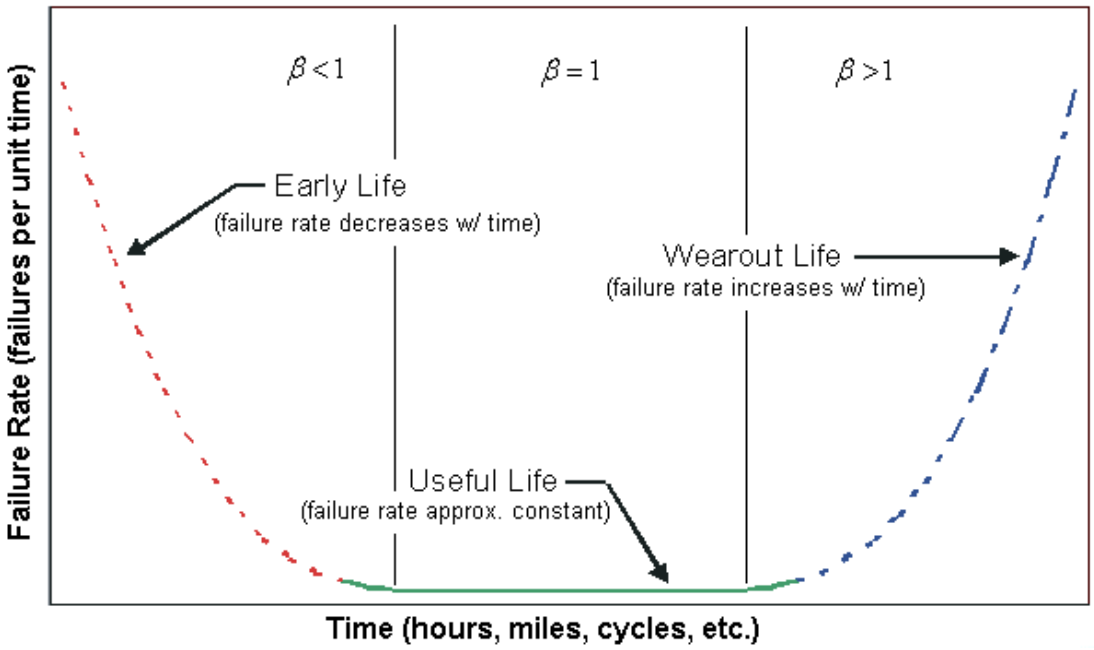

Fig. 2.3 "Bathtub curve"-effect of the shape parameter β on the failure rate function [95]

2.5.2 Effect of the scale parameter η

The scale parameter η represents the characteristic life in the two-parameter Weibull distribution. A change in η has the same effect on the distribution as a change of the abscissa scale, as illustrated in Fig. 2.4.

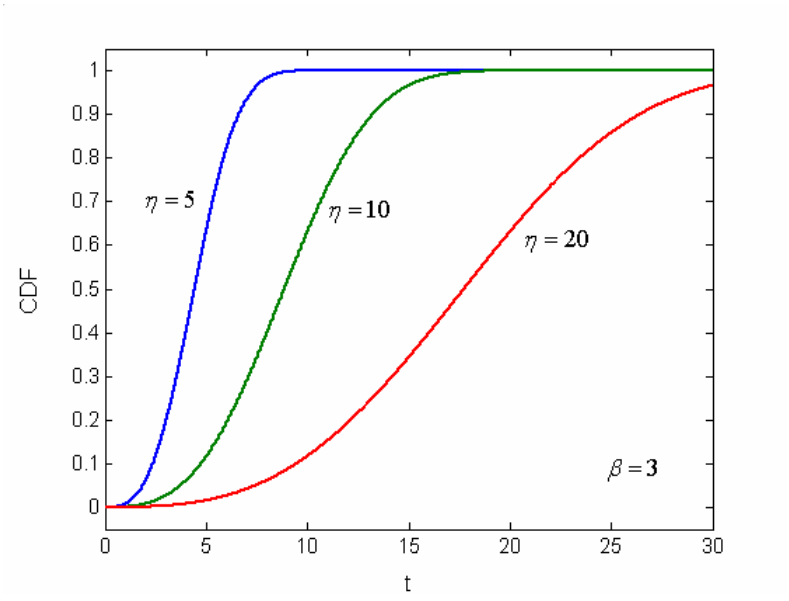

(a)

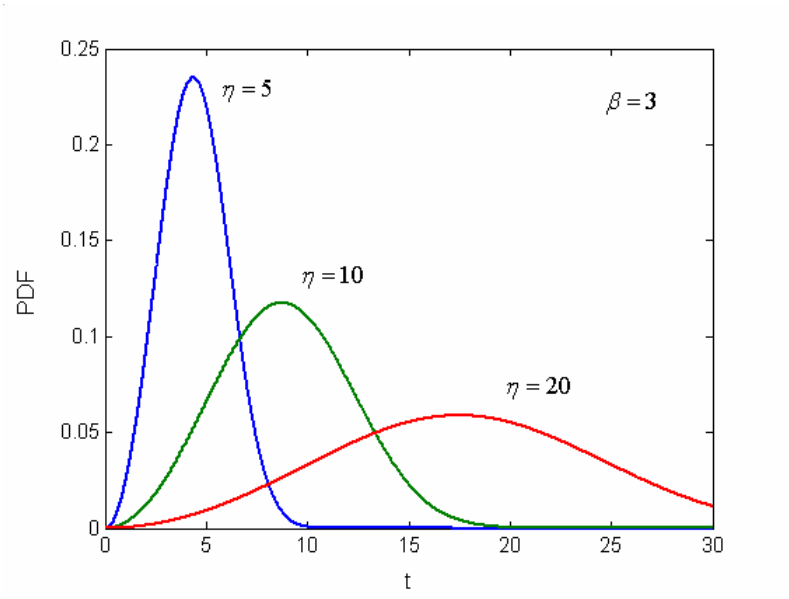

(b)

Fig. 2.4 Effects of the scale parameter η on (a) CDF and (b) PDF

Increasing the η value while holding β constant has an effect of straightening the CDF curve and making the steepness gentler. In the PDF plot, increasing η stretches out the PDF curve to the right. Since the area under a PDF curve is always equal to one, the peak of the PDF curve will also decrease with the increase of η.

2.5.3 Effect of the location parameter t_0

The location parameter t_0 simply has a shifting effect on both the CDF and the PDF of a Weibull distribution. It locates the range of the distribution along the abscissa (Fig. 2.5).

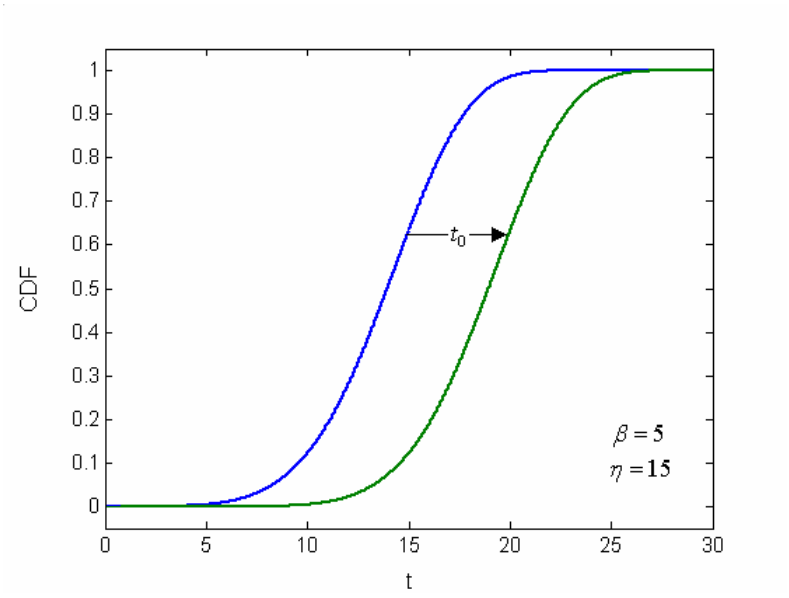

(a)

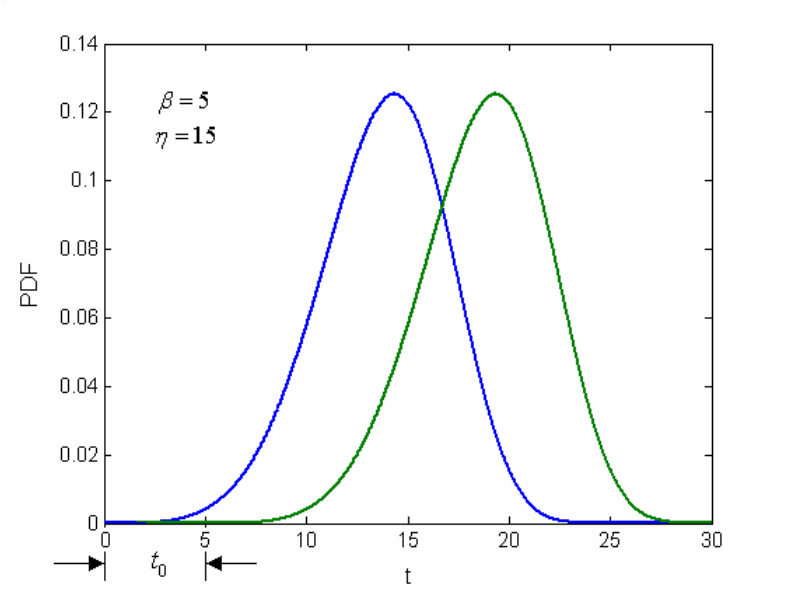

(b)

Fig. 2.5 Effects of the location parameter t_0 on (a) CDF and (b) PDF

When $t_0 = 0$, as in the two-parameter Weibull distribution, the distribution starts at the origin. When $t_0 \neq 0$, it introduces a horizontal translation t_0 to the distribution, and a physical justification is needed for the failure probability not starting at the origin. If $t_0 > 0$, it indicates a guaranteed failure free time. If $t_0 < 0$, it indicates the possibility of failure during production or fabrication which is before the design of being actually used.

2.6 The Mixed Weibull Distribution

The mixed Weibull distribution (also known as the multimodal Weibull distribution) is commonly used for describing distribution behaviour when there are multiple failure modes involved. It gives a global picture of life by mixing different Weibull distributions, or subpopulations. When each subpopulation is described by a two-parameter Weibull distribution, the CDF of the mixed Weibull distribution is

$$F(t) = \sum_{i=1}^{S} p_i F_i = \sum_{i=1}^{S} p_i \left\{ 1 - \exp\left[-\left(\frac{t}{\eta_i} \right)^{\beta_i} \right] \right\} = 1 - \sum_{i=1}^{S} p_i \exp\left[-\left(\frac{t}{\eta_i} \right)^{\beta_i} \right] \qquad (2\text{-}29)$$

And by taking derivative of $F(t)$ with respect to t, the PDF is obtained as

$$f(t) = \sum_{i=1}^{S} p_i f_i = \sum_{i=1}^{S} p_i \left(\frac{\beta_i}{\eta_i} \right) \left(\frac{t}{\eta_i} \right)^{\beta_i - 1} \exp\left[-\left(\frac{t}{\eta_i} \right)^{\beta_i} \right] \qquad (2\text{-}30)$$

where S is the number of failure modes, or the number of subpopulations, p_i is the mixing weight or portion for the ith subpopulation, and β_i and η_i are the corresponding shape parameter and scale parameter. The total number of model parameters is $3S - 1$ considering that the following condition has to be satisfied

$$\sum_{i=1}^{S} p_i = 1 \qquad (2\text{-}31)$$

Weibull++ realizes nonlinear regression by utilizing a modified Levenberg-Marquardt algorithm [96, 97] for the parameter determination in the mixed Weibull distribution.

Chapter 3 Experimental Details

3.1 Material

The material used in the study is poly(acrylonitrile butadiene styrene) (ABS), a typical rubber-toughened thermoplastic. Introduced commercially in the 1940s, ABS is synthesized through grafting of butadiene to styrene-acrylonitrile (SAN) copolymer. The molecular formulas of the three components are shown in Fig. 3.1. In the resulting polymer, most of the styrene and acrylonitrile form a continuous glassy matrix with the polybutadiene to form the dispersed spherical phase. The continuous phase of styrene-acrylonitrile is responsible for the strength, stiffness, rigidity and processability of the polymer. It also provides a shiny, impervious surface. The butadiene-riched dispersed phase provides the resilience and toughness even at low temperatures. A wide range of ABS materials can be formulated from different combinations of the above three components. The proportions can vary from 15% to 35% for acrylonitrile, 5% to 30% for butadiene and 40% to 60% for styrene. Desired material properties can be achieved through design of the components, often with the sacrifice of some others.

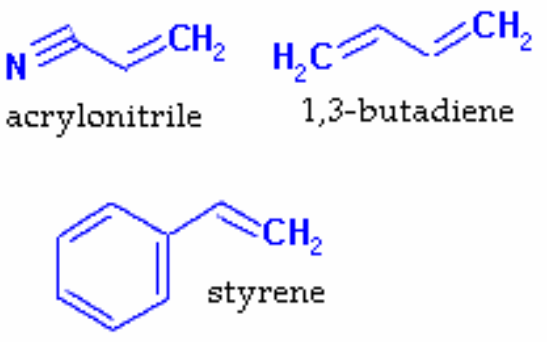

Fig. 3.1 Molecular structures of the three components of ABS [98]

Due to its excellent mechanical properties, ABS has extensive applications in piping, auto industry and home appliance.

As introduced in the literature review, crazing and shear yielding are found to be two principal toughening mechanisms involved in the deformation behaviour of ABS. In general, the roles of crazing and shear yielding in the deformation of rubber-toughened polymers vary with the component ratio and test conditions, such as temperature, strain rate, etc.

The ABS material used in this study is supplied by McMaster-Carr (Part Number: 8586K24) and some properties of the ABS product can be found on the supplier's website [99].

3.2 Specimen Preparation

The ABS panels provided by McMaster-Carr came in 3.2mm thick sheets (121.92×60.96 cm^2). They were firstly cut using table saw into rectangular strips of 195mm×19mm. Then the strips were fixed in a template and machined to tensile specimens using Tensilkut, model 10-33 (from Qualitest). Dimensions of the template follow the ASTM standard for tensile tests of plastics, as illustrated in Table 3.1. The configuration and dimensions of our machined specimens are shown in Fig. 3.2.

Table 3.1 ASTM standard for tensile specimen of plastics (D638, Type I), unit: mm

gauge length	50
distance between grips	115±5
length of narrow parallel-sided portion	57±0.5
overall length	≥165
width of narrow portion	13±0.5
width at ends	19±0.4
thickness	3.2±0.4
radius of fillet	76±1

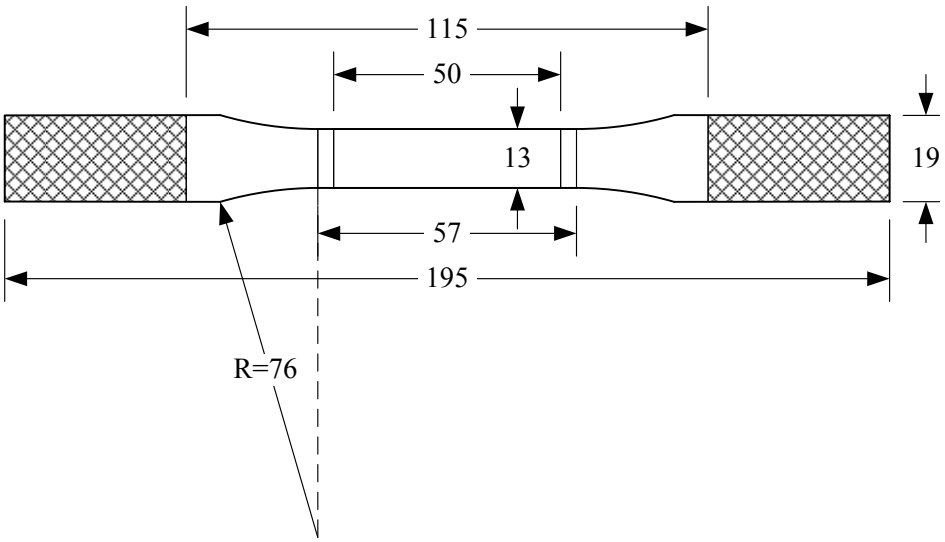

Fig. 3.2 Configuration and dimensions of an ABS tensile specimen (unit: mm)

The cutting was done by fixing the rectangular strip to the template, and then pushing the template against the guide bar of Tensilkut. Given the specimen thickness and the fact that ABS is a plastic material, the machining can be done by cutting once on each side of the specimen. The high speed rotation of the cutting bit at around 17,000 RPM is suitable for machining soft materials like plastics and does not cause melting. The Tensilkut machine was hooked up to a vacuum chamber to prevent the debris from building up on or near the cutting bit.

The machined surfaces were then polished using sandpapers, 400 Grit first and then 600 Grit, to improve the surface smoothness. The polishing reduced the possibility of defects and potential stress concentration caused by the machining. The gripping positions were marked on each specimen and the dimensions of the cross section within the gauge length were recorded before the testing.

3.3 Mechanical Testing

3.3.1 Test equipment and control

Both monotonic tests and multi-stage tensile tests were carried out on a hydraulic MTS machine (Material Testing System, Model 810) (Fig. 3.3) at room temperature and pressure. According to the material used and the thickness of the specimens, wedge grips of Model 647.10A were used at a gripping pressure of 2.8 MPa.

Fig. 3.3 MTS material testing system and tensile test setup

When mounting the specimens, the MTS machine was set in the stroke control mode. An alignment jig was applied on both the upper and lower grips to ensure that the specimen was placed vertically. The specimen was gripped at the upper side first. Then the load was set to zero before the lower grip was engaged. Note that before

engaging the lower grip, the CLC control mode was selected to be able to monitor both load and stroke readings. After the lower end of the specimen was gripped, the load control mode was immediately selected and the load is commanded to be zero. Finally the stroke control mode was selected again and the stroke reading was set to zero before the test started. The above steps removed residual load upon gripping and ensured that the test started with real zero load and zero stroke readings. Load, stroke and time were recorded during the test through the MTS data acquisition system at a sampling rate of 50 Hz.

3.3.2 Monotonic tensile tests

Monotonic tensile tests were carried out under stroke control mode using the MTS machine. Three different crosshead speeds, 5, 30 and 60mm/min, were used to investigate the effect of loading rate on material toughness and the deformation mechanisms involved. The ultimate tensile strength [100] was determined by dividing the maximum load by the original cross sectional area of the specimen. In addition, the toughness, defined as the energy consumption during the test, i.e. the area under the load-displacement curve, was determined for each specimen. Considering the data scattering from the mechanical testing, at least 42 repetitive tests were conducted for each crosshead speed and the statistical distributions were examined for material properties such as ultimate strength, extension at break and toughness (as defined above).

3.3.3 Multi-stage tensile tests

Based on results from the monotonic tensile tests, loading rates that were in favor of a particular deformation mechanism were identified, 5 and 60mm/min for crazing and shear yielding, respectively, as to be presented in the following chapter. Multi-stage tensile tests were then conducted using these two crosshead speeds to further understand the effect on the mechanical properties of ABS, that is, to evaluate the

effect of pre-existing deformation on the development of the other mechanism during the tensile test. Two scenarios were considered for the multistage tensile tests. One was to use a low crosshead speed of 5mm/min to a prescribed stroke to introduce crazing. After unloading, the specimen was immediately loaded at a high crosshead speed of 60mm/min until failure. The other scenario was to reverse the above order of the crosshead speeds. The MTS control system was able to realize the pre-loading to a prescribed stroke and then unloaded it to zero and reloaded it at the new crosshead speed. Using different prescribed stroke values, extent of deformation by one mechanism was changed. The above two scenarios of the multi-stage tensile tests are summarized in Table 3.2. Totally, about 25 specimens were used for each loading condition. Mechanical properties and their variation were analyzed in the same way as those for the monotonic tensile tests.

Table 3.2 The scenarios of the multi-stage tensile tests

<table>
<tr><th></th><th colspan="2">pre-loading</th><th rowspan="2"></th><th>tensile loading</th></tr>
<tr><th></th><th>crosshead speed (mm/min</th><th>predetermined stroke (mm)</th><th>crosshead speed (mm/min)</th></tr>
<tr><td rowspan="3">scenario 1</td><td rowspan="3">5</td><td>2.563</td><td rowspan="6">load returning to zero</td><td rowspan="3">60</td></tr>
<tr><td>3.129</td></tr>
<tr><td>6</td></tr>
<tr><td rowspan="3">scenario 2</td><td rowspan="3">60</td><td>2.998</td><td rowspan="3">5</td></tr>
<tr><td>3.432</td></tr>
<tr><td>6</td></tr>
</table>

Chapter 4 Results and Discussion

4.1 Monotonic Tensile Tests

Repetitive monotonic tensile tests were conducted at crosshead speeds 5, 30 and 60mm/min. Test results are summarized in section 4.1.1, and Weibull analysis of the results in section 4.1.2 to quantify the damage mechanisms involved in the deformation.

4.1.1 Test results

As depicted in Fig. 4.1, post-fracture specimens show distinct deformation mechanisms by the change of the crosshead speed.

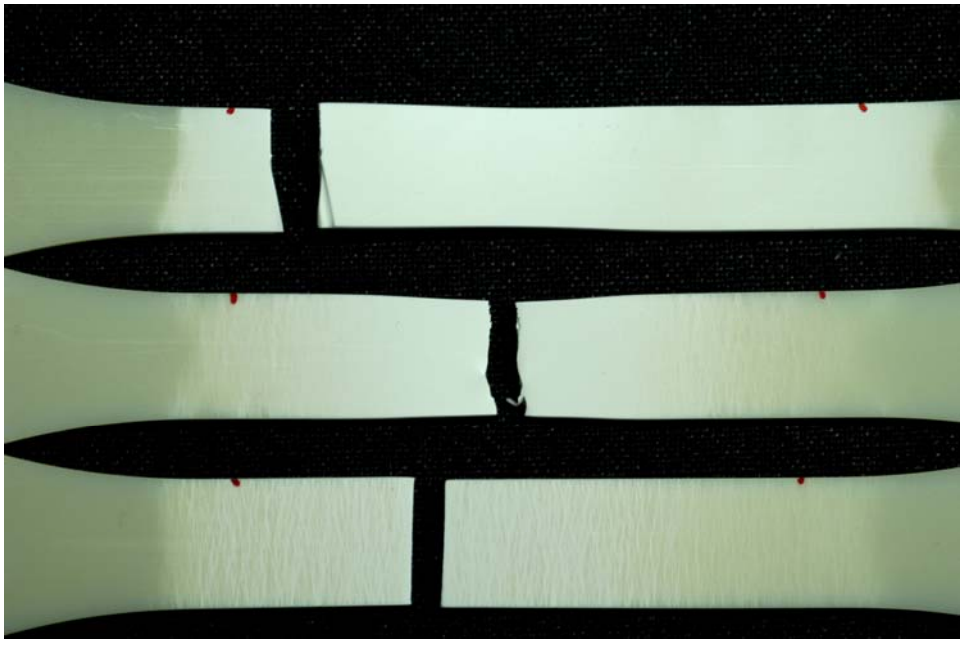

Fig. 4.1 Post-fracture specimens for the crosshead speeds of 5mm/min (bottom), 30mm/min (middle) and 60mm/min (top)

With the crosshead speed of 5mm/min (bottom in Fig. 4.1), damage involves a great amount of tiny but dense strips that are perpendicular to the loading direction. With the

crosshead speed of 60mm/min (top), damage appears as a fairly uniform whitening area over the gauge section. For the medium crosshead speed of 30mm/min (middle), the damage appears to show both features, with the extensive stress whitening in the middle section, in which the fracture occurred, and strips at the ends of the gauge section. This is probably because of the change of strain rate along the specimen even though one crosshead speed was applied. Therefore, specimens tested at 30mm/min actually show a transition of the damage mechanisms due to the change of strain rate. It was also noticed that necking occurred in the whitening area at the crosshead speeds of 30 and 60mm/min, while no obvious necking was observed on the specimen at 5mm/min. Considering that crazing and shear yielding are the two main mechanisms involved in the deformation of ABS [30], and necking is a remarkable sign of shear yielding, the dominant deformation mechanism for specimens tested at the crosshead speed of 60mm/min and the stress whitening region in the mid-section of specimens tested at 30mm/min are believed to be shear yielding. At the crosshead speed of 5mm/min, on the other hand, crazing must have dominated the deformation.

Typical load-displacement curves from the monotonic tensile tests are presented in Fig. 4.2. All of the load-displacement curves illustrate extensive elongations. Initially the load increases almost linearly with stroke till yield point is reached. Then the load drops relatively quickly for over 10%, and decreases gradually until failure. Experimental observations suggest that the rapid load drop coincides with the appearance of damage on the specimens. They also suggest that the modulus remains constant within the range of the crosshead speed used. However, by increasing the crosshead speed, the ultimate strength, the post-yield load level and the extension all have a trend of increase. They all contribute to increasing the area under the load-displacement curve, thus the toughness increase.

Data of the ultimate tensile strength (UTS), extension at break and toughness are tabulated in Appendix 2. Their mean values and the standard deviations are summarized in Table 4.1, and their variations with the crosshead speed shown in Fig. 4.3.

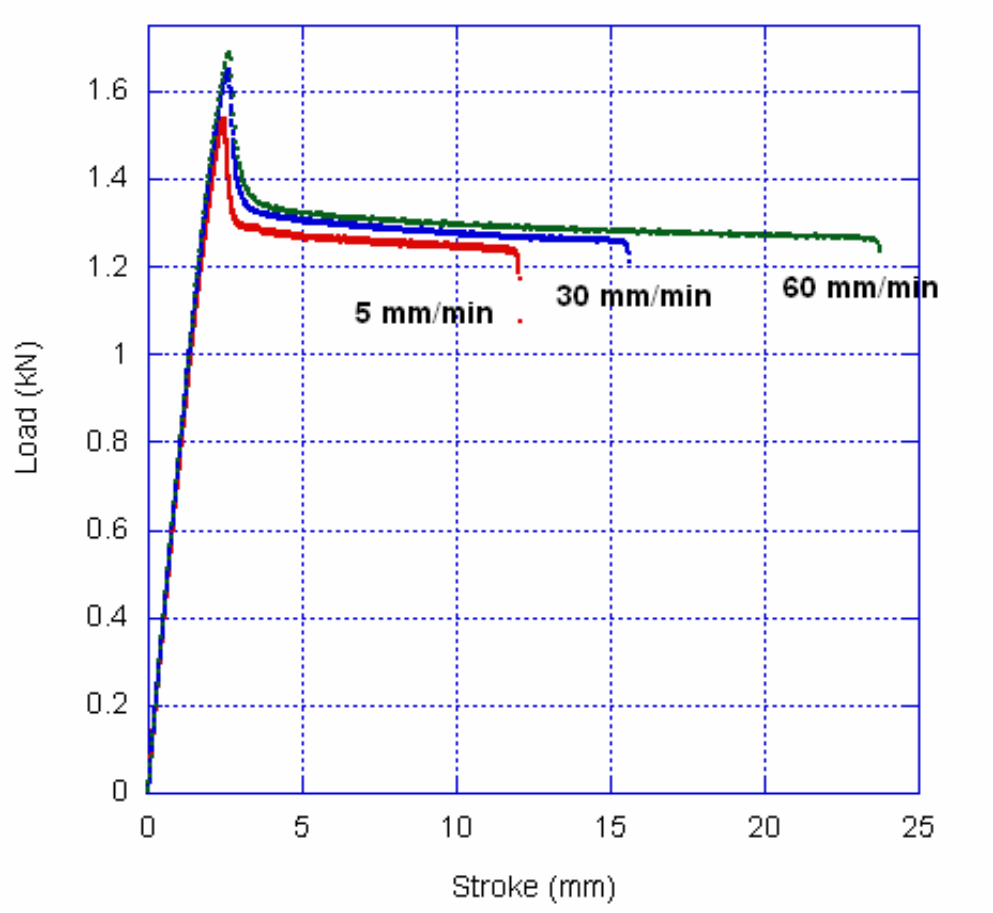

Fig. 4.2 Typical load-displacement curves at crosshead speeds of 5, 30 and 60mm/min

Table 4.1 Results of UTS, extension at break and toughness for monotonic tests at three crosshead speeds

Crosshead speed (mm/min) \ # of tests		5 — 51	30 — 50	60 — 50
UTS (MPa)	mean	36.7	39.2	40.2
	standard deviation	0.25	0.31	0.20
Extension at break (mm)	mean	11.8	16.4	22.9
	standard deviation	2.95	7.42	9.45
Toughness (J)	mean	13.7	19.7	28.0
	standard deviation	3.60	9.21	11.61

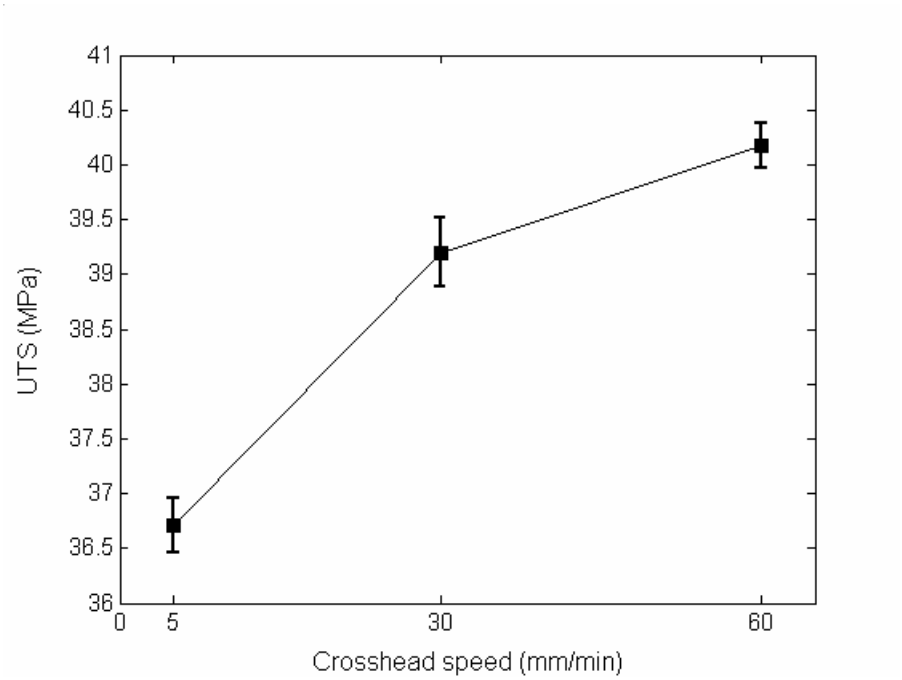
41
40.5
40
39.5
39
38.5
38
37.5
37
36.5
36
UTS (MPa)
0
5
30
60
Crosshead speed (mm/min)

(a)

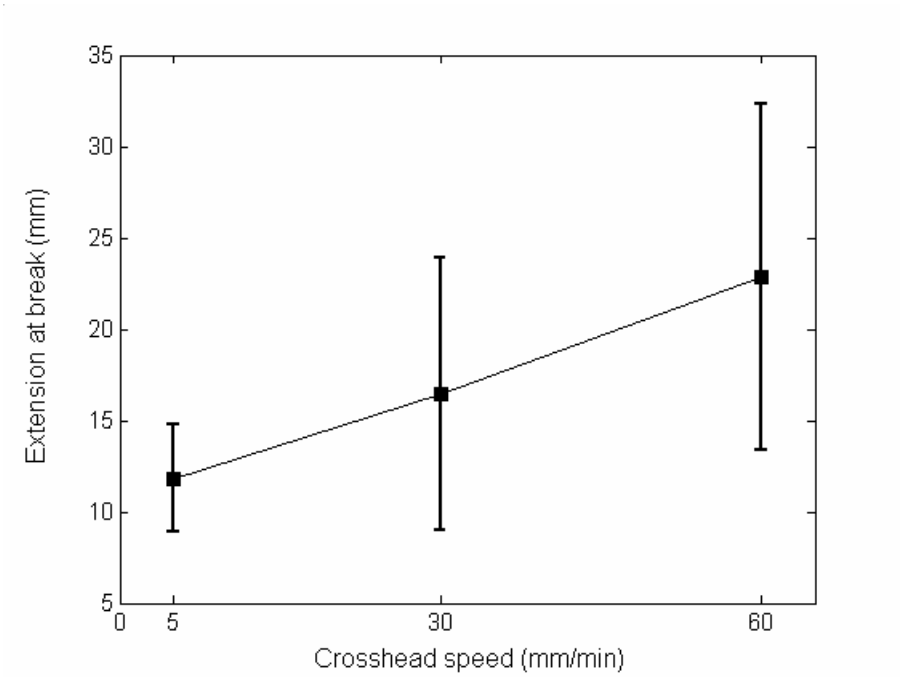
35
30
25
20
15
10
5
Extension at break (mm)
0
5
30
60
Crosshead speed (mm/min)

(b)

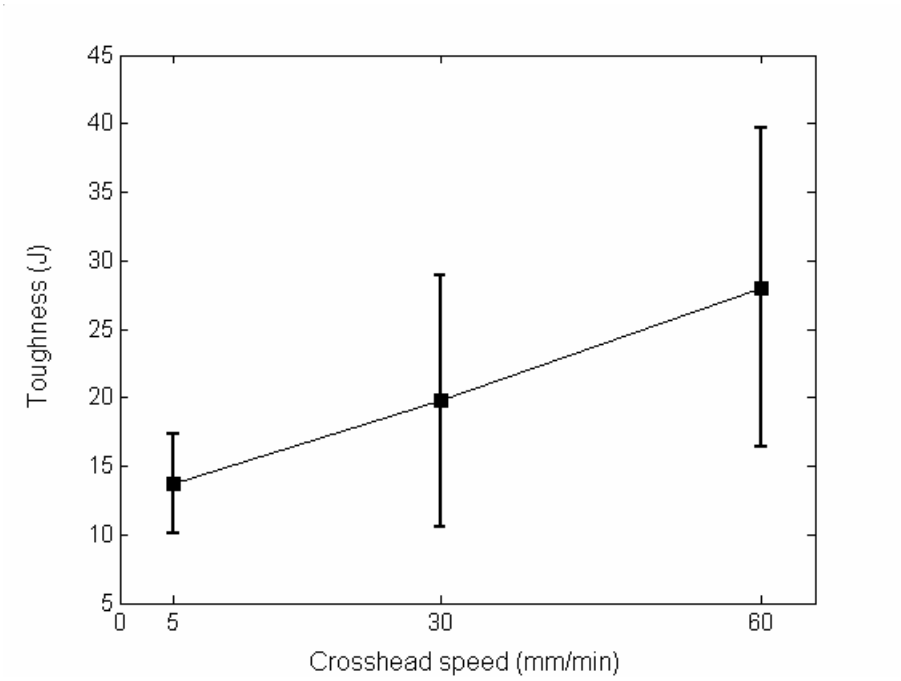

(c)

Fig. 4.3 Variation of (a) ultimate strength, (b) extension at break and (c) toughness with crosshead speed

The UTS, extension at break and toughness all increase with the increase of the crosshead speed, though the UTS shows a different trend from the extension and toughness. Also, variation of the UTS is relatively small compared to that for the extension at break and toughness. The results suggest that by increasing the crosshead speed from 5 to 60mm/min, the mean value of the UTS increases by only 9.46%, while for the extension at break and toughness, they are 93.45% and 104.55%, respectively.

When considering the ratio of deviation to the mean value, it ranges 0.5~0.8% for the UTS, 25~45% for extension at break and 26~47% for toughness. Hence, extension at break and toughness bear more variation characteristics than the UTS. In addition, the favorable deformation mechanism at a given crosshead speed does not seem to have a clear influence on the standard deviation of the UTS values. But it is noticed that the standard deviation has its largest value at the intermediate crosshead speed of 30mm/min. This is probably due to the competing effect of crazing and shear yielding that coexist at this crosshead speed. Although this competing effect may also contribute to the variation

of the extension at break and toughness, their standard deviation values show a clear trend of increasing with the crosshead speed. This is probably because the variation of those values by the shear yielding overpowers the variation due to the competing effect.

4.1.2 Weibull analysis

It is well established [5, 21, 30] that crazing and shear yielding are the two mechanisms involved in the deformation behaviour of ABS. Therefore, two-parameter Weibull and two group mixed Weibull (see Chapter 2) were applied to the test data analysis. The parameter determination and graph generation were through Reliasoft Weibull++ 7 (ReliaSoft Corporation). Note that if some of the specimens did not fail at the end of the tests or some specimens failed in a different manner, these test data would be "censored" or "suspended". Under this circumstance, the calculation of median ranks for the unsuspended test data would need adjustment [89]. In our case, however, all the specimens fractured, thus the test data were treated as a single set without suspension. For the two-parameter Weibull evaluation, settings of standard linear regression on x and median ranks were assigned for calculating the shape parameter β and the scale parameter η. When based on the two-group mixed Weibull for evaluation, the settings of nonlinear regression and median ranks were used to determine β, η and the portion p for both subpopulations. The correlation coefficient ρ was also given for each evaluation. The results are presented in Table 4.2. The unreliability (CDF) curves and PDF curves by two-parameter Weibull distribution and two group mixed Weibull distribution are illustrated in Figs. 4.4, 4.5 and 4.6 for UTS, extension at break and toughness, respectively.

Table 4.2 Parameter values for two-parameter Weibull and two-group mixed Weibull analysis for (a) UTS, (b) extension at break and (c) toughness

(a)

Crosshead speed (mm/min)			5	30	60
Two-parameter Weibull	Shape parameter β		189.7	159.4	250.7
	Scale parameter η (MPa)		36.8	39.3	40.3
	Correlation coefficient ρ		0.95	0.96	0.99
Two-group mixed Weibull	1st subpopulation	β_1	358.9	247.8	300.7
		η_1 (MPa)	36.5	39.0	40.1
		p_1	0.50	0.50	0.49
	2nd subpopulation	β_2	324.0	320.5	434.8
		η_2 (MPa)	37.0	39.5	40.4
		p_2	0.50	0.50	0.51
	ρ		0.98	0.98	0.99

(b)

Crosshead speed (mm/min)			5	30	60
Two-parameter Weibull	β		4.5	2.3	2.5
	η (mm)		12.9	18.6	25.9
	ρ		0.98	0.99	0.99
Two-group mixed Weibull	1st subpopulation	β_1	30.1	24.3	3.9
		η_1 (mm)	15.4	16.3	26.3
		p_1	0.28	0.18	0.53
	2nd subpopulation	β_2	5.0	1.9	1.7
		η_2 (mm)	11.4	19.0	25.0
		p_2	0.72	0.82	0.47
	ρ		0.98	0.94	0.96

(c)

Crosshead speed (mm/min)			5	30	60
Two-parameter Weibull	β		4.2	2.2	2.4
	η (J)		15.1	22.3	31.8
	ρ		0.98	0.99	0.99
Two-group mixed Weibull	1st subpopulation	β_1	22.7	21.5	4.8
		η_1 (J)	18.1	19.8	32.1
		p_1	0.23	0.18	0.38
	2nd subpopulation	β_2	4.4	1.9	1.9
		η_2 (J)	13.7	22.8	31.3
		p_2	0.77	0.82	0.62
	ρ		1.00	0.95	0.97

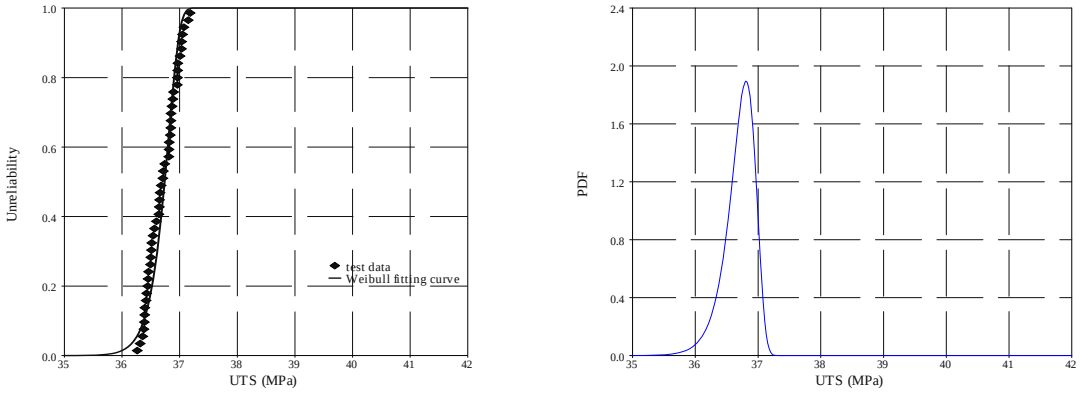

5mm/min

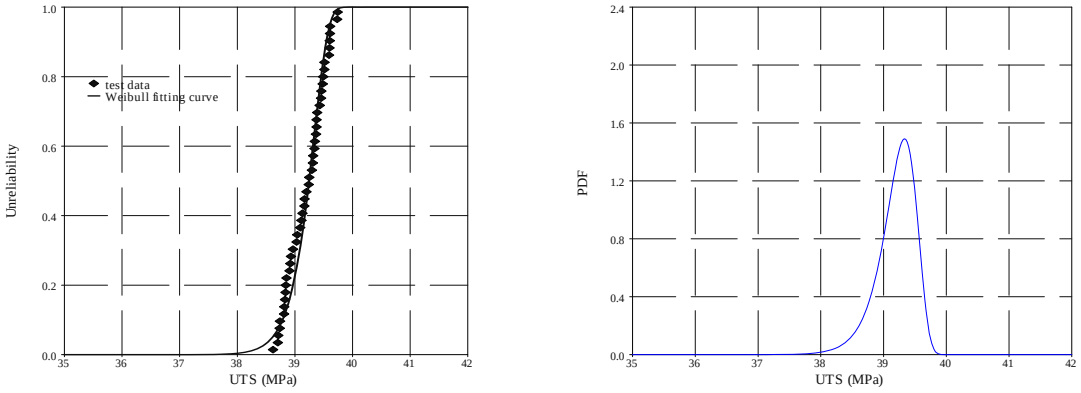

30mm/min

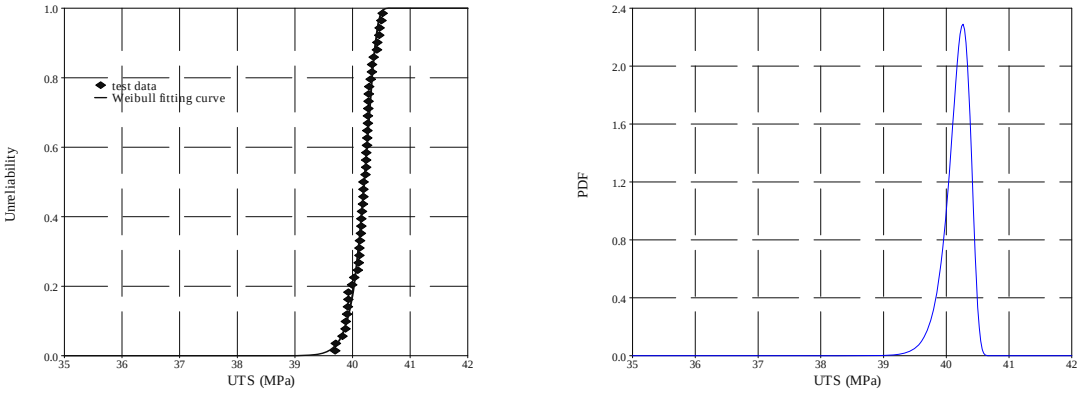

60mm/min

(a)

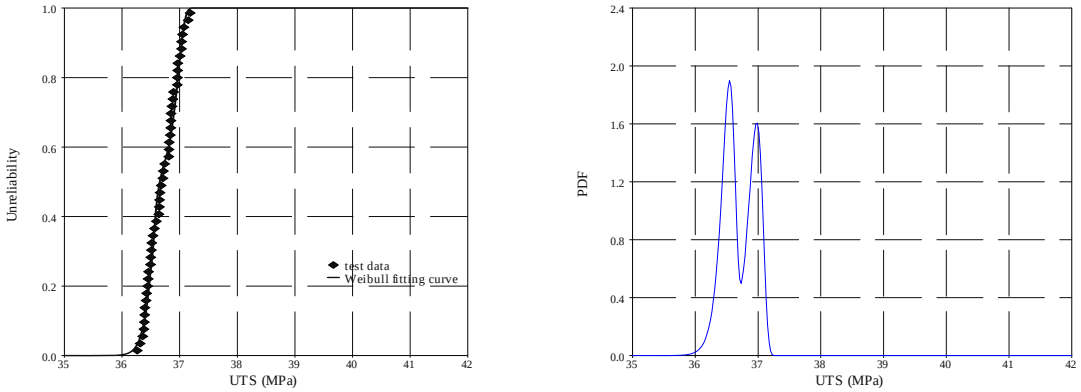

5mm/min

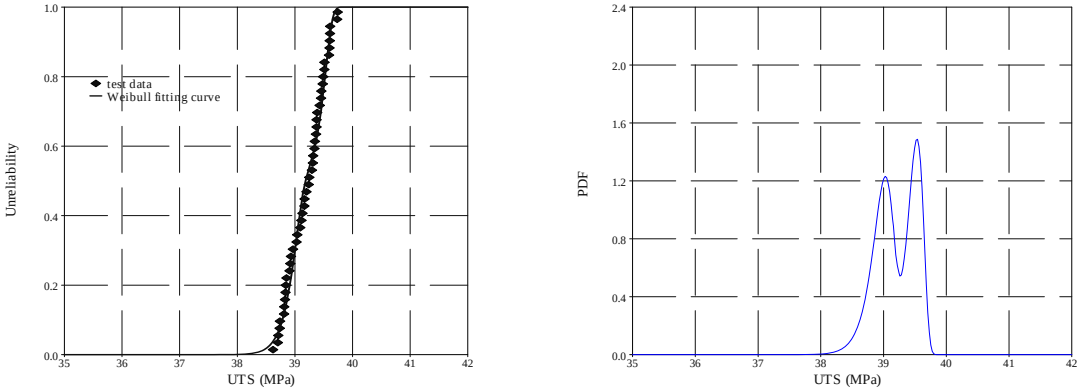

30mm/min

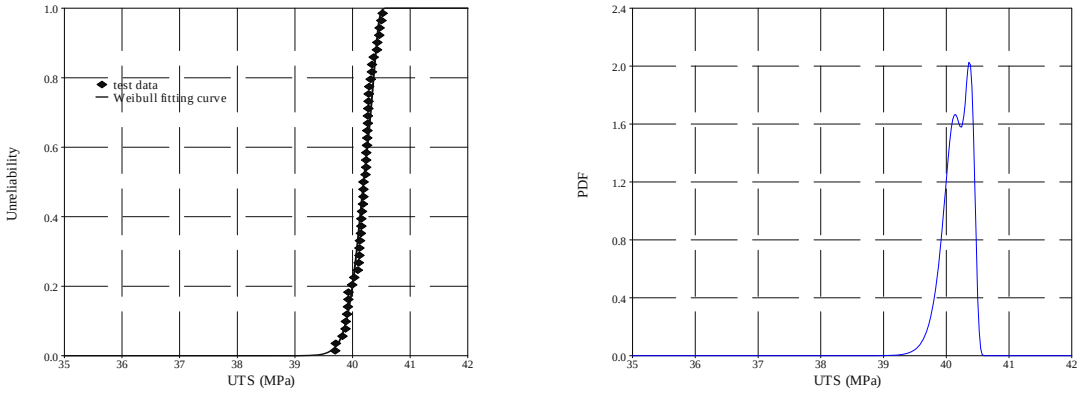

60mm/min

(b)

Fig. 4.4 Results of unreliability and PDF on UTS by (a) two-parameter Weibull distribution and (b) two group mixed Weibull distribution

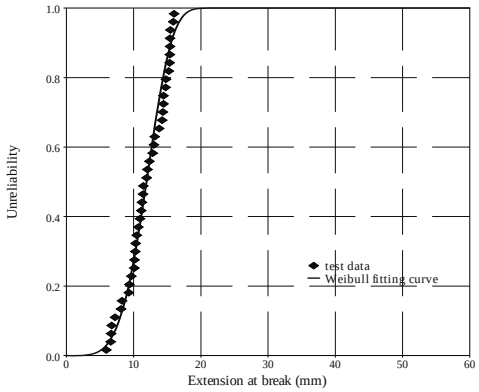

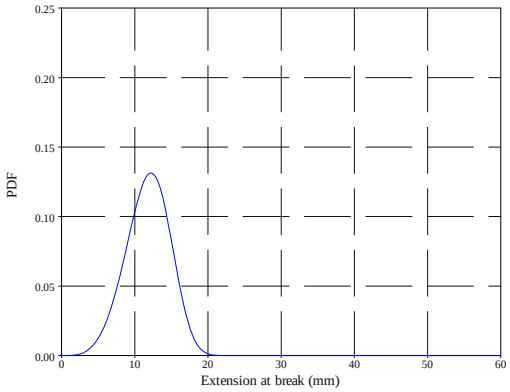

5mm/min

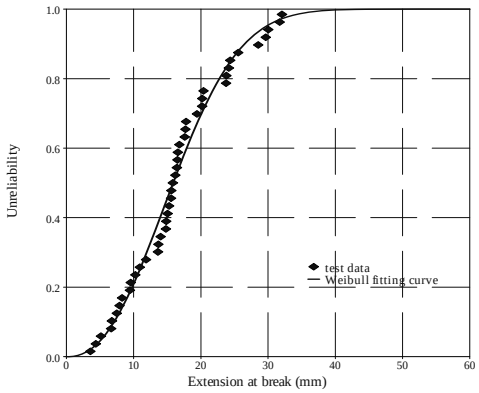

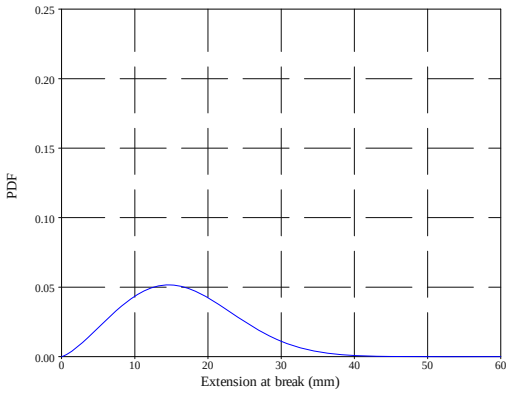

30mm/min

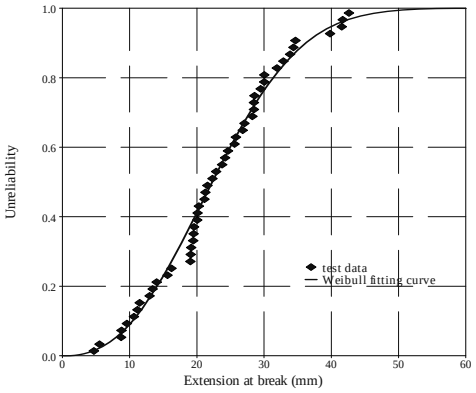

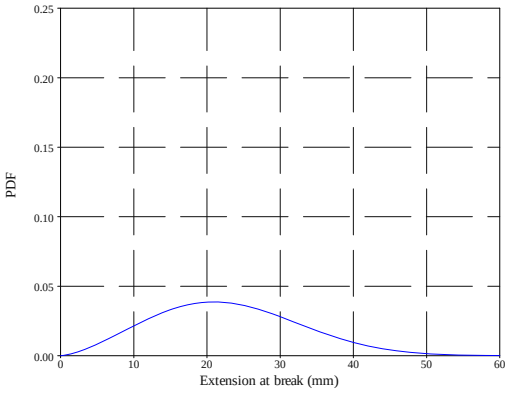

60mm/min

(a)

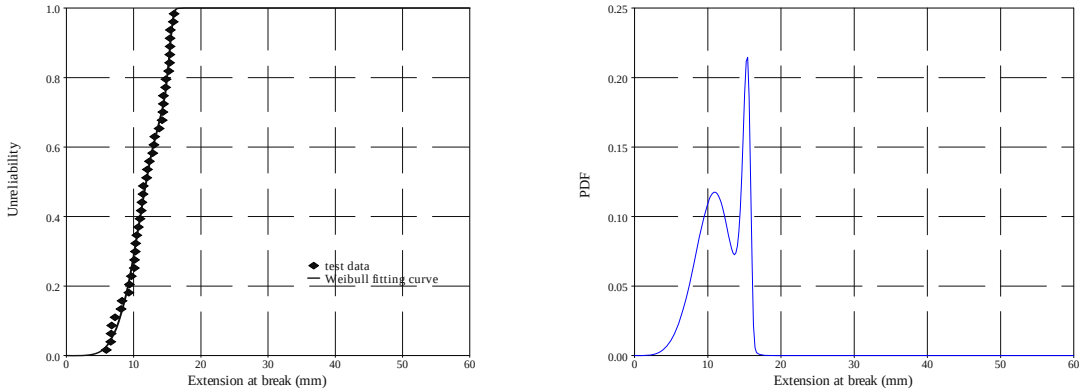

5mm/min

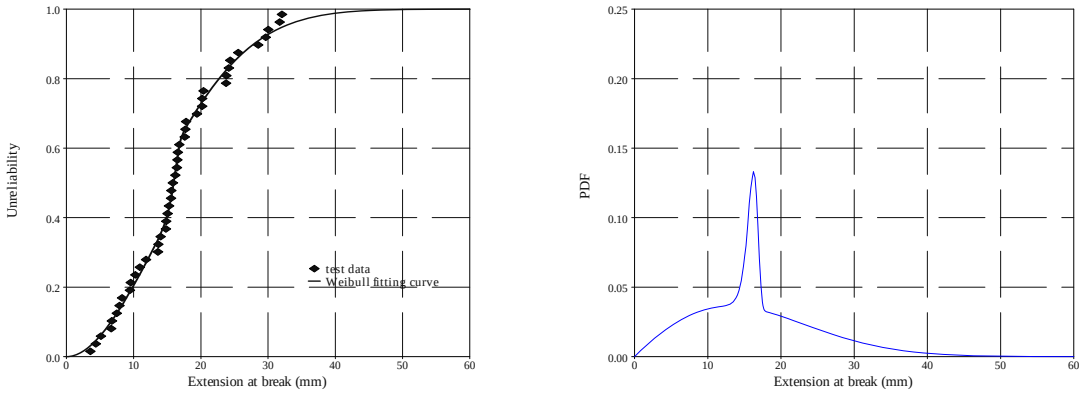

30mm/min

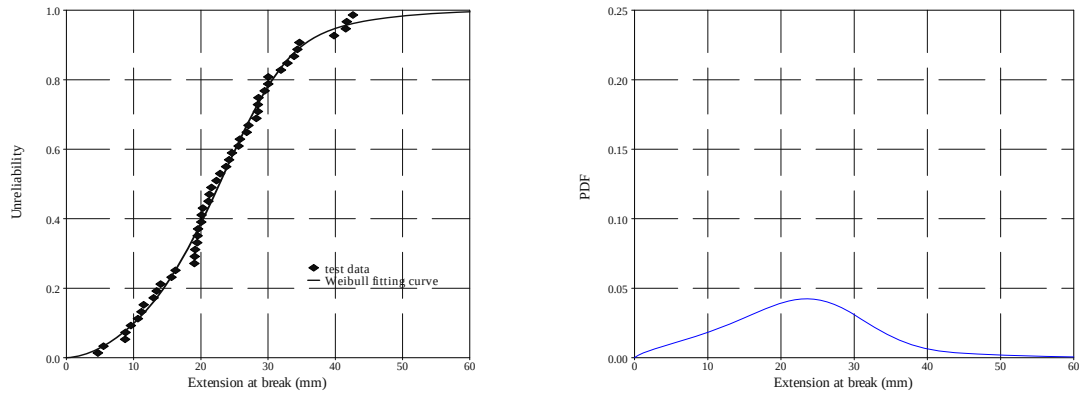

60mm/min

(b)

Fig. 4.5 Results of unreliability and PDF on extension at break by (a) two-parameter Weibull distribution and (b) two group mixed Weibull distribution

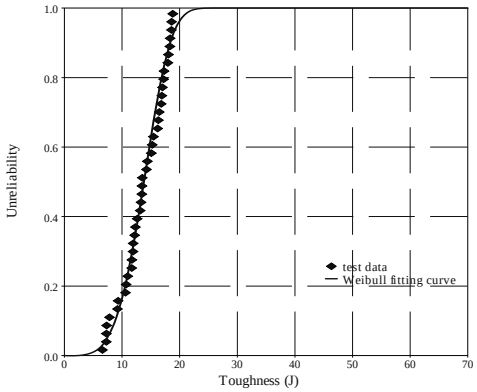

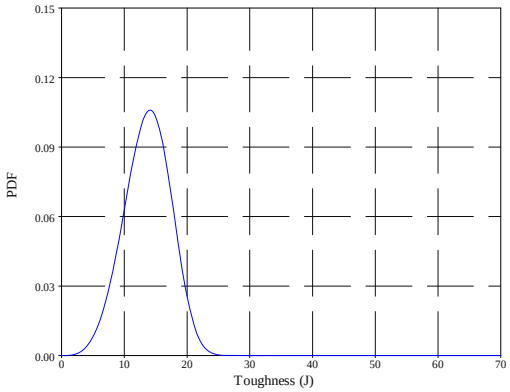

5mm/min

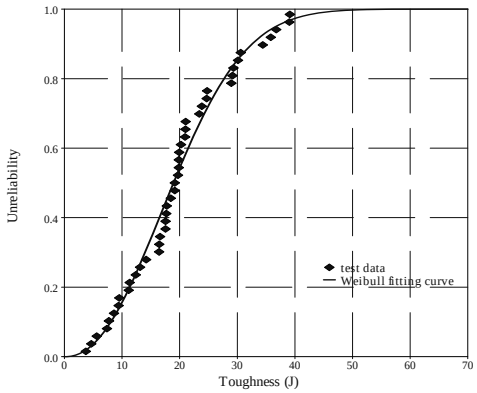

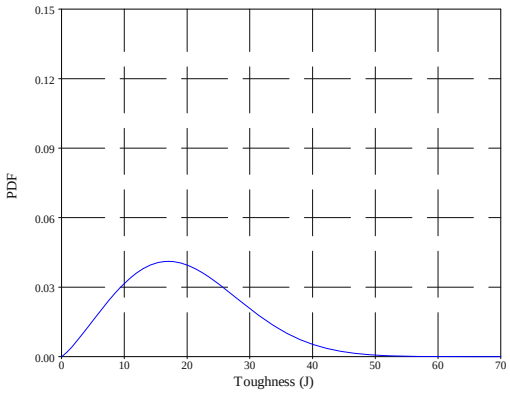

30mm/min

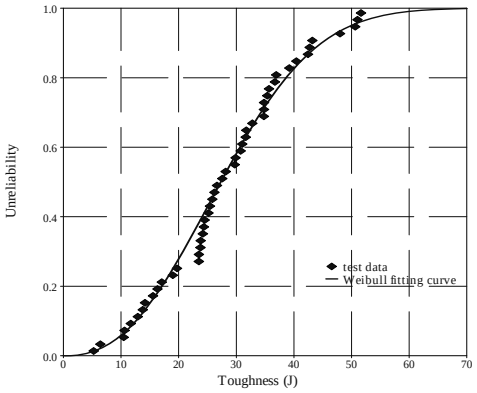

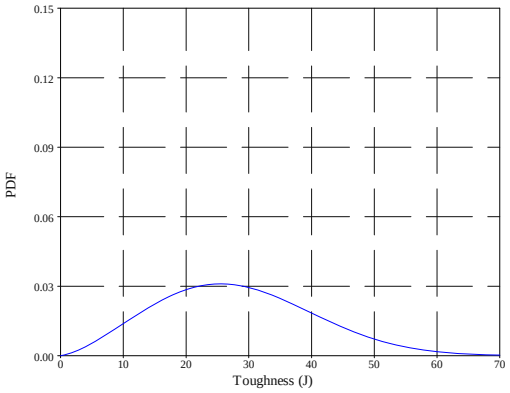

60mm/min

(a)

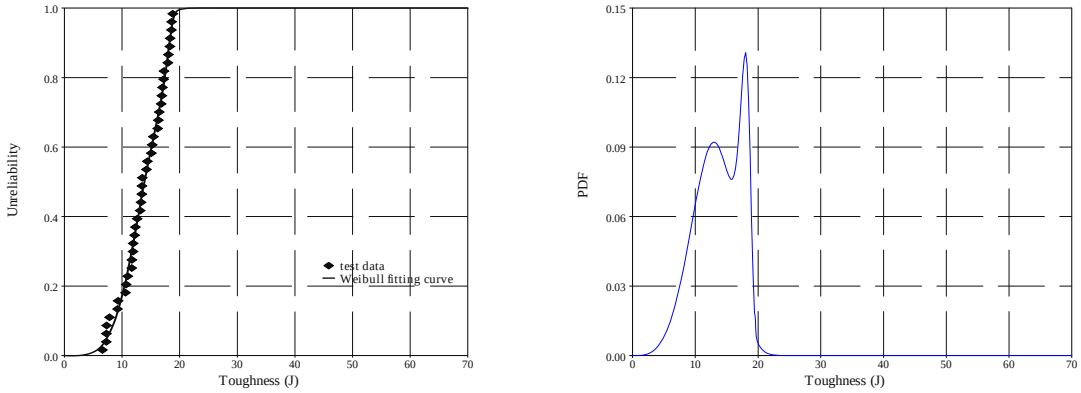

5mm/min

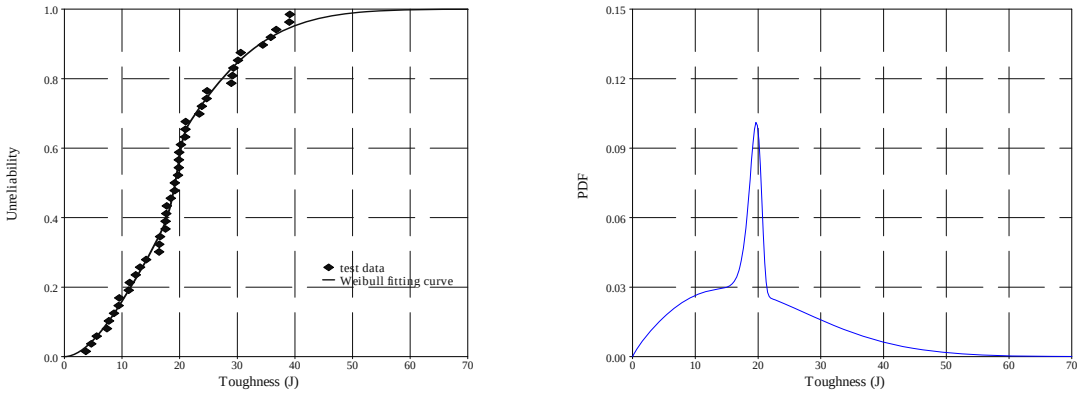

30mm/min

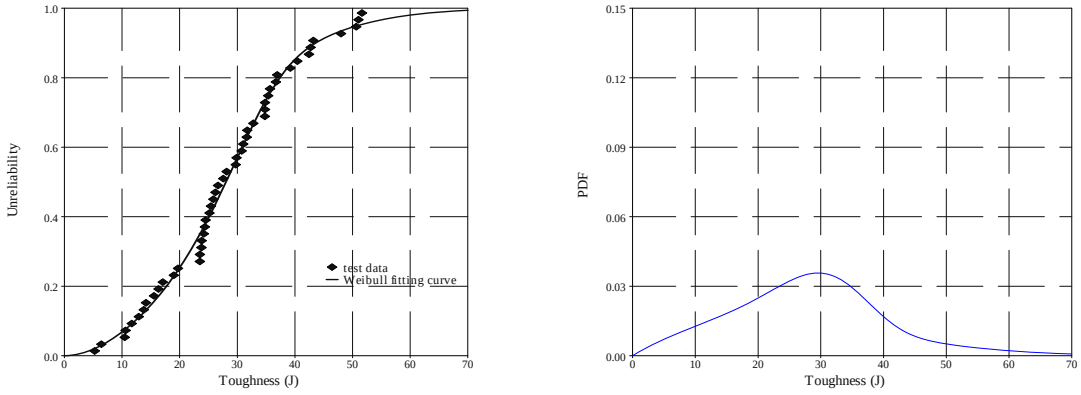

60mm/min

(b)

Fig. 4.6 Results of unreliability and PDF on toughness by (a) two-parameter Weibull distribution and (b) two group mixed Weibull distribution

From these results, both two-parameter Weibull distribution and two group mixed Weibull distribution can satisfactorily fit the test data to characterize the unreliability distribution of the material properties. The mixed Weibull distribution shows its advantage of describing details with the ability to fit distributions when multiple failure mechanisms are involved.

In the two-parameter Weibull evaluation on the ultimate strength, β values are very large for all the three crosshead speeds. The unreliability curves have a steep rise and the PDFs have relatively sharp and narrow peaks. In the two group mixed Weibull analysis, β still shows very large values for all the subpopulations. For each crosshead speed, the parameters of the two subpopulations are not much different, and the portion (or mixing weight) of each subpopulation is close to, if not exactly, 0.5. The PDF plot for each crosshead speed has two sharp peaks that look similar and are close to each other. Therefore, we believe that single group distribution is acceptable for the analysis of UTS. This is supported by the unreliability curves for the three crosshead speeds, Fig. 4.7.

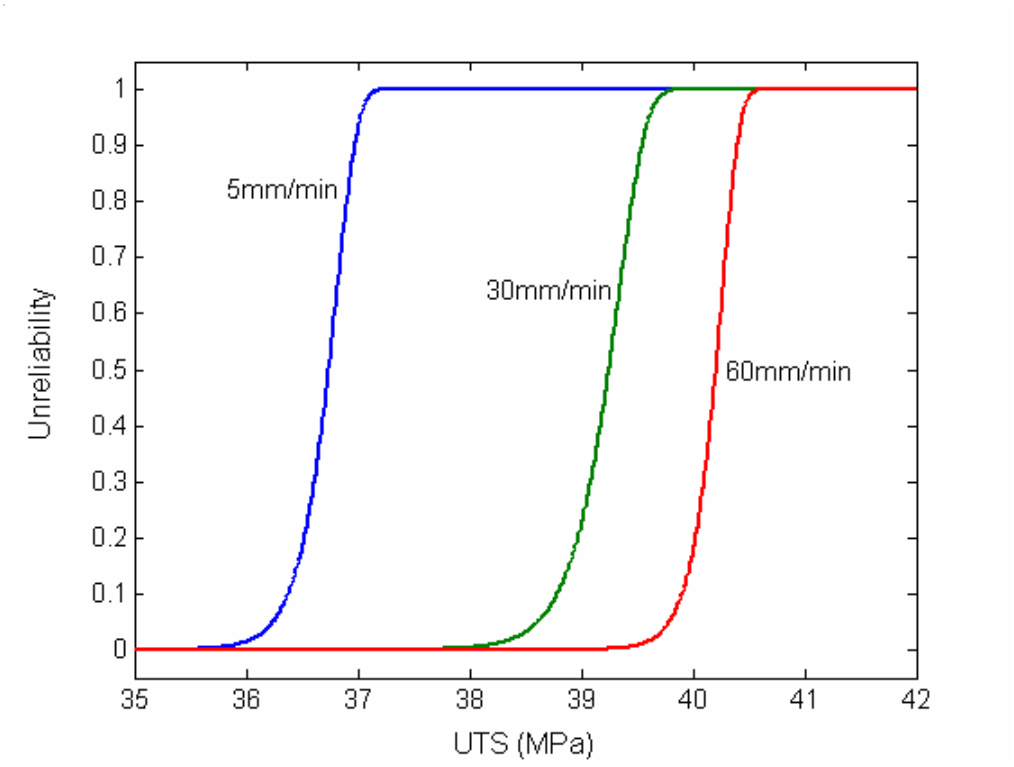

Fig. 4.7 Unreliability of UTS (by two-parameter Weibull distribution) for the three crosshead speeds

Using two-parameter Weibull distribution, changing the crosshead speed only causes shift of the unreliability curves of UTS. Other than that, characteristics of the curves remain largely unchanged, except that the rising of the curve for 30mm/min is slightly gentler than the other two curves. This indicates that the unreliability curve for 30mm/min has a relatively more scattered distribution than the other two, probably due to the competing effect of the two deformation mechanisms, crazing and shear yielding, as mentioned earlier.

The Weibull evaluation results on extension at break and toughness are again very similar among the three crosshead speeds. It is noticed that using the two-parameter Weibull distribution to evaluate toughness, the β values are much smaller than the results for UTS. This reduces steepness of the unreliability curve, and by comparing Figs. 4.5 and 4.6 with Fig. 4.4, the distribution ranges of PDFs for the former are much larger than the latter. In addition, the η value has a very large variation for the three sets of data. In general, with the increase of the crosshead speed, β decreases (though β has very similar values for the crosshead speeds of 30 and 60mm/min) and η increases drastically. That is, the distribution characteristics of toughness have changed tremendously as the crosshead speed varies.

The above phenomenon can also be shown by the unreliability curves with the two-group mixed Weibull distribution (Fig. 4.8). The figure suggests that the characteristic life increases and the steepness of the unreliability curve decreases with the increase of the crosshead speed.

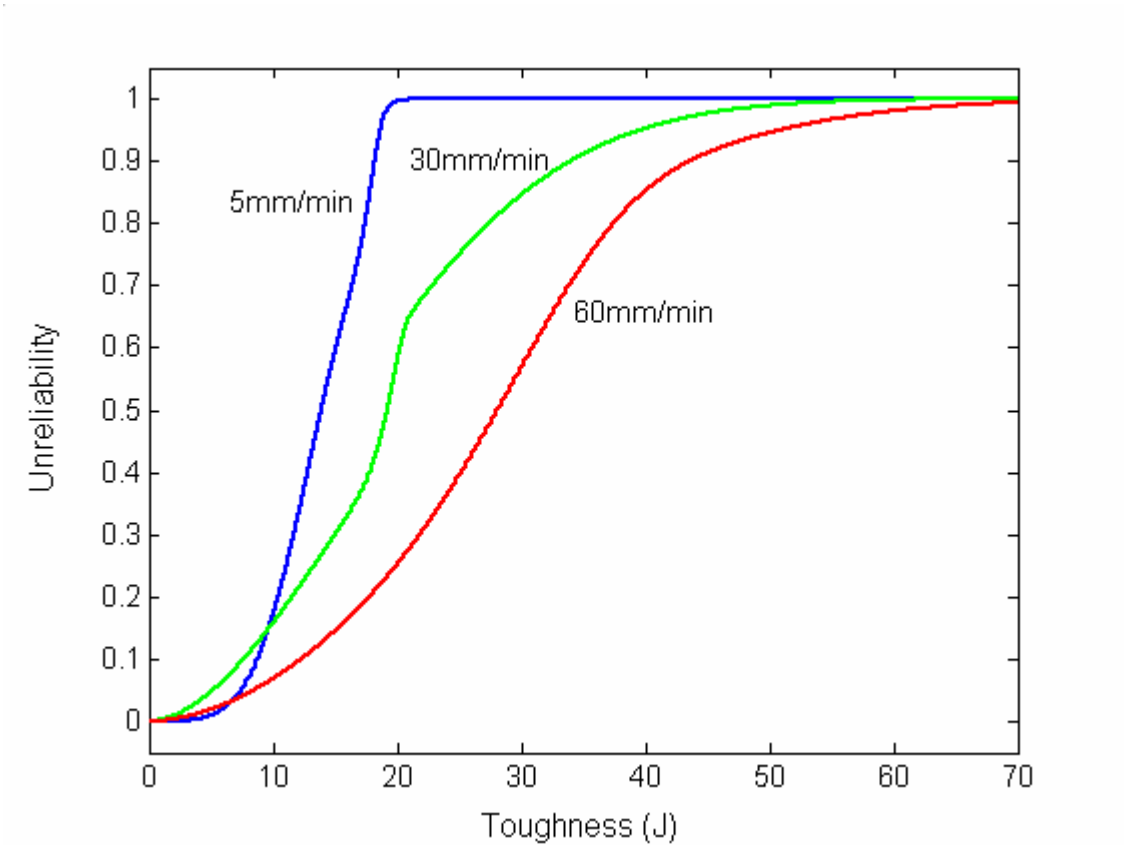

Fig. 4.8 Comparison of unreliability curves for the three crosshead speeds by two-group mixed Weibull distribution

When evaluating the toughness using the two group mixed Weibull, the two subpopulations are designated in such a way that for each crosshead speed, the first subpopulation always has a larger β value. As shown in Fig. 4.6, the two group mixed Weibull is able to better characterize the kink of the unreliability curve at 30mm/min than the two-parameter Weibull distribution. At the crosshead speed of 5mm/min, the PDF of the toughness distribution can be decomposed into a sharp peak and a slightly broad one. For 30mm/min, it consists of one sharp peak and one very broad curve. For the crosshead speed of 60mm/min, however, only one broad curve can be identified even using the two group mixed Weibull distribution. Fig. 4.9 shows the curves for each of the unreliability subpopulations of the toughness distributions. For each crosshead speed, the first subpopulation with larger β value tends to have larger steepness. Note that the β value of the second subpopulation for the crosshead speed of 5mm/min is comparable to that of

the first subpopulation for 60mm/min, but η for the former is much smaller which makes the corresponding unreliability curve still relatively steep. As a result, all unreliability curves can be classified into two groups with distinctly different steepness. That is, both subpopulations for the crosshead speed of 5mm/min and the first subpopulation for 30mm/min are in one group that has relatively large curve steepness. The second subpopulation for 30mm/min and both subpopulations for 60mm/min are in the other group that has small steepness. Therefore, each of the toughness distribution at the crosshead speeds of 5 and 60mm/min can be acceptably described by one group distribution and at 30mm/min two failure modes are involved, with distinct difference in the distribution characteristics. Based on the above discussions and observations, it is concluded that there is one dominant mechanism at the crosshead speed of 5mm/min, i.e. crazing, and shear yielding at 60mm/min. At the intermediate crosshead speed of 30mm/min, both mechanisms are involved.

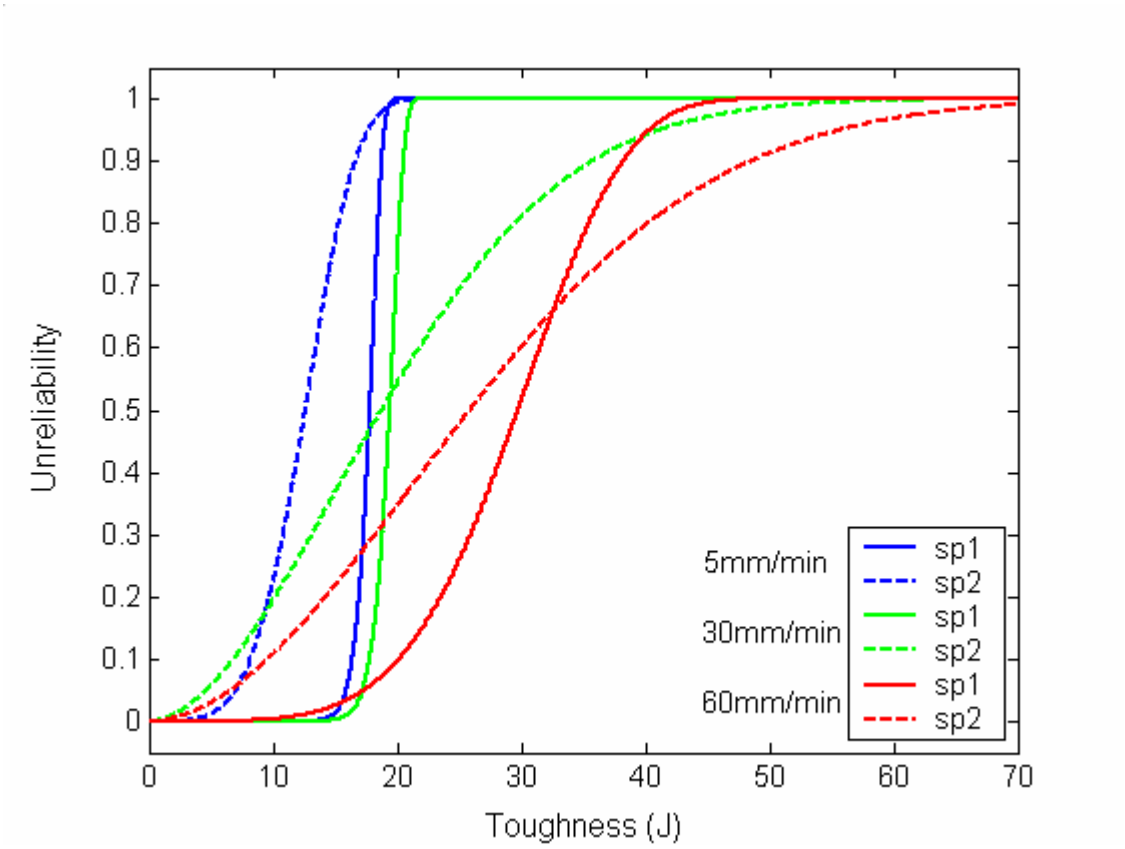

Fig. 4.9 Unreliability subpopulations of the toughness distributions at three crosshead speeds

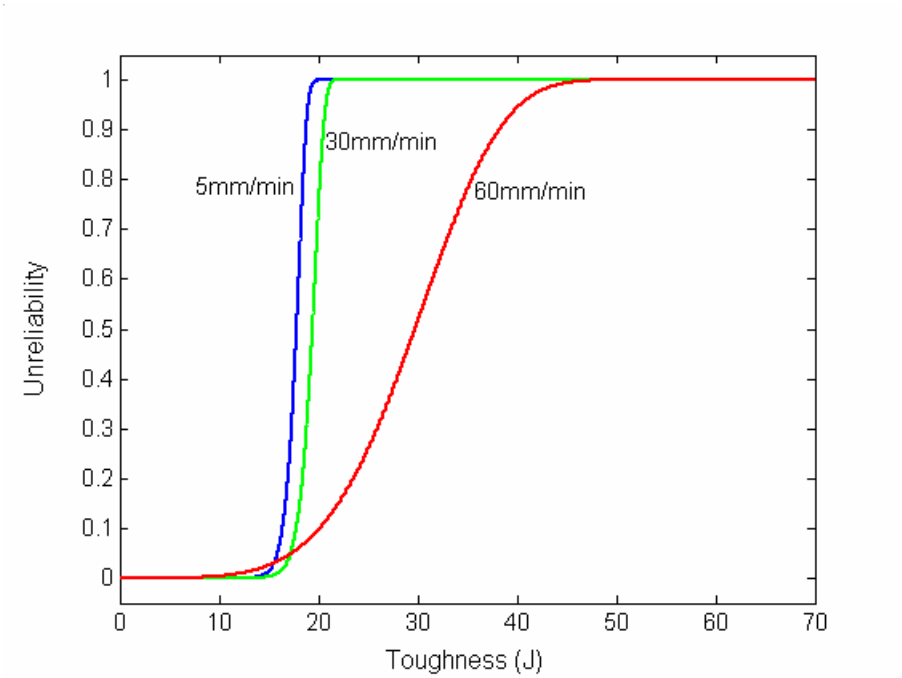

(a)

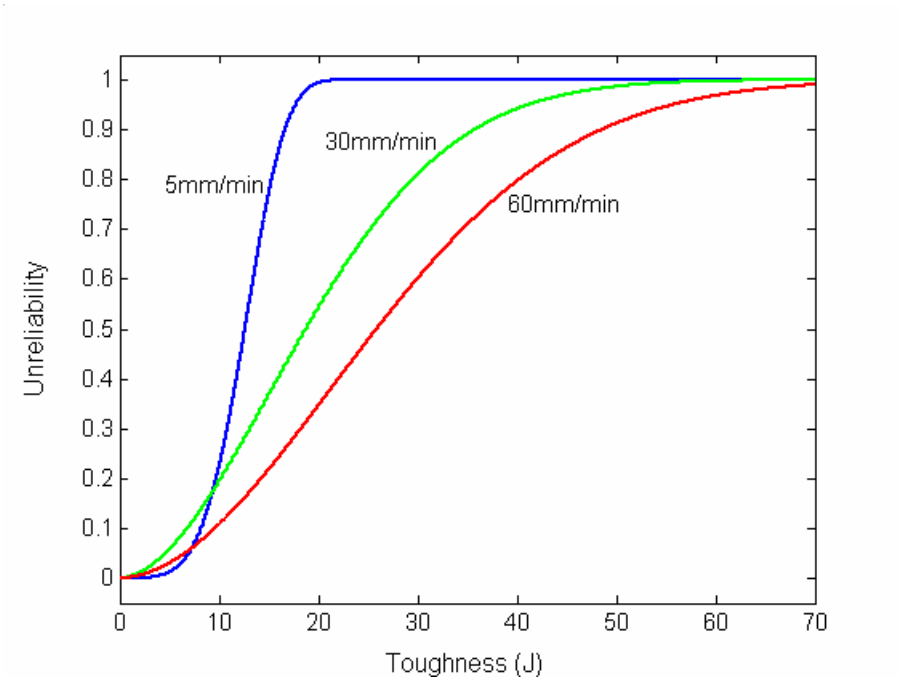

(b)

Fig. 4.10 Comparison of unreliability curves of (a) the first subpopulations and (b) the second subpopulations at the three crosshead speeds

Note that for either the first subpopulation or the second subpopulation of each of the three crosshead speeds, β has a trend of decrease and η increase with the increase of the crosshead speed. As a result, the steepness of the corresponding unreliability curves has a tendency of decrease with the crosshead speed, as shown in Fig. 4.10.

4.2 Multi-stage Tensile Tests

In the monotonic tensile tests, damage was developed through crazing and shear yielding with the increase of elongation, at the crosshead speeds of 5 and 60mm/min, respectively, as shown in Fig. 4.11. In addition, the coexistence of both deformation mechanisms was observed at the intermediate crosshead speed of 30mm/min. In order to further understand the roles of crazing and shear yielding on the toughness and the effect of one pre-existing damage on the other, multi-stage tensile tests were conducted, following the scenarios described in Chapter 3, Section 3.3.3.

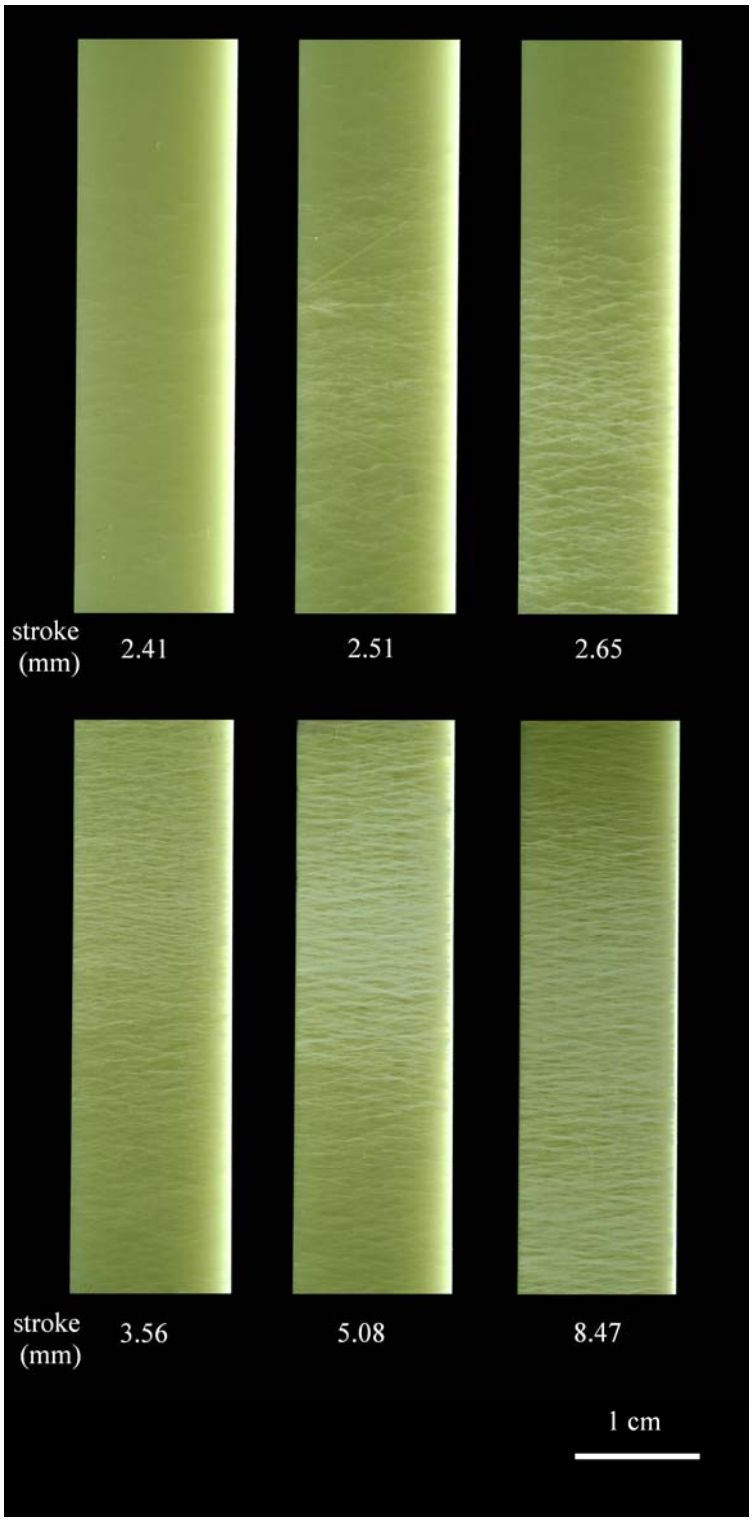

(a)

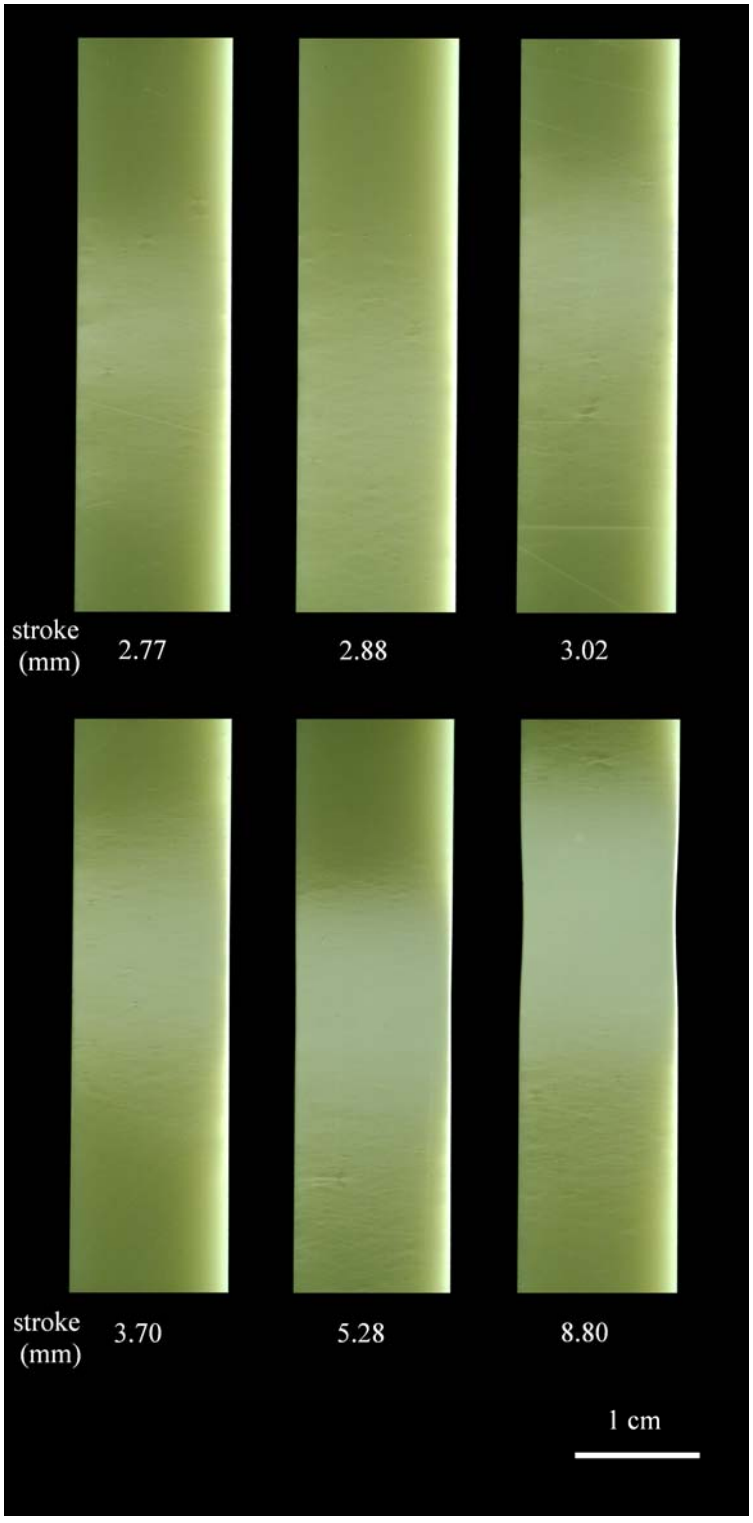

(b)

Fig. 4.11 Damage development in monotonic tensile tests at (a) 5mm/min and (b) 60mm/min

4.2.1 Test results

For the first scenario where the specimen was loaded at 5mm/min first to a stroke of 2.563, 3.129 and 6mm, and then at 60mm/min to fracture, typical load-displacement curves are displayed in Fig. 4.12.

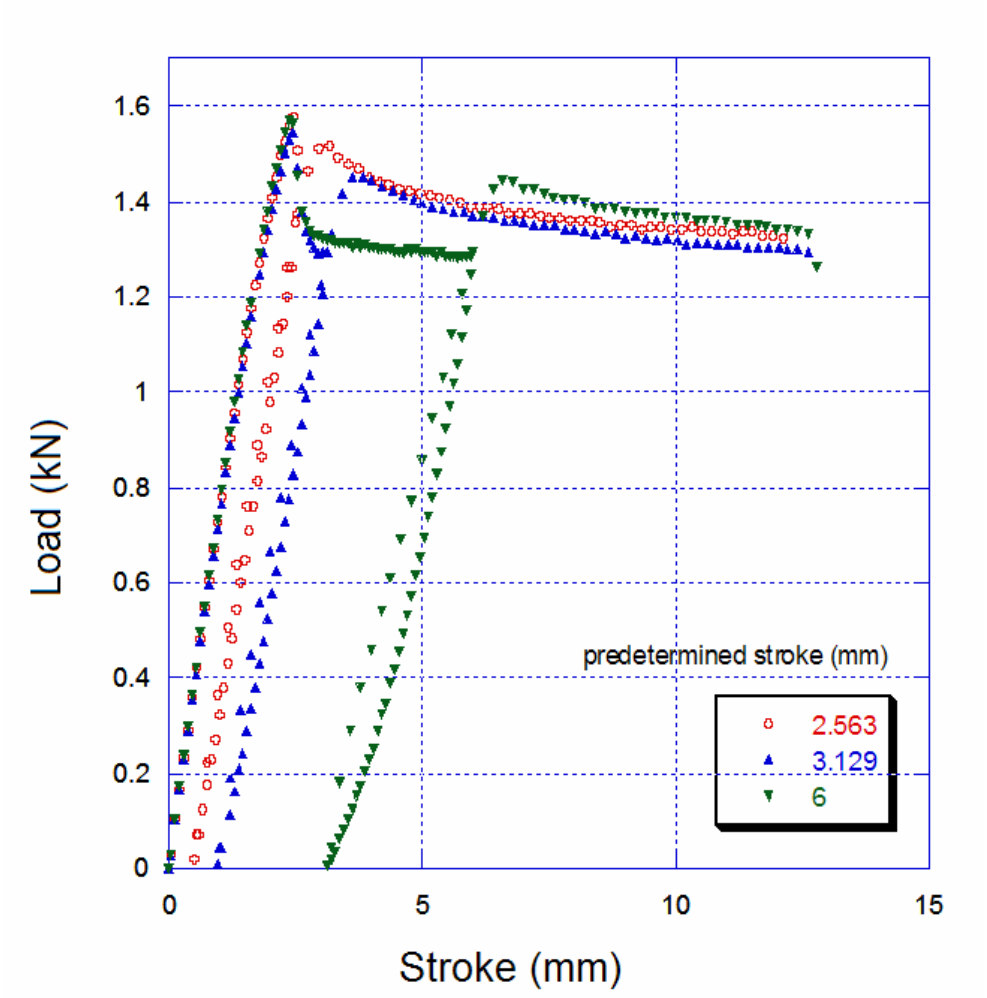

Fig. 4.12 Typical load-displacement curves for the first scenario

It can be seen that upon reloading at the crosshead speed of 60mm/min, the load-displacement curves still show a peak. As the predetermined stroke increases, the residual stroke immediately after unloading increases accordingly. The maximum strength of the second stage loading, on the other hand, decreases. A slight decrease of stiffness can also be noticed. But the total elongation does not seem to be affected in any obvious manner.

Therefore, the second stage elongation has been shortened and the corresponding toughness decreased by the increase of the first stage stroke.

For the second scenario, the specimen was loaded first at the crosshead speed of 60mm/min to a specified stroke and then at 5mm/min till fracture. All post-fracture specimens showed extensive “stress whitening” and little trace of crazing damage. Typical load-displacement curves are presented in Fig. 4.13.

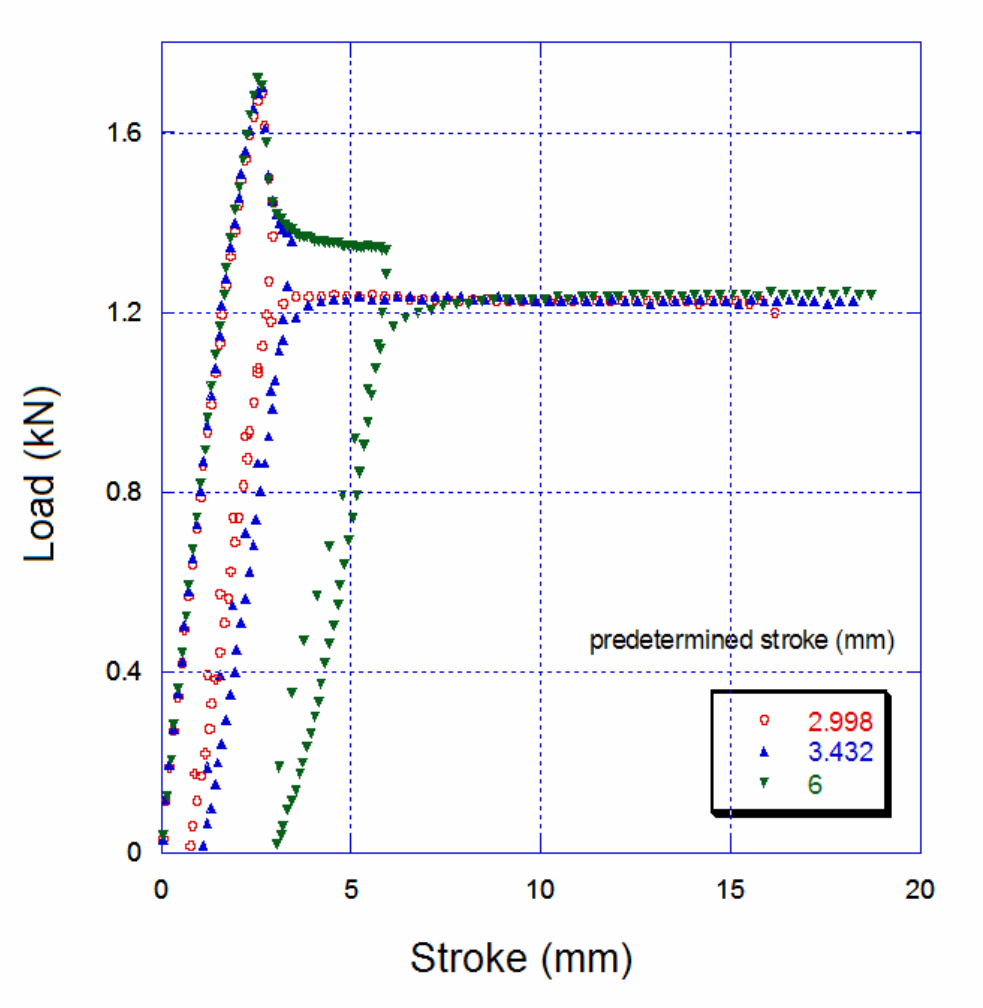

Fig. 4.13 Typical load-displacement curves for the second scenario

In the second loading stage, at 5mm/min, no peak was detected. The load-displacement curves rise to a certain level, and remain steady with a very gradual drop until fracture. The steady load level does not change with the predetermined stroke value. This is believed to be an indication of the lack of the second damage mechanism involved in the deformation process. Given the conclusion from the monotonic tests that shear

yielding is the dominant damage mechanism at the loading rate 60mm/min, it is reasonable to believe that crazing has been to some extent suppressed by the pre-existing shear yielding damage.

The results of multi-stage tensile tests are tabulated in Appendix 3. Note that for both scenarios, the total energy of fracture includes the unloading-reloading loop energy twice, therefore it is a summation of material toughness and energy dissipation during the unloading-reloading stage. The mean value and the standard deviation of the mechanical properties are listed in Table 4.3 and their variations with the predetermined stroke are illustrated in Figs. 4.14 and 4.15 for the first and second scenarios, respectively.

Table 4.3 Mechanical properties of ABS in multi-stage tensile tests of (a) scenario 1 and (b) scenario 2 with different predetermined strokes

(a)

Predetermined stroke (mm)		2.563	3.129	6
Total elongation (mm)	mean	11.8	11.8	11.5
	deviation	3.33	2.93	2.41
Total energy (J)	mean	15.1	15.0	14.7
	deviation	4.40	3.87	3.27
2nd stage maximum strength (MPa)	mean	36.0	35.2	34.5
	deviation	0.15	0.12	0.12
2nd stage elongation (mm)	mean	11.3	10.9	8.4
	deviation	3.33	2.94	2.42
2nd stage toughness (J)	mean	14.1	13.2	9.5
	deviation	4.40	3.87	3.25

(b)

Predetermined stroke (mm)		2.998	3.432	6
Total elongation (mm)	mean	16.8	20.7	18.8
	deviation	4.89	5.73	6.83
Total energy (J)	mean	20.1	25.0	23.2
	deviation	5.83	6.96	8.24
2nd stage elongation (mm)	mean	16.1	19.7	15.9
	deviation	4.90	5.73	6.85
2nd stage toughness (J)	mean	18.5	22.6	17.6
	deviation	5.84	7.08	8.26

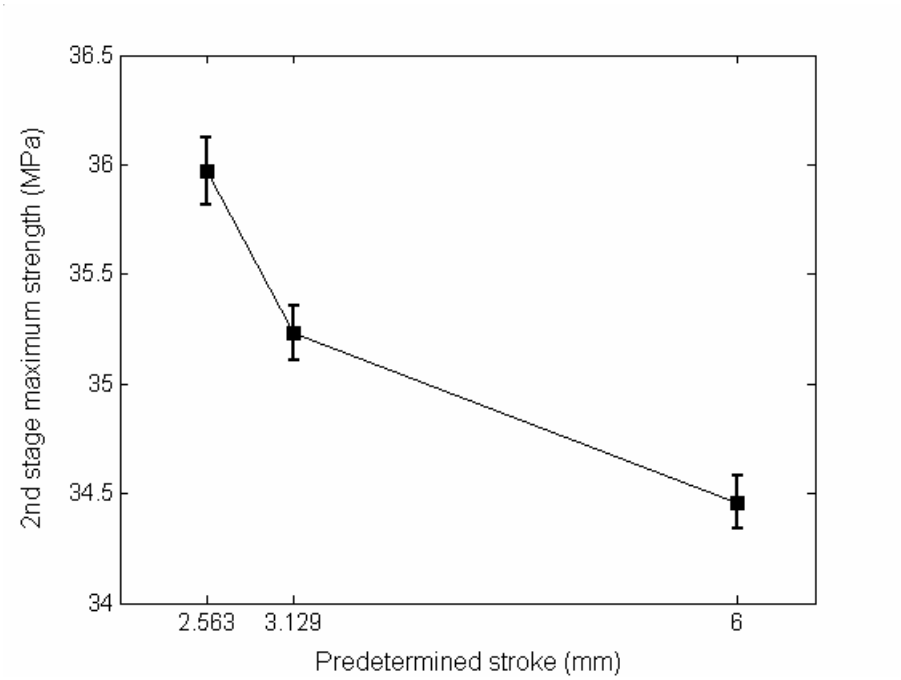
36.5
36
35.5
35
34.5
34
2nd stage maximum strength (MPa)
2.563
3.129
6
Predetermined stroke (mm)

(a)

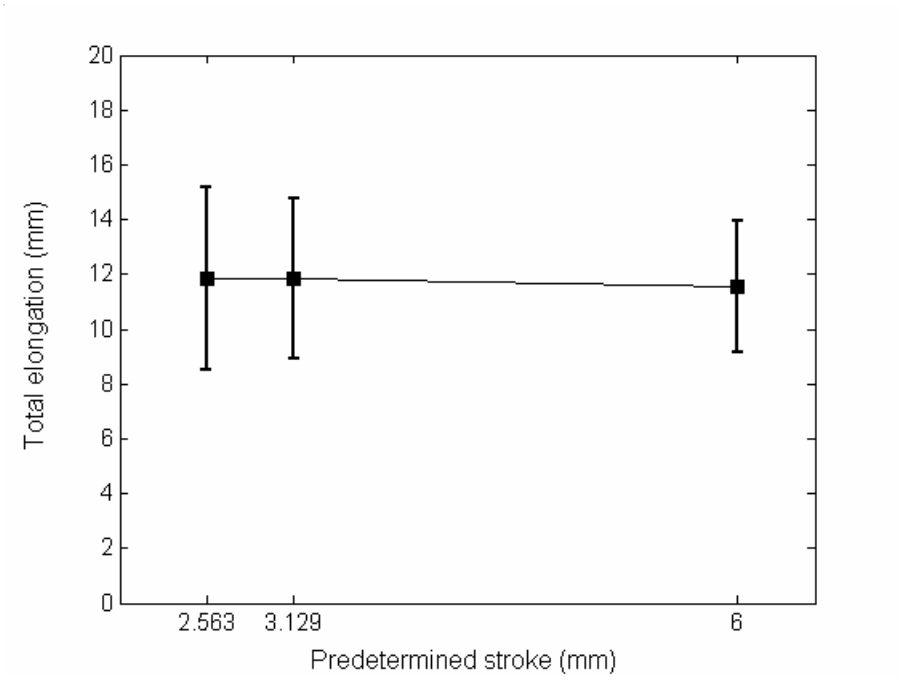
20
18
16
14
12
10
8
6
4
2
0
Total elongation (mm)
2.563
3.129
6
Predetermined stroke (mm)

(b)

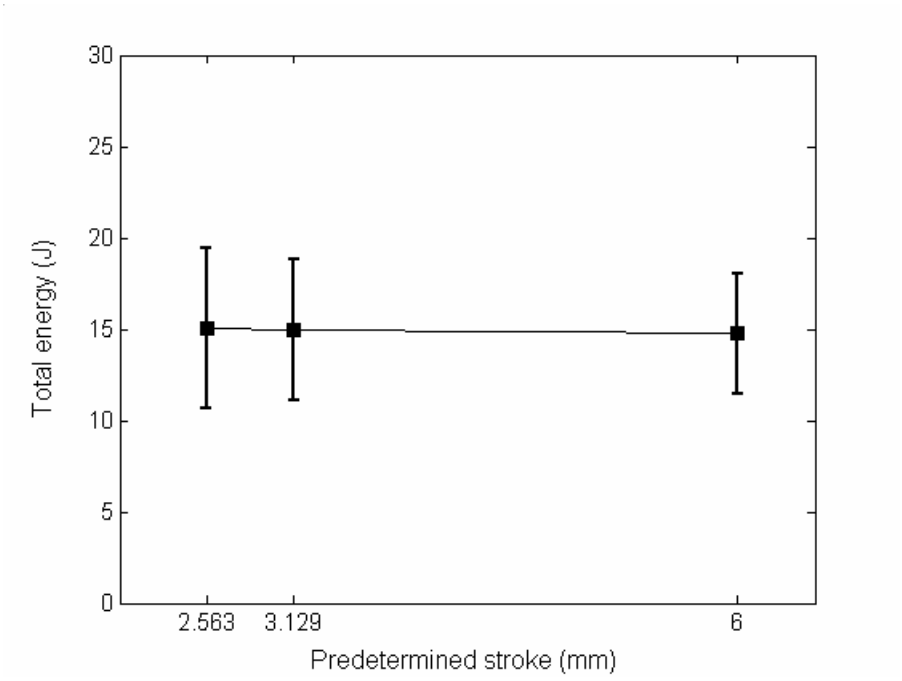
30
25
20
15
10
5
0
Total energy (J)
2.563
3.129
6
Predetermined stroke (mm)

(c)

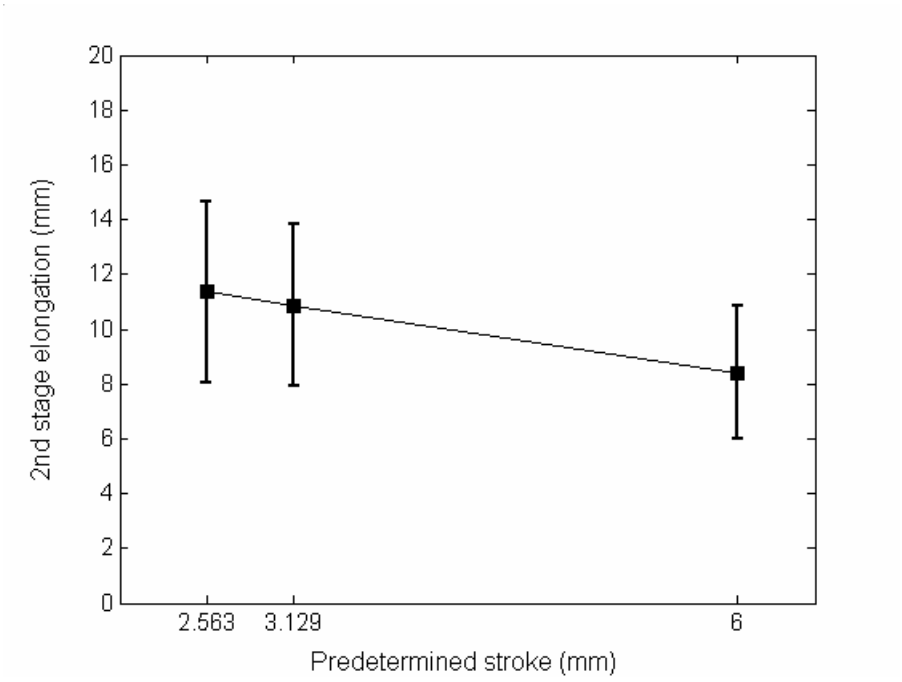
20
18
16
14
12
10
8
6
4
2
0
2nd stage elongation (mm)
2.563
3.129
6
Predetermined stroke (mm)

(d)

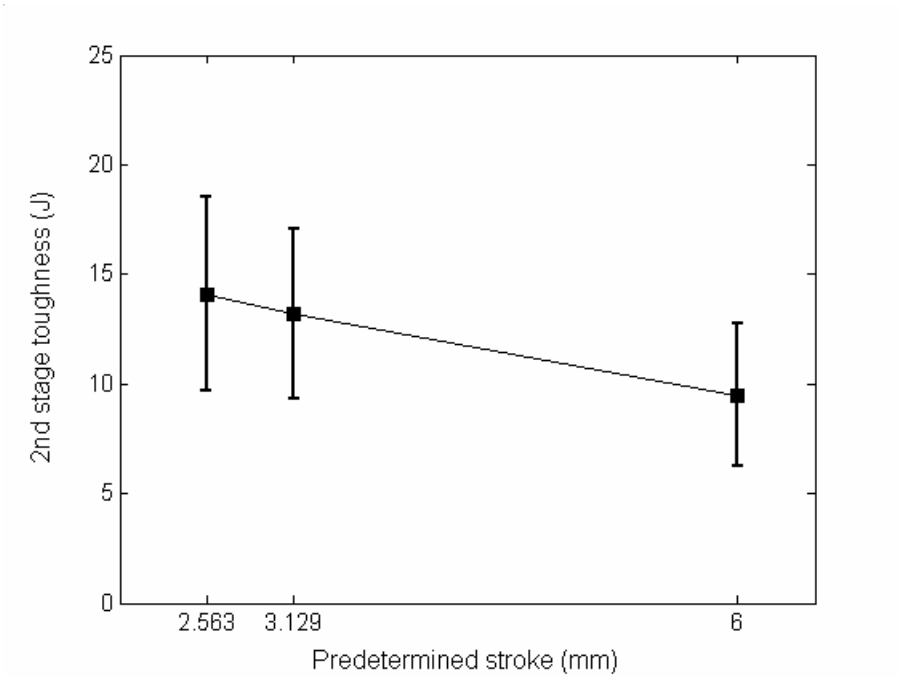

(e)

Fig. 4.14 Summary of multi-stage test results for scenario 1 (5-60mm/min): (a) 2nd stage maximum strength, (b) total elongation, (c) total energy, (d) 2nd stage elongation and (e) 2nd stage toughness

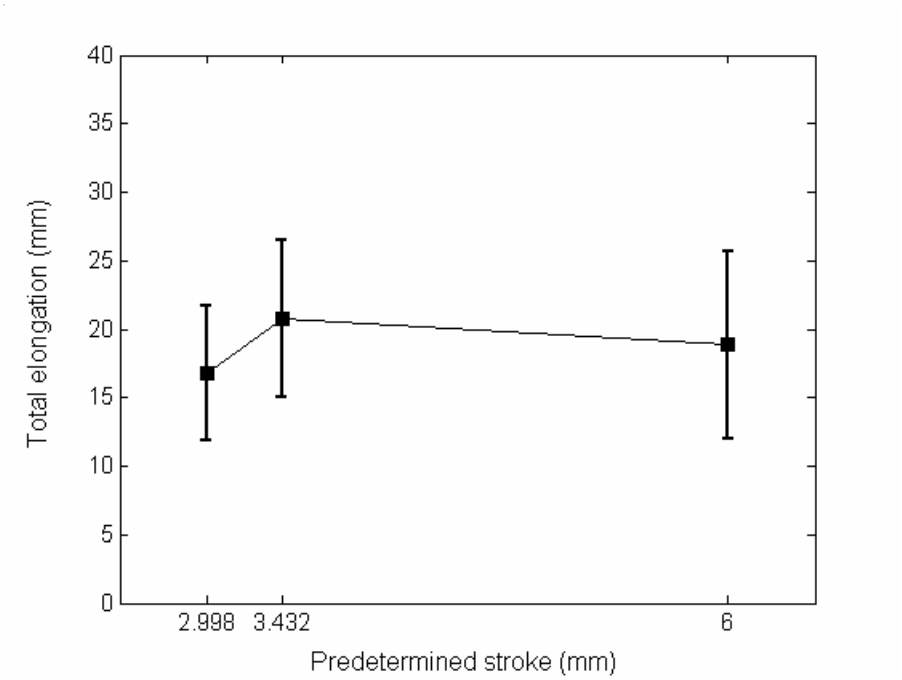

(a)

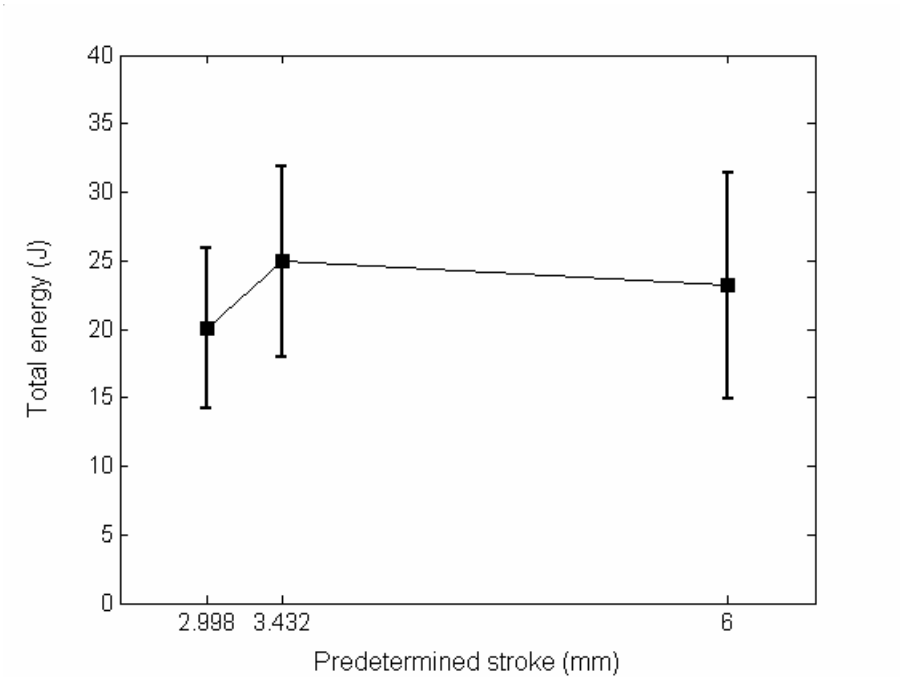
Total energy (J)
40
35
30
25
20
15
10
5
0
2.998
3.432
6
Predetermined stroke (mm)

(b)

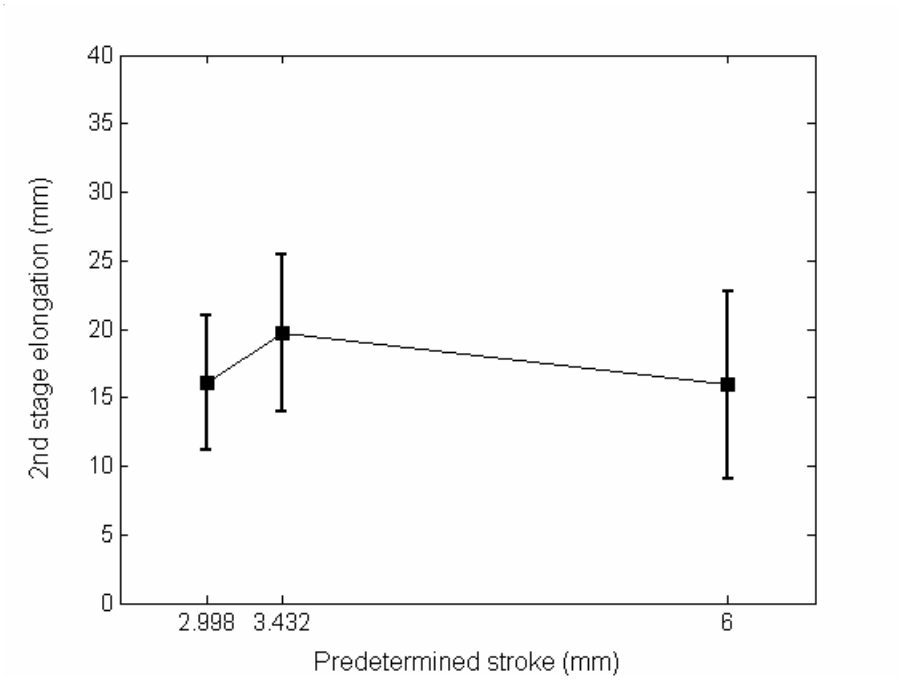
2nd stage elongation (mm)
40
35
30
25
20
15
10
5
0
2.998
3.432
6
Predetermined stroke (mm)

(c)

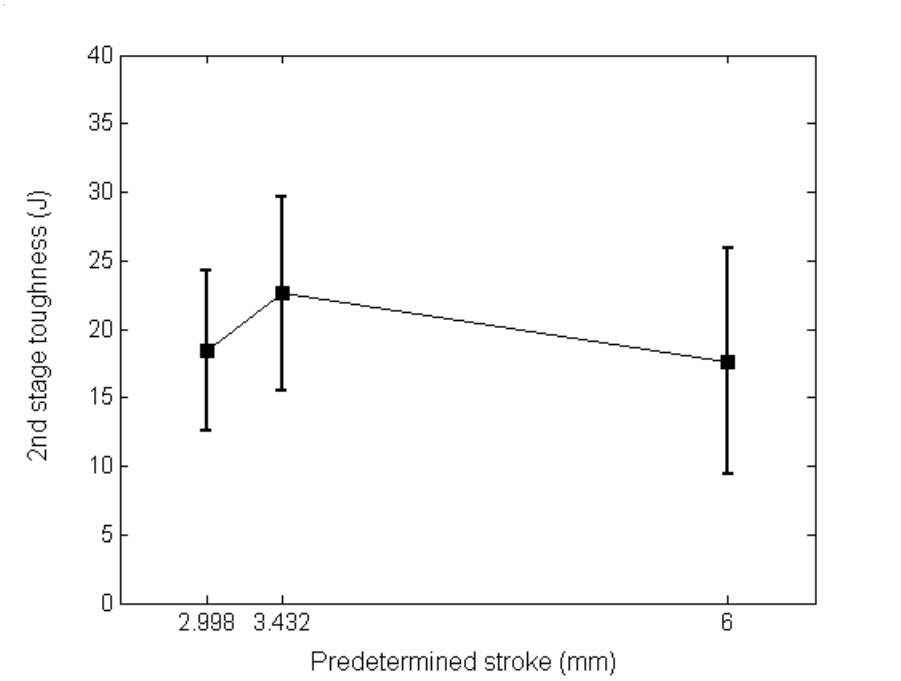

(d)

Fig. 4.15 Summary of multi-stage test results for scenario 2 (60-5mm/min): (a) total elongation, (b) total energy, (c) 2nd stage elongation and (d) 2nd stage toughness

For scenario 1, the second stage maximum strength shows a clear trend of decrease with the increase of the predetermined stroke. Its standard deviation also decreases in a similar manner, but in a smaller range. However, both the total elongation and the total energy remain almost unchanged for different predetermined strokes, with the standard deviations decreasing with the increase of the predetermined stroke. The mean values and the standard deviations of the total elongations for scenario 1 are very close to those of extension at break at the crosshead speed of 5mm/min in monotonic tests. Those values of the total energy for scenario 1 in the multi-stage tests also show the same range as the toughness at 5mm/min in the monotonic tests. The total energy for the former is slightly large compared to the latter, partly because it includes twice of the dissipated energy in the unloading-reloading loop. With the consideration of the energy dissipation being smallest for the predetermined stroke of 2.998mm and that the total energy decreases with the increase of the predetermined stroke, the toughness should actually improve through the introduction of the shear yielding in the second stage loading. Decrease of the

second stage elongation and toughness, as indicated by their mean values, is probably because of the increase of predetermined stroke that caused increase of the residual deformation. Their standard deviations, however, decrease, which is consistent with the trend of the standard deviations for the total elongation and energy.

A different trend was observed for scenario 2. The mean values of the total elongation and energy are slightly smaller than those values at the crosshead speed of 60mm/min in the monotonic tests. The variations of the total elongation and energy and the second stage elongation and toughness all do not show a monotonic trend of increase or decrease. They all have the largest values at the medium predetermined stroke of 3.432mm. This is relatively easy to understand for the second stage elongation and toughness due to two contradictory effects. That is, with more shear yielding damage introduced in the preloading stage, the material toughness is expected to increase. On the other hand, the increase damage with the increase of predetermined stroke tends to consume more of the energy absorption and reduce the residual toughness. However, a reasonable explanation for the variation trend of the total elongation and energy could not be suggested. The standard deviations of all above properties consistently increase with the increase of the predetermined stroke. This is probably caused by the increasing amount of shear yielding introduced in the preloading stage.

4.2.2 Weibull analysis

For each scenario of the multi-stage tests, the results of total energy and second stage toughness for each predetermined stroke were analyzed again based on two-parameter Weibull distribution and two-group mixed Weibull distribution. The evaluation results are summarized in Tables 4.4 and 4.5, and the unreliability and PDF curves are illustrated in Figs. 4.16, 4.17, 4.18 and 4.19.

Table 4.4 Two-parameter Weibull and two group mixed Weibull parameters for (a) total energy and (b) 2nd stage toughness for scenario 1

(a)

Predetermined stroke (mm)			2.563	3.129	6
Two-parameter Weibull	β		3.7	4.4	5.5
	η (J)		16.7	16.4	15.9
	ρ		0.99	0.99	0.96
Two group mixed Weibull	1st subpopulation	β_1	11.7	12.7	38.9
		η_1 (J)	15.7	13.5	13.1
		p_1	0.20	0.21	0.27
	2nd subpopulation	β_2	3.2	4.0	4.7
		η_2 (J)	17.0	17.1	16.7
		p_2	0.80	0.79	0.73
	ρ		0.99	0.99	0.99

(b)

Predetermined stroke (mm)			2.563	3.129	6
Two-parameter Weibull	β		3.4	3.8	3.3
	η (J)		15.7	14.6	10.5
	ρ		0.99	0.99	0.97
Two group mixed Weibull	1st subpopulation	β_1	10.7	11.3	28.6
		η_1 (J)	14.8	11.7	7.8
		p_1	0.22	0.19	0.24
	2nd subpopulation	β_2	2.9	3.5	3.1
		η_2 (J)	16.0	15.2	11.3
		p_2	0.78	0.81	0.76
	ρ		0.99	0.97	0.92

Table 4.5 Two-parameter Weibull and two group mixed Weibull parameters for (a) total energy and (b) 2nd stage toughness for scenario 2

(a)

Predetermined stroke (mm)			2.998	3.432	6
Two-parameter Weibull	β		4.3	4.7	3.2
	η (J)		21.9	27.1	25.8
	ρ		0.96	0.94	0.99
Two group mixed Weibull	1st subpopulation	β_1	10.9	29.7	4.2
		η_1 (J)	15.5	18.4	22.3
		p_1	0.35	0.27	0.33
	2nd subpopulation	β_2	4.3	5.3	2.7
		η_2 (J)	25.3	29.5	27.9
		p_2	0.65	0.73	0.67
	ρ		0.96	0.98	0.96

(b)

Predetermined stroke (mm)			2.998	3.432	6
Two-parameter Weibull	β		4.3	4.2	2.1
	η (J)		21.9	24.6	20.1
	ρ		0.96	0.93	0.99
Two group mixed Weibull	1st subpopulation	β_1	9.8	50.0	50.0
		η_1 (J)	13.8	15.8	20.0
		p_1	0.34	0.30	0.06
	2nd subpopulation	β_2	4.0	5.2	2.1
		η_2 (J)	23.6	27.6	19.9
		p_2	0.66	0.70	0.94
	ρ		0.96	0.93	1.00

Predetermined stroke: 2.563mm

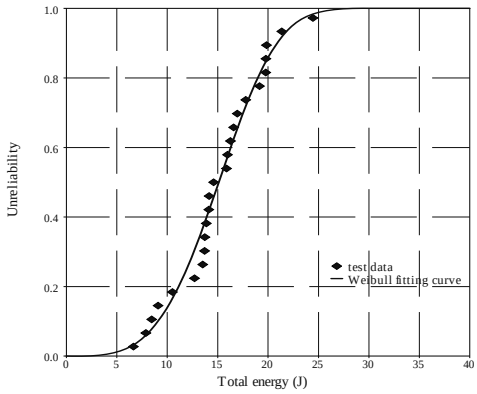

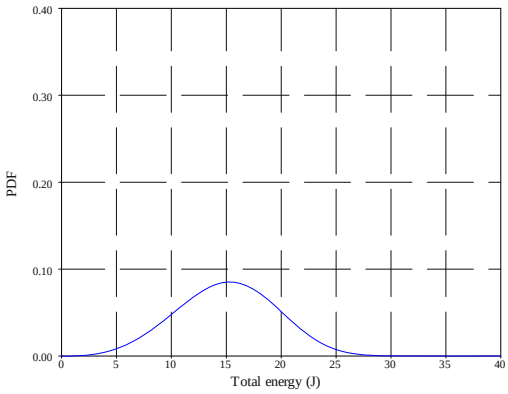

Predetermined stroke: 3.129mm

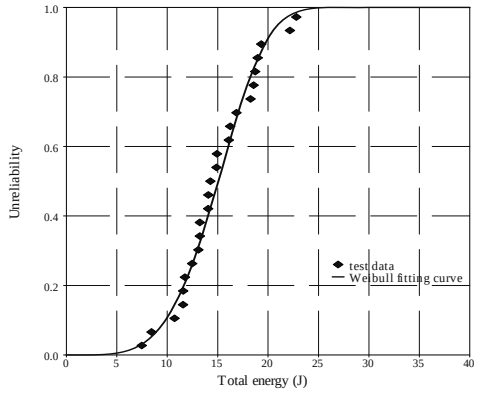

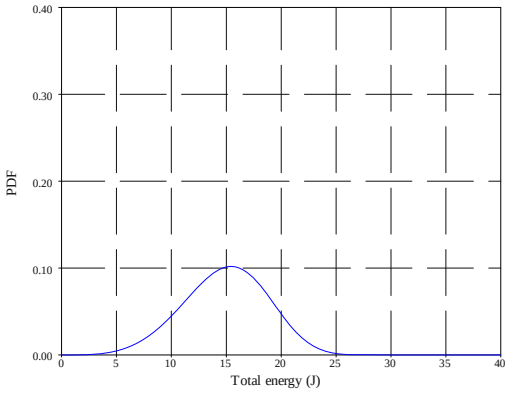

Predetermined stroke: 6mm

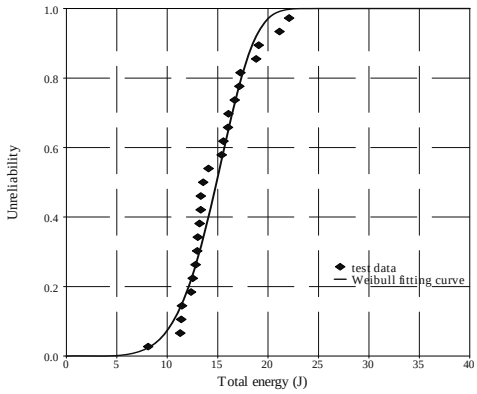

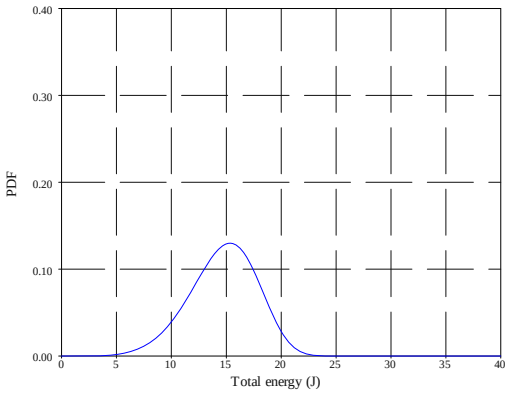

(a)

Predetermined stroke: 2.563mm

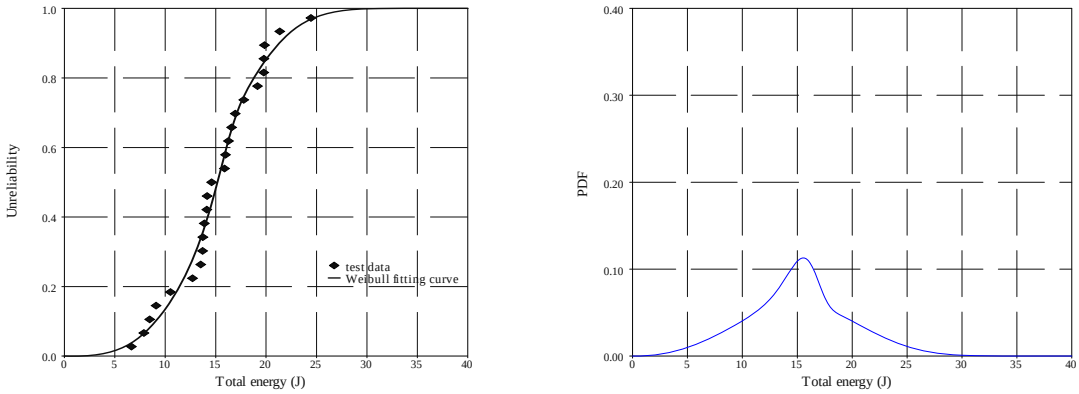

Predetermined stroke: 3.129mm

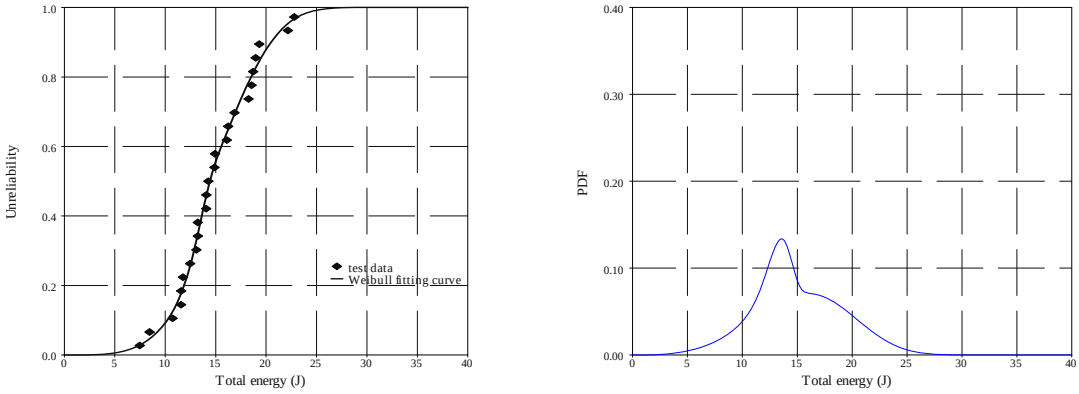

Predetermined stroke: 6mm

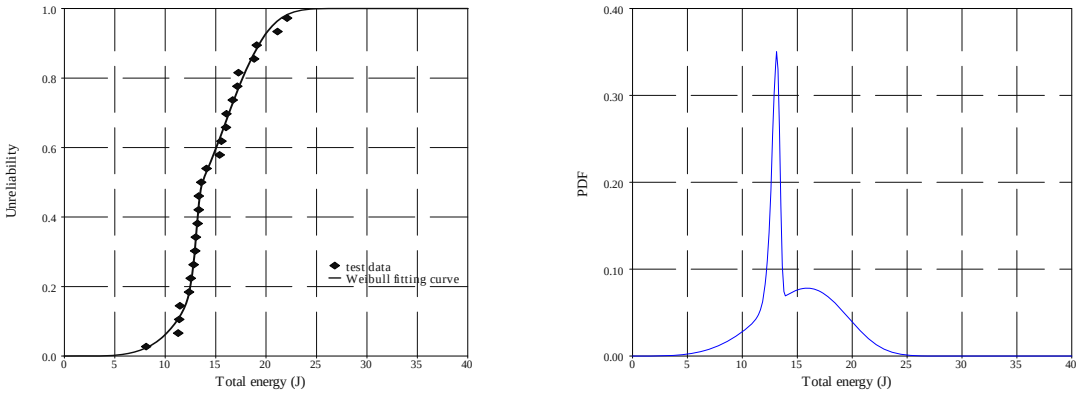

(b)

Fig. 4.16 Results of unreliability and PDF on total energy for scenario 1 by (a) two-parameter Weibull distribution and (b) two group mixed Weibull distribution

Predetermined stroke: 2.563mm

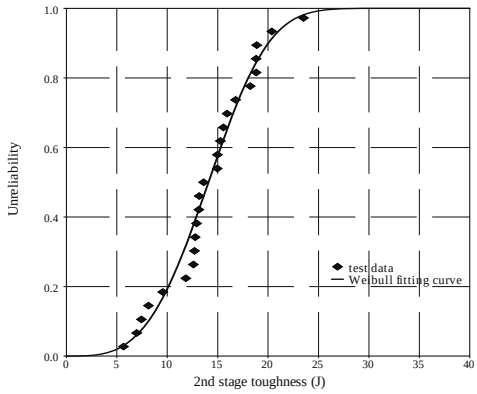

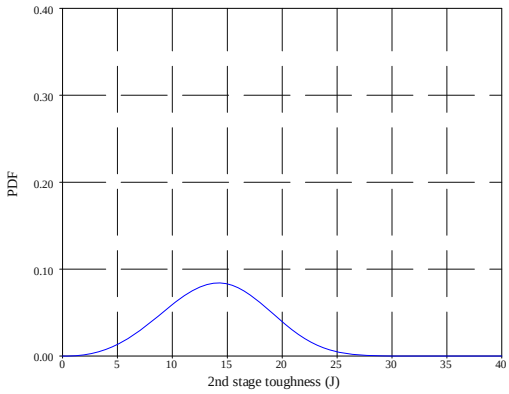

Predetermined stroke: 3.129mm

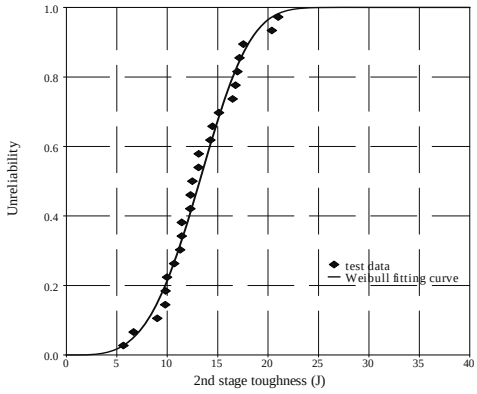

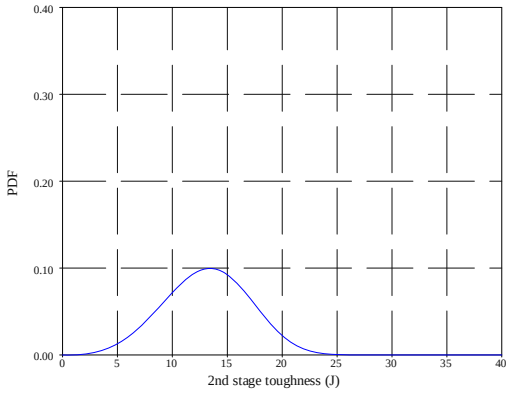

Predetermined stroke: 6mm

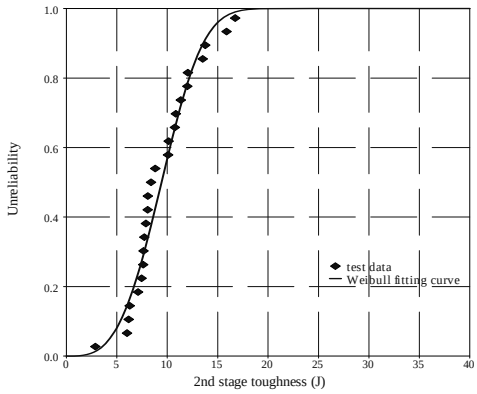

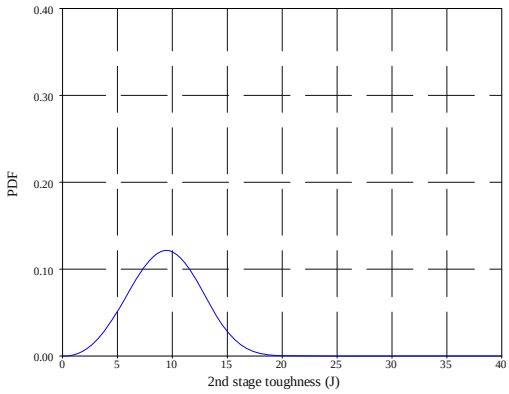

(a)

Predetermined stroke: 2.563mm

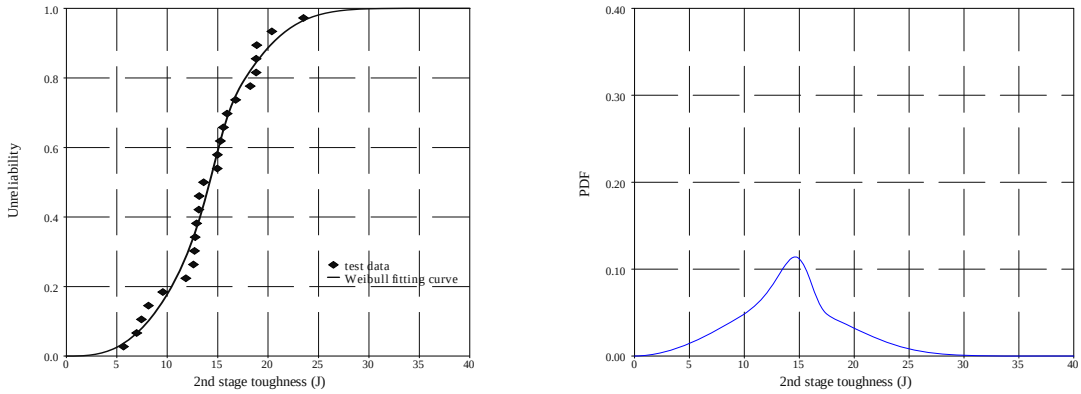

Predetermined stroke: 3.129mm

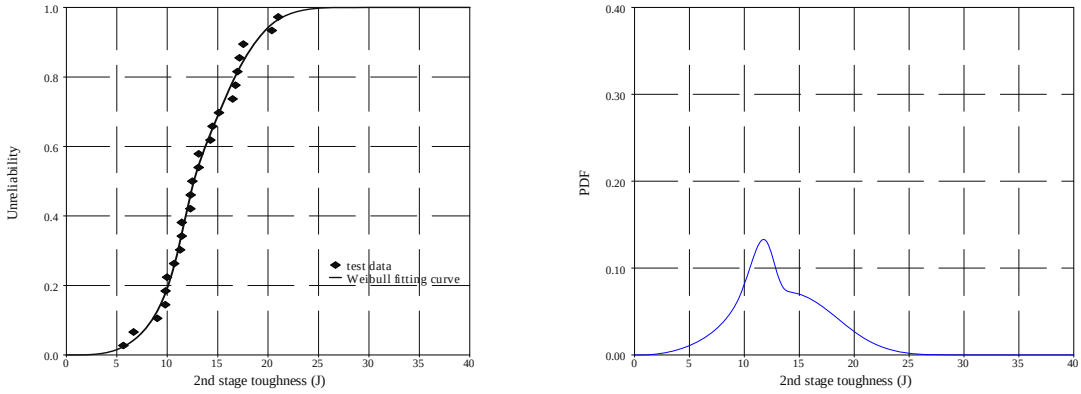

Predetermined stroke: 6mm

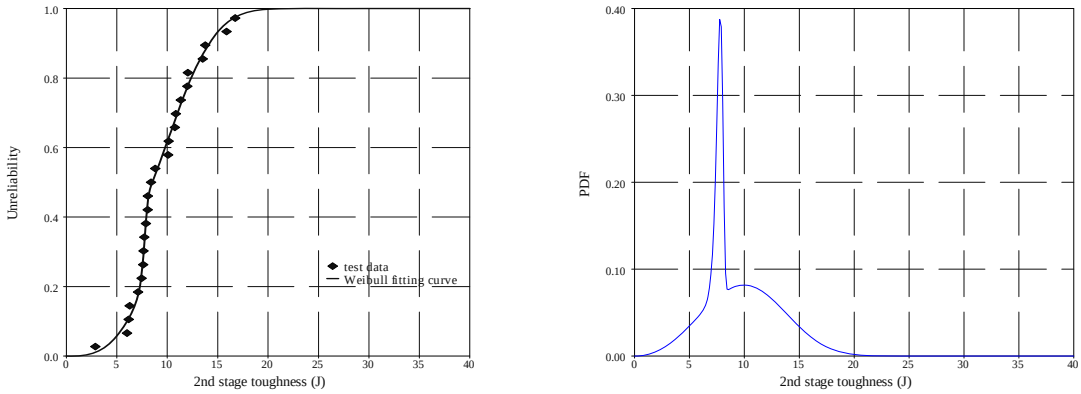

(b)

Fig. 4.17 Results of unreliability and PDF on 2nd stage toughness for scenario 1 by (a) two-parameter Weibull distribution and (b) two group mixed Weibull distribution

Predetermined stroke: 2.998mm

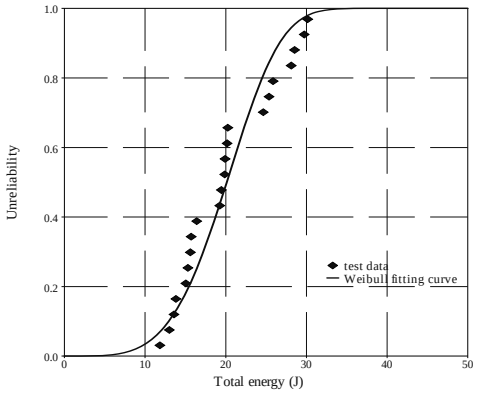

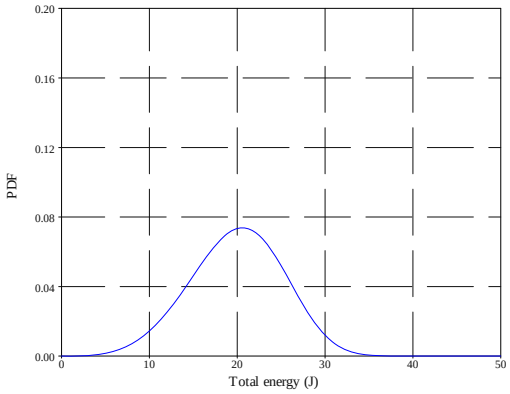

Predetermined stroke: 3.432mm

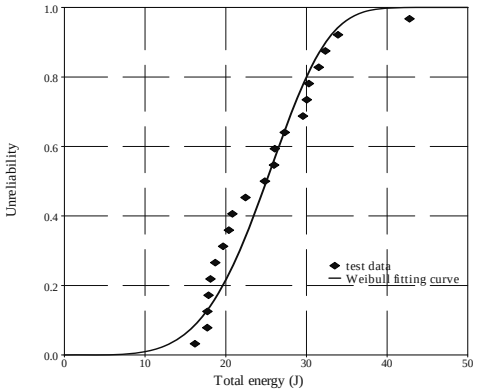

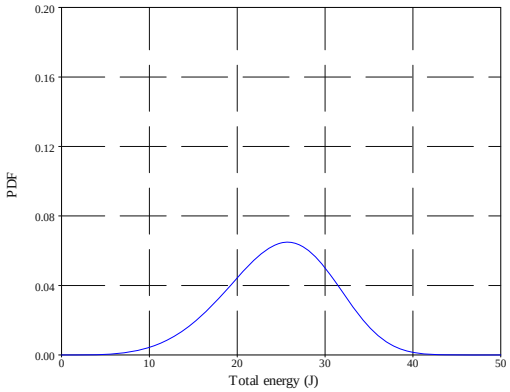

Predetermined stroke: 6mm

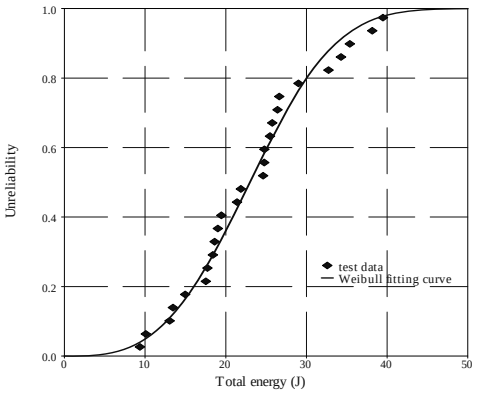

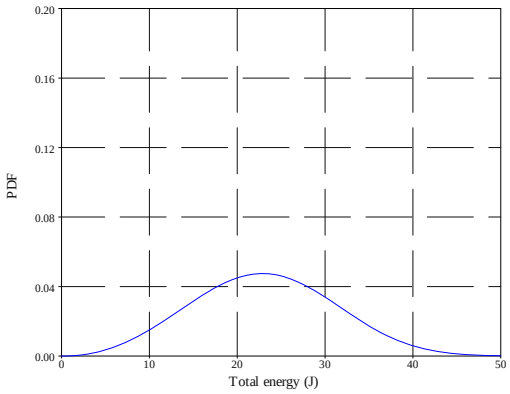

(a)

Predetermined stroke: 2.998mm

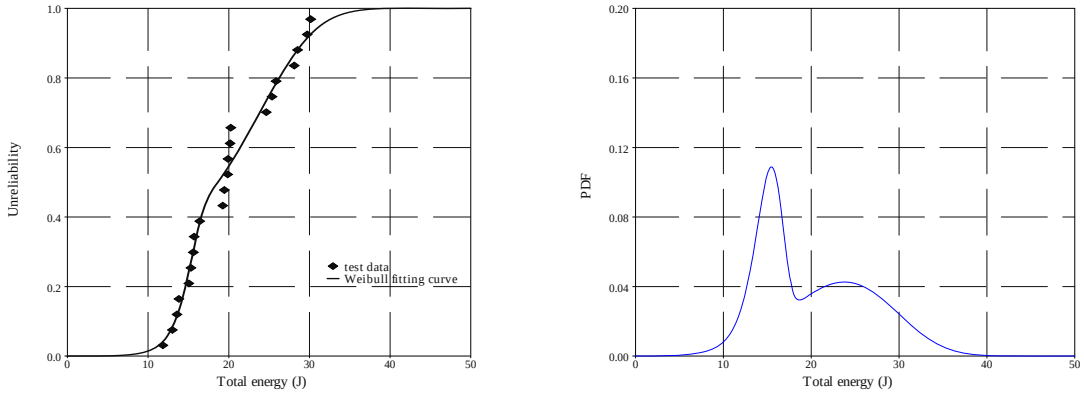

Predetermined stroke: 3.432mm

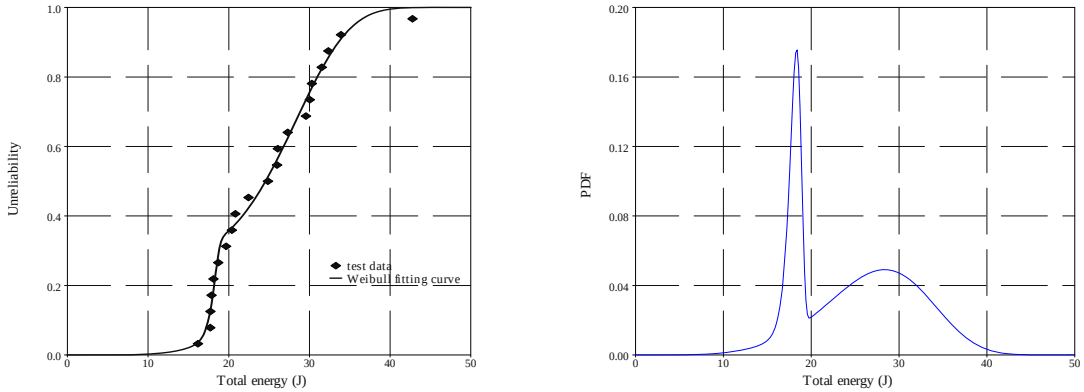

Predetermined stroke: 6mm

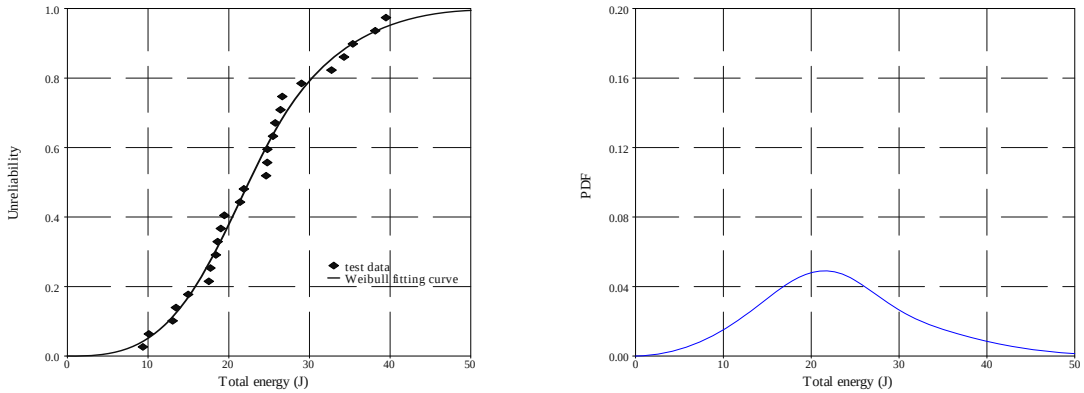

(b)

Fig. 4.18 Results of unreliability and PDF on total energy for scenario 2 by (a) two-parameter Weibull distribution and (b) two group mixed Weibull distribution

Predetermined stroke: 2.998mm

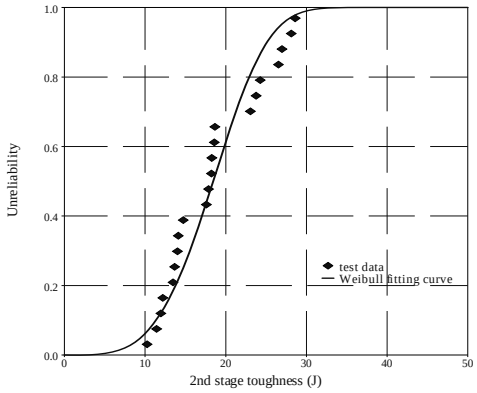

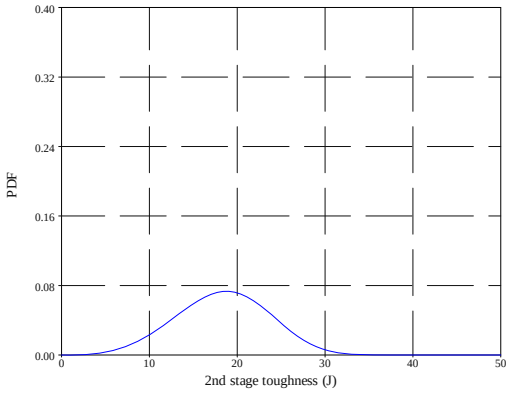

Predetermined stroke: 3.432mm

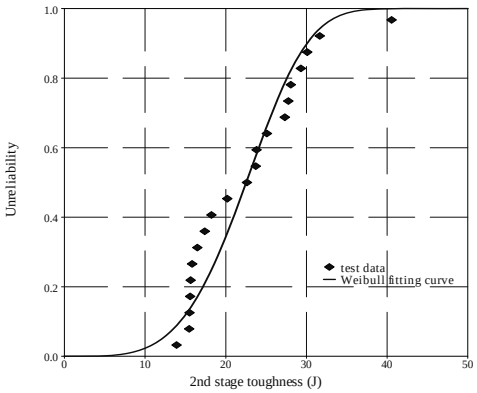

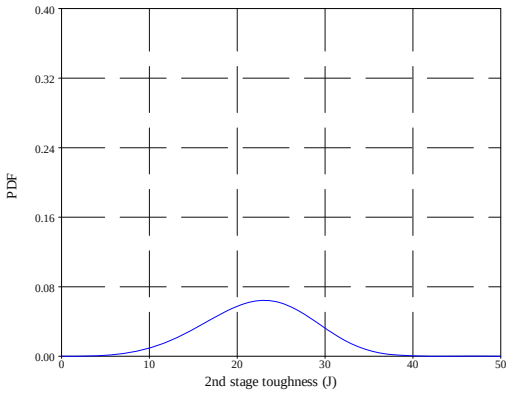

Predetermined stroke: 6mm

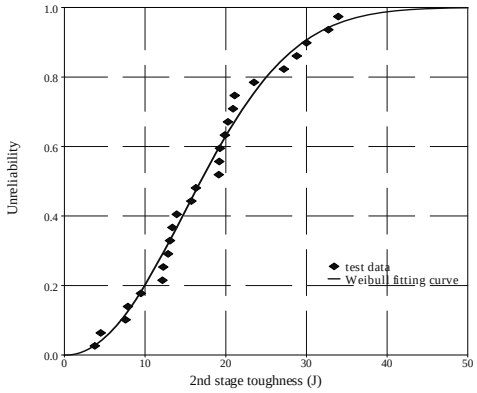

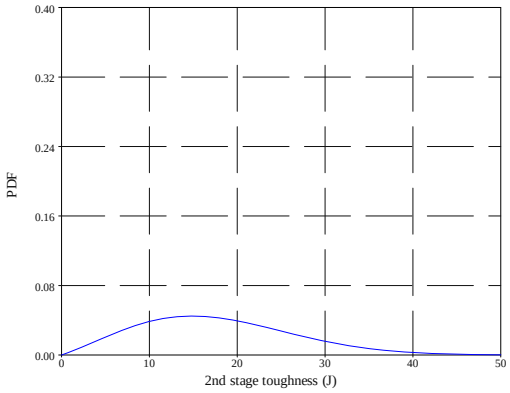

(a)

Predetermined stroke: 2.998mm

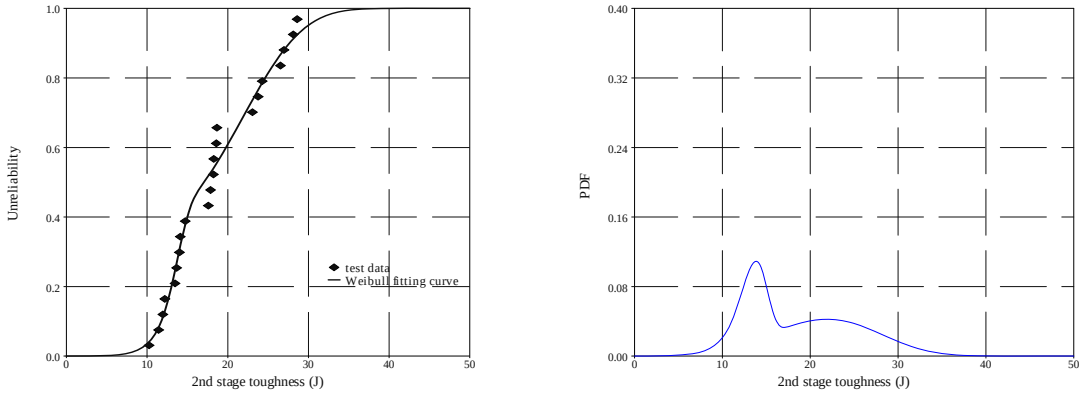

Predetermined stroke: 3.432mm

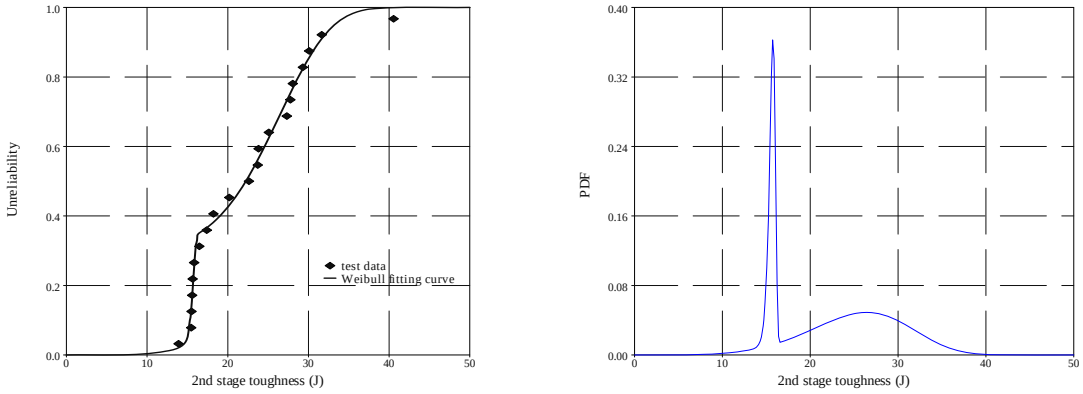

Predetermined stroke: 6mm

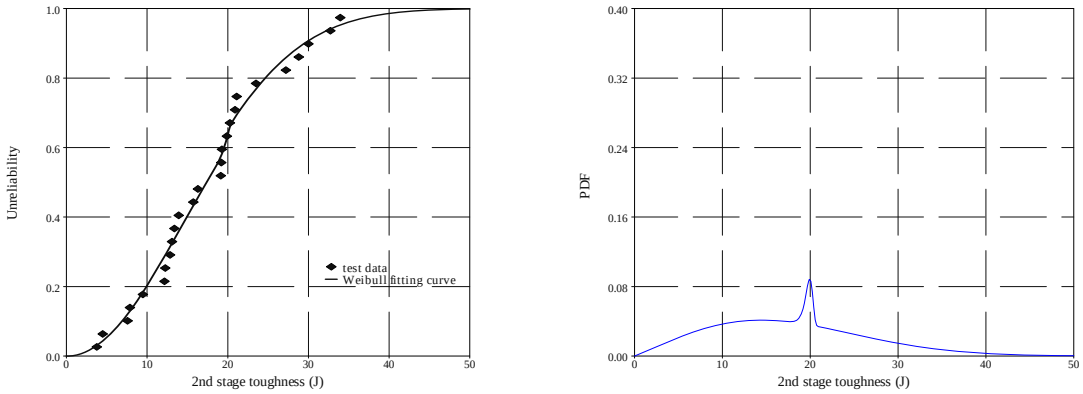

(b)

Fig. 4.19 Results of unreliability and PDF on 2nd stage toughness for scenario 2 by (a) two-parameter Weibull distribution and (b) two group mixed Weibull distribution

Again, both the two-parameter Weibull distribution and two group mixed Weibull distribution can provide acceptable fitting to the test data to describe the distribution of total energy and second stage toughness for each scenario at various predetermined strokes in the multi-stage tests.

For scenario 1, the results of total energy and second stage toughness are quite similar except that the characteristic life of total energy almost remains constant and that of the second stage toughness decreases with the increase of the predetermined stroke. This can be noticed by similar distribution characteristics and the position shift of the PDF curves. When using the two-parameter Weibull distribution, the unreliability curve becomes steeper and the broadness of the PDF curve becomes smaller as the predetermined stroke increases. When the two group mixed Weibull distribution is applied, the unreliability of test data can be better described. With the increase of the predetermined stroke, a peak can be seen to gradually emerge from the PDF and become sharper. The percentage of the corresponding subpopulation has a trend of increase, too. This is identified as the increasing contribution of crazing introduced in the preloading stage to the toughness distribution.

For scenario 2, the characteristic lives of total energy and second stage toughness do not show a monotonic trend with the increase of the predetermined stroke. This is in agreement with the mean value results. When using two-parameter Weibull distribution, the broadness of the PDF curves increases with the predetermined stroke. When using two-group mixed Weibull distribution to analyze the total energy, a relatively sharp peak and a broad distribution curve coexist in the PDF plots for the predetermined strokes of 2.998 and 3.432mm. When the predetermined stroke increases to 6mm, however, only one broad distribution curve can be observed even using two group mixed Weibull distribution. That is, with the increasing amount of shear yielding damage introduced in the preloading stage, crazing can no longer be identified. The portion of the subpopulation representing crazing has a trend of decreasing and then increasing at the predetermined stroke is 6mm, the shape and scale parameters of the two subpopulations are so close that they cannot be distinguished as two groups. The analysis result for the second stage toughness is similar except that the portion of the subpopulation representing crazing consistently decreases and a very small peak can be identified in the

PDF curve for the predetermined stroke of 6mm. The distribution characteristics still indicate the dominancy of shear yielding which to some extent suppresses crazing.

The results of unreliability are further compared based on tw- group mixed Weibull analysis on the total energy and second stage toughness for different predetermined strokes for scenario 1 (Figs. 4.20 and 4.21) and scenario 2 (Figs. 4.22 and 4.23).

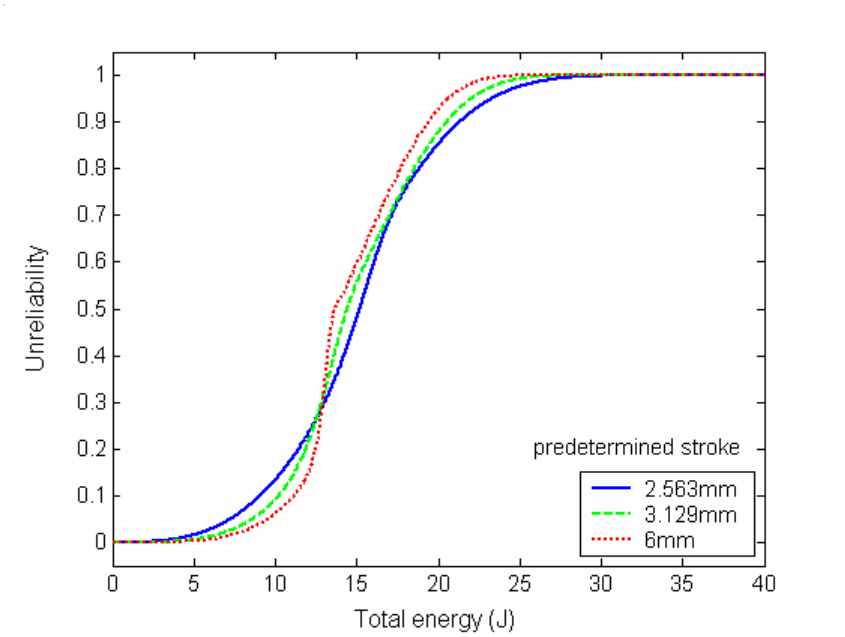

(a)

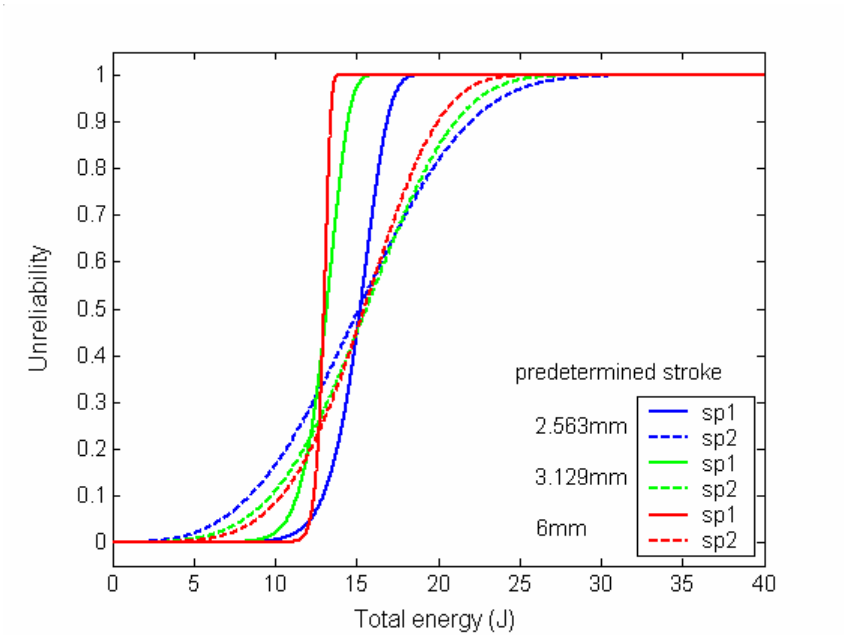

(b)

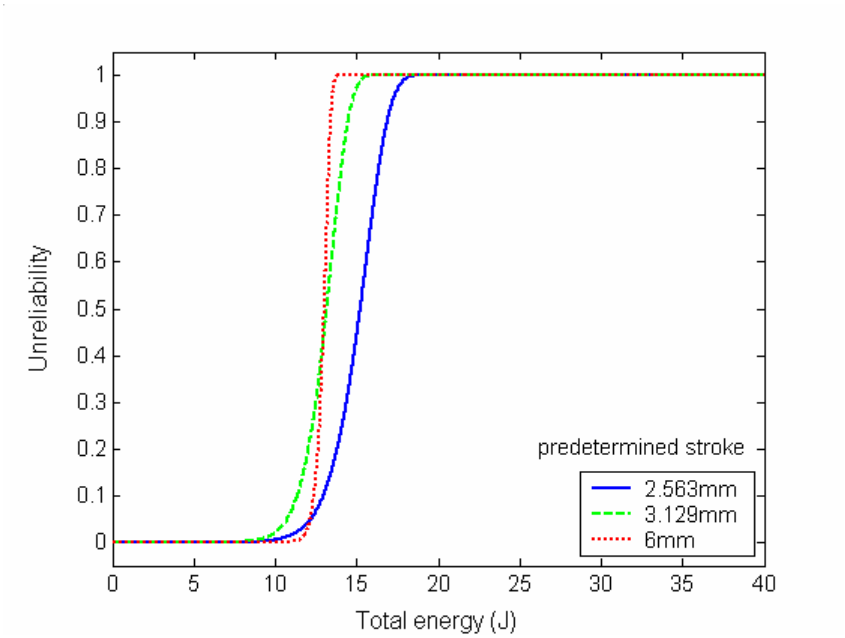

(c)

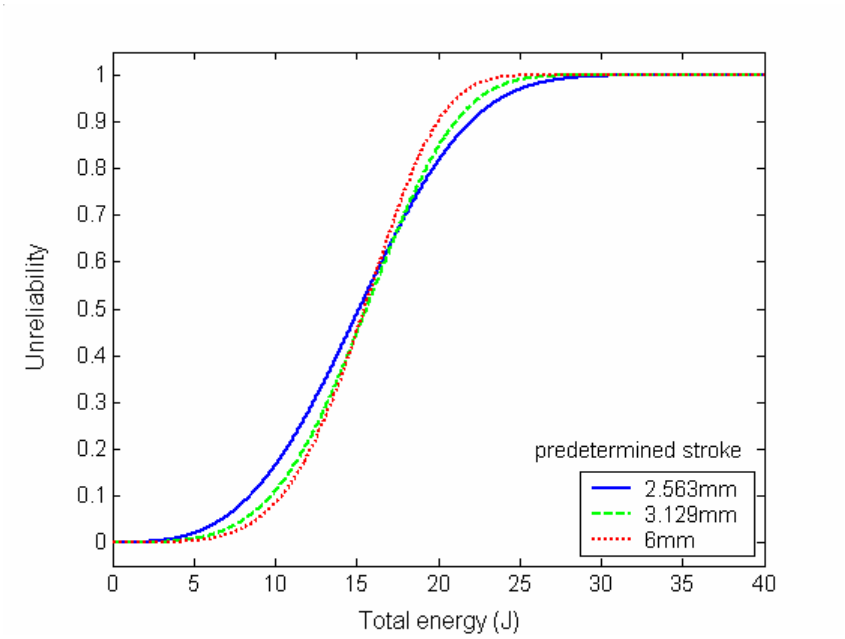

(d)

Fig. 4.20 Unreliability results of (a) mixed group distributions, (b) all subpopulations, (c) 1st subpopulations and (d) 2nd subpopulations of total energy for different predetermined strokes for scenario 1

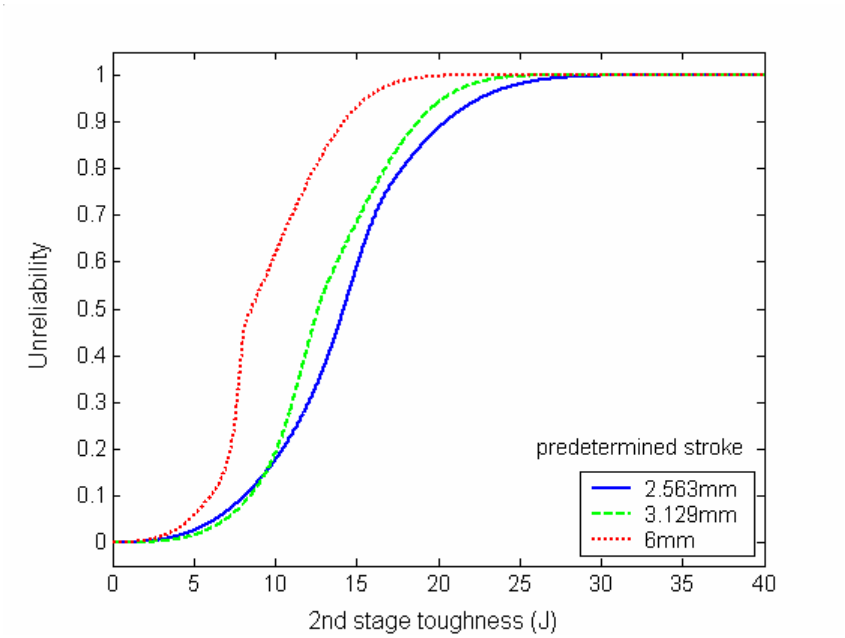
Unreliability
2nd stage toughness (J)
predetermined stroke
2.563mm
3.129mm
6mm

(a)

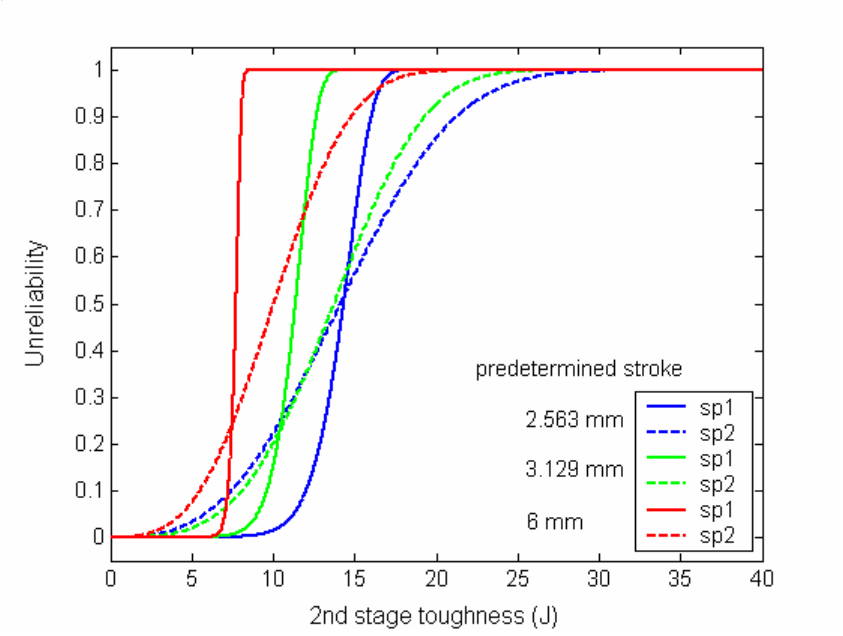
Unreliability
2nd stage toughness (J)
predetermined stroke
2.563 mm
3.129 mm
6 mm
sp1
sp2
sp1
sp2
sp1
sp2

(b)

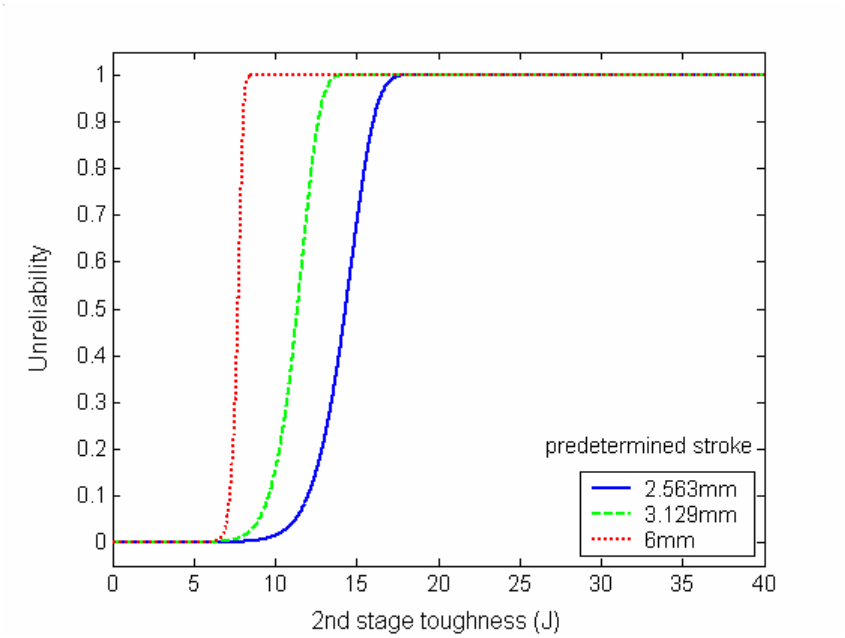

(c)

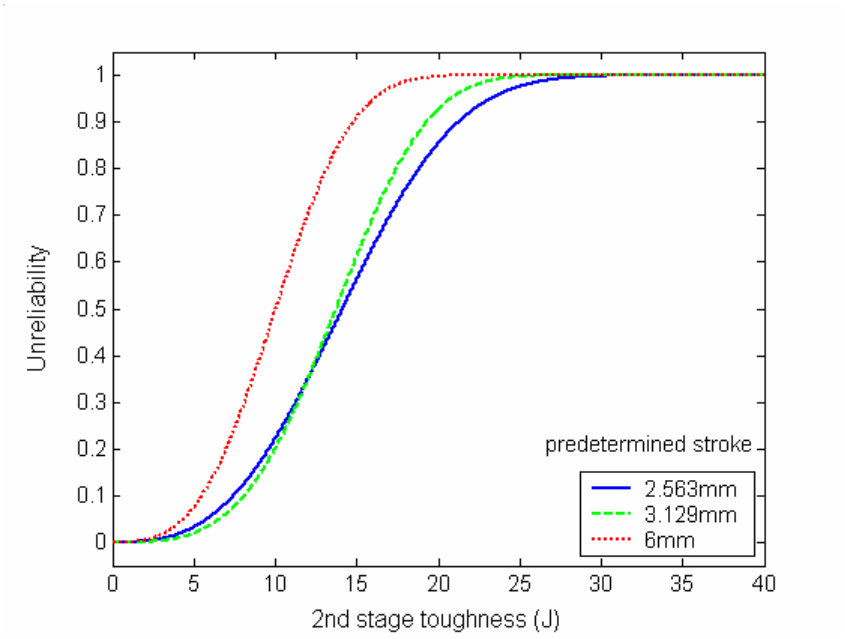

(d)

Fig. 4.21 Unreliability results of (a) mixed group distributions, (b) all subpopulations, (c) 1st subpopulations and (d) 2nd subpopulations of 2nd stage toughness for different predetermined strokes for scenario 1

Although the unreliabilities of total energy for different predetermined strokes are very similar, a trend of the increase of the steepness of the curve with the increase of the predetermined stroke can still be observed. This is more obvious in the comparison of the second stage toughness. For which the unreliability curve shifts to the left, indicating the decrease of characteristic life. For either the total energy or the second stage toughness, when all subpopulations are plotted, the unreliability curves can be classified into two groups with distinctive steepness. One group, plotted in solid lines in Fig. 4.21(b), represents the first subpopulations, for the contribution from crazing. The other group in dashed lines with much gentler steepness represents the second subpopulations, which is believed to be from shear yielding. With increasing predetermined stroke, thus more crazing damage introduced in the preloading stage, both curves in the first and second subpopulation become steeper and the characteristic life tends to become shorter.

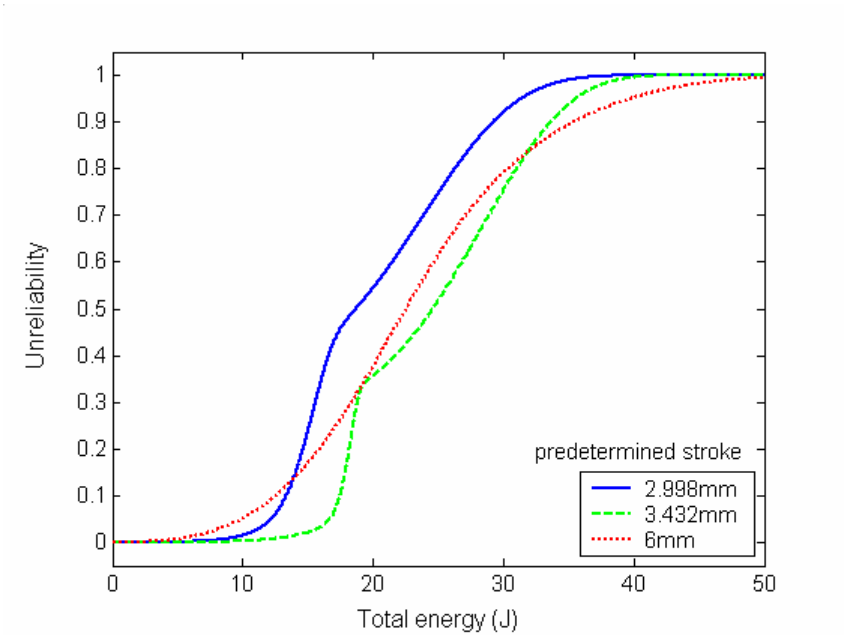

(a)

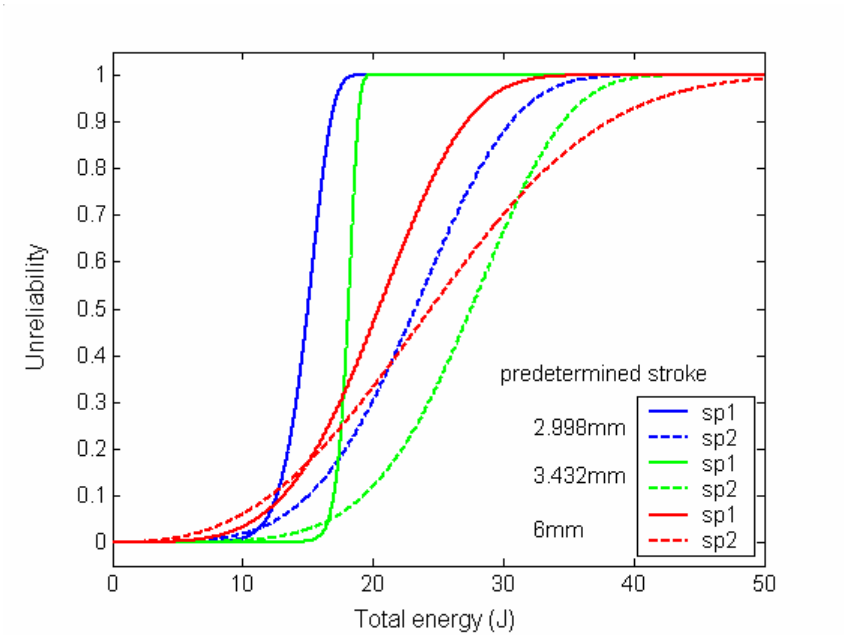
Unreliability
Total energy (J)
predetermined stroke
2.998mm
3.432mm
6mm
sp1
sp2
sp1
sp2
sp1
sp2

(b)

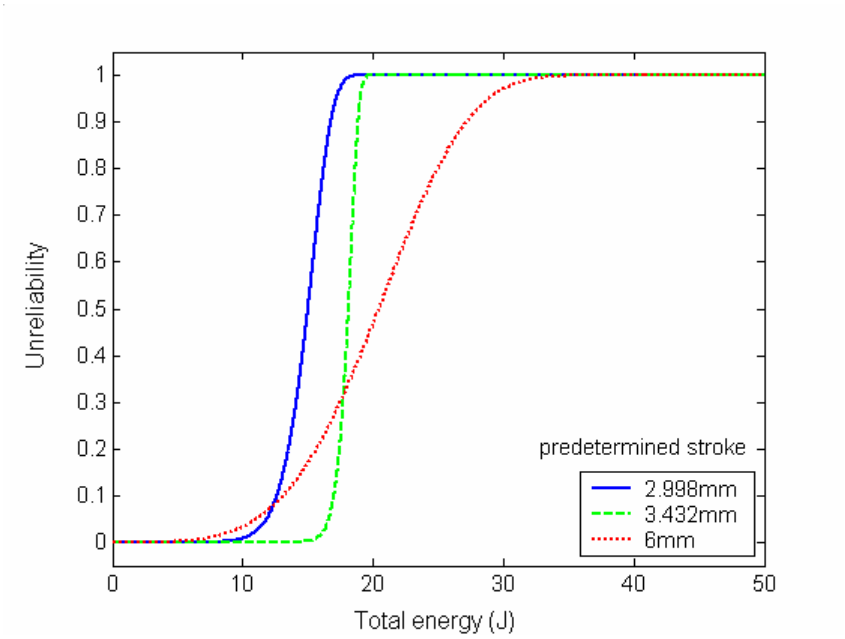
Unreliability
Total energy (J)
predetermined stroke
2.998mm
3.432mm
6mm

(c)

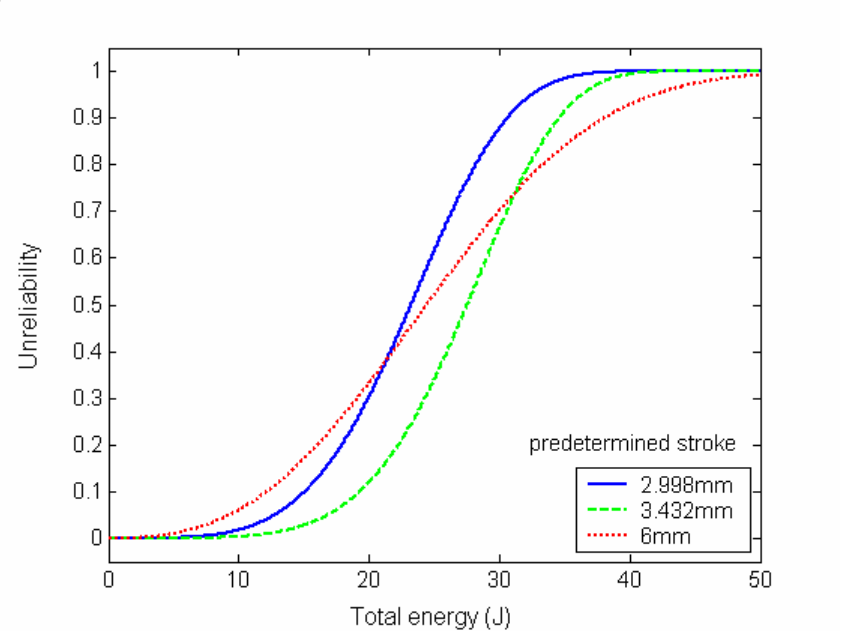

(d)

Fig. 4.22 Unreliability results of (a) mixed group distributions, (b) all subpopulations, (c) 1st subpopulations and (d) 2nd subpopulations of total energy for different predetermined strokes for scenario 2

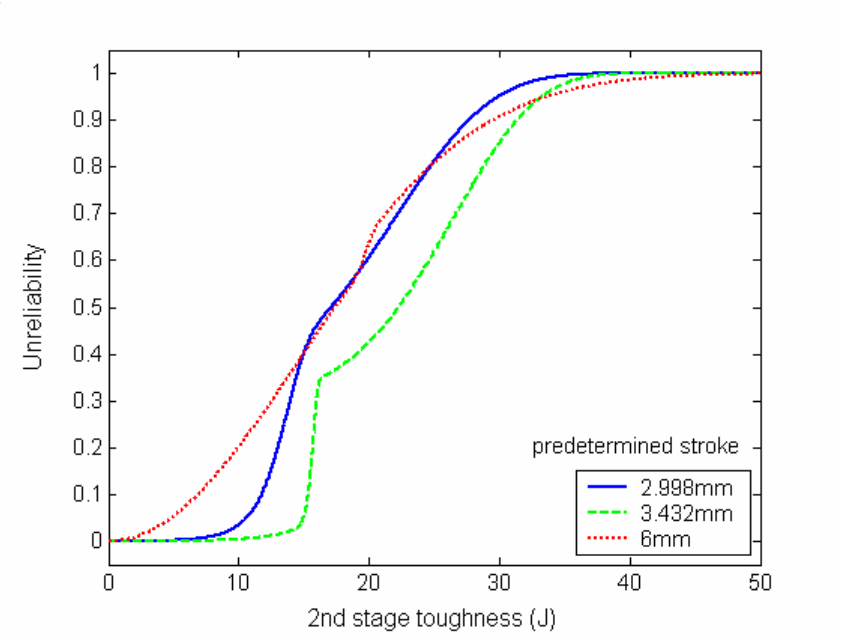

(a)

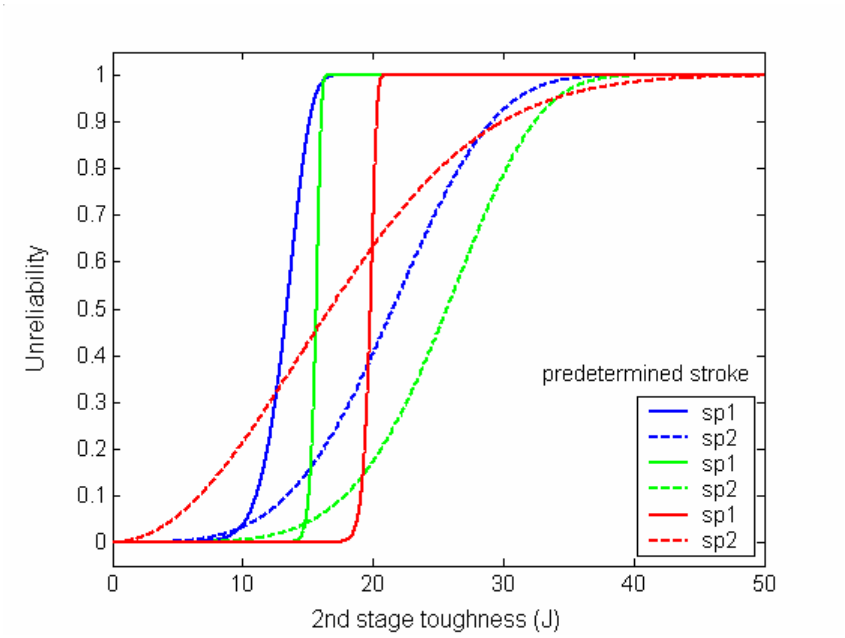
Unreliability
2nd stage toughness (J)
predetermined stroke
sp1
sp2
sp1
sp2
sp1
sp2

(b)

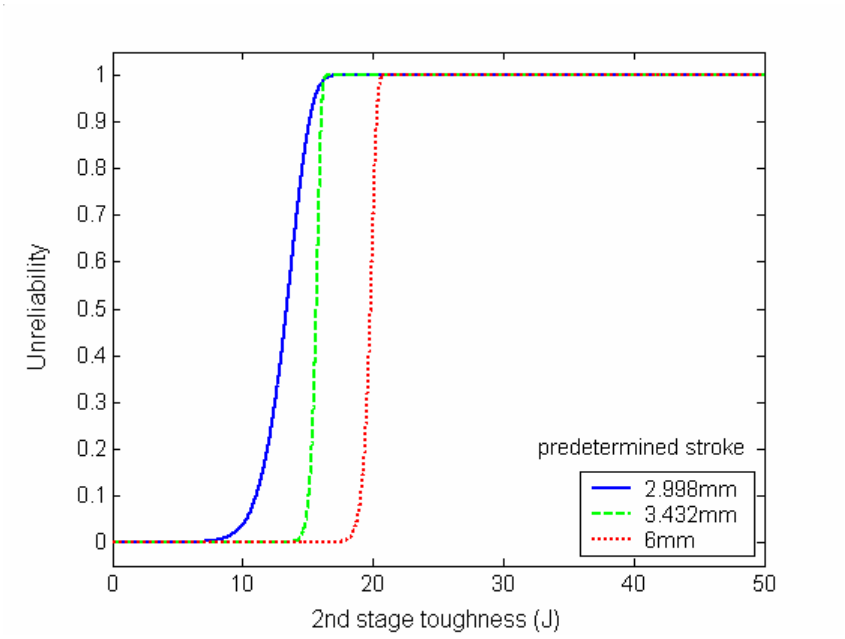
Unreliability
2nd stage toughness (J)
predetermined stroke
2.998mm
3.432mm
6mm

(c)

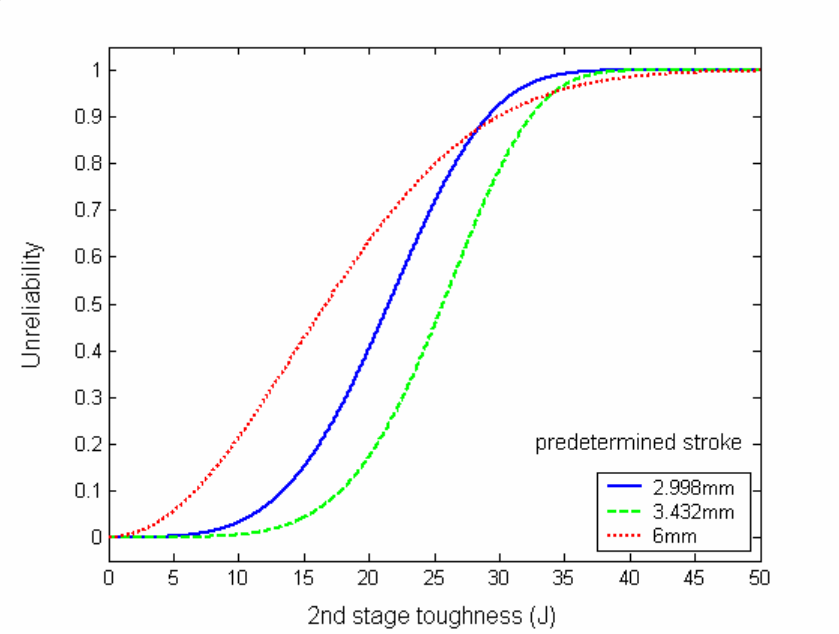

(d)

Fig. 4.23 Unreliability results of (a) mixed group distributions, (b) all subpopulations, (c) 1st subpopulations and (d) 2nd subpopulations of 2nd stage toughness for different predetermined strokes for scenario 2

For scenario 2, the total energy and the second stage toughness do not have a monotonic trend with the increase of the predetermined stroke. But it has been noticed that when the predetermined stroke is 6mm, the unreliability curves are much smoother and gentler. When the subpopulation is considered for the total energy, Fig. 4.22 (b), the curves can be classified as two categories of different steepness. Note that both curves for the predetermined stroke of 6mm are in the group of gentle steepness. For the second stage toughness, the classification can still be based on the first subpopulations and second subpopulations. But note that the portion of the first subpopulation for the predetermined stroke of 6mm is fairly small. It is believed that at this point crazing has been sufficiently suppressed to allow the deformation to be dominated by shear yielding.

4.3 Discussion

It has long been accepted that difference of the two mechanisms, crazing and shear yielding, lies in that the crazing-dominant failure is more brittle and the shear-yielding-

dominant damage tends to improve material toughness. Our results also supports those findings and suggest, more importantly, that the major difference between crazing and shear yielding is their effect on distinctive distribution characteristics of toughness. This is probably due to the sensitivity of the two mechanisms to defects or mechanical testing conditions or both. In terms of the PDF curve, crazing can be identified by a relatively sharp peak and shear yielding a broad distribution curve. Therefore, the crazing-dominant failure is expected to be more consistent than the shear-yielding-dominant failure, making the latter difficult to predict its reliability, especially when the number of tests conducted is small. Dominancy between the two mechanisms is affected by the test conditions, i.e. loading rate in the monotonic tensile tests and preloading stroke in the multi-stage tensile tests. The coexistence of both mechanisms can be identified and their contribution to the deformation can be quantified using two-group mixed Weibull distribution. Transition of the dominancy of the damage mechanisms has also been observed. This suggests that variation of test conditions changes toughness distribution or reliability of its prediction.

Chapter 5 Conclusions

In this study, Weibull statistics was applied to characterize the data scattering of mechanical properties for a rubber-toughened polymer, poly(acrylonitrile butadiene styrene) (ABS) in monotonic tensile tests and multi-stage tensile tests. Both the two-parameter Weibull and the two-group mixed Weibull distribution were proven effective in describing the data distributions. More importantly, the involvement of two deformation mechanisms, crazing and shear yielding, can be identified in ABS and quantified through the two-group mixed Weibull evaluation on toughness.

In the monotonic tensile tests, loading rate was found to be able to vary the involvement of each mechanism in the deformation process. The dominant mechanism changed from crazing to shear yielding by increasing the crosshead speed from 5 to 60mm/min. When failure is dominated by crazing, the material is relatively brittle with small values for the extension at break and toughness. Shear yielding generates a relatively ductile failure, and the corresponding properties increase in value significantly. This is consistent with results available in the literature. Based on the data from more than 40 repetitive tests at each crosshead speed, Weibull analysis suggests that the crazing-dominant toughness values showed a characteristic sharp PDF while that for shear yielding a relatively broad distribution. At the intermediate crosshead speed of 30mm/min, coexistence of both mechanisms was observed, and the unreliability of the toughness data were better fitted using two-group mixed Weibull distribution. The portion of each subpopulation in the two-group mixed Weibull distribution provided the statistical contribution from each mechanism to the deformation.

In order to further understand the involvement of crazing and shear yielding associated with the change of the loading rate, multi-stage tests were conducted. Two scenarios were considered to vary the type and extent of the pre-existing damage, by changing the order of the crosshead speeds applied to the specimen, with variation in the predetermined stroke value in the preloading stage. For each scenario and

predetermined stroke, at least 20 tests were carried out to examine the distribution characteristics. Weibull analysis indicated that by increasing the predetermined stroke, for scenario 1, i.e. preloading at 5mm/min then fracture at 60mm/min, the amount of crazing damage was increased accordingly. The test data indicate that the total energy remained constant and the 2nd stage toughness decreased continuously with the increase of the predetermined stroke. A sharp peak was observed to emerge in the PDF curve, suggesting that the portion of the corresponding subpopulation increases with the increase of the predetermined stroke, i.e. the increasing involvement of crazing. For scenario 2, when the crosshead speed of 60mm/min was applied first to introduce shear yielding, the total energy and the 2nd stage toughness do not show significant change with the increase of the predetermined stroke, with the mean values increasing slightly then decreasing. However, the increasing contribution of shear yielding can still be identified by Weibull analysis. To the point at which the predetermined stroke was increased to 6mm, the subpopulation representing crazing contributes to a very small portion of the 2nd stage toughness, which is not even detectable in the total energy. As a result, crazing is believed to be suppressed by the pre-existence of the shear yielding.

The study concludes that the two deformation mechanisms, crazing and shear yielding, have a major influence on the toughness of ABS, more importantly, on its distribution characteristics from their contribution. Their involvement in the deformation process can be adjusted by changing the test conditions, that is, crosshead speed in monotonic test and predetermined stroke in multi-stage tests. Weibull analysis is capable of characterizing data scattering in the evaluation of material toughness, and mixed Weibull distribution is useful to quantify the involvement of multiple mechanisms in the deformation of rubber-toughened polymers.

In the future study, optical or microscopic observation can be conducted to provide visual identification and confirm the involvement of each mechanism. The result is expected to give graphic evidence on individual specimens, however, it cannot provide quantitative information on the mechanism transition. It is well known that the deformation at high strain rate is an adiabatic process and energy will be

consumed for heating the material. When the glass transition temperature is approached, material properties, as well as the associated deformation mechanisms, are expected to change drastically. In our study, the loading rate applied is believed to be low enough to avoid significant heating. Therefore, the loading rate is deemed as the major parameter that affects the toughening mechanisms. When the high loading rate is applied, the temperature change and its influence on material properties and distribution characteristics can be an area that is worth exploration in the future study.

References

[1] J. N. Sultan, R. C. Liable, F. J. McGarry. Polym. Symp, 16, p. 127 (1971).

[2] J. N. Sultan, F. J. McGarry. “Effect of Rubber Particle-Size on Deformation Mechanisms in Glassy Epoxy”, Polymer Engineering and Science, Vol. 13, p. 29-34 (1973).

[3] A.C. Garg and Y. W. MAI, “Failure Mechanisms in Toughened Epoxy-Resins-a Review”, Composites Science and Technology, Vol. 31, p. 179-223 (1988).

[4] R. P. Kambour. “Optical Properties and Structure of Crazes in Transparent Glassy Polymers”, Nature, Vol. 195, p. 1299-1300 (1962).

[5] C. B. Bucknall and R. R. Smith. “Stress-Whitening in High-Impact Polystyrenes”, Polymer, Vol. 6, p. 437-446 (1965).

[6] R. P. Kambour, R. R. Russell. “Electron Microscopy of Crazes in Polystyrene and Rubber Modified Polystyrene-Use of Iodine-Sulphur Eutectic as a Craze Reinforcing Impregnant”, Polymer, Vol. 12, p. 237 (1971).

[7] C. B. Bucknall and D. Clayton. “Rubber-Toughening of Plastics. 1. Creep Mechanisms in HIPS”, Journal of Materials Science, Vol. 7, p. 202 (1972).

[8] C. B. Bucknall, D. Clayton and W. E. Keast. “Rubber-Toughening of Plastics. 2. Creep Mechanisms in HIPS/PPO Blends”, Journal of Materials Science, Vol. 7, p. 1443-1453 (1972).

[9] C. B. Bucknall, D. Clayton and W. E. Keast. “Rubber-Toughening of Plastics. 3. Strain Damage in HIPS and HIPS/PPO Blends”, Journal of Materials Science, Vol. 8, p. 514-524 (1973).

[10] C. B. Bucknall and I. C. Drinkwater. “Rubber-Toughening of Plastics. 4. Creep Mechanisms in ABS Emulsion Polymer”, Journal of Materials Science, Vol. 8, p. 1800-1808 (1973).

[11] A. M. Donald and E. J. Kramer. “Effect of Molecular Entanglements on Craze Microstructure in Glassy-Polymers”, Journal of Polymer Science Part B-Polymer Physics, Vol. 20, p. 899-909 (1982).

[12] G. H. Michler. “Mechanisms of Plastic-Deformation in Rubber-Modified High-Impact Polymers”, Acta Polymerica, Vol. 36, p. 285-293 (1985).

[13] A. C. M. Yang, E. J. Kramer, C. C. Kuo and S. L. Phoenix. “Craze Fibril Stability and Breakdown in Polystyrene”, Macromolecules, Vol. 19, p. 2010-2019 (1986).

[14] S. Newman and S. Strella. “Stress-Strain Behavior of Rubber-Reinforced Glassy Polymers”, Journal of Applied Polymer Science, Vol. 9, p. 2297-2310 (1965).

[15] S. Strella. “Rubber Reinforcement of Glassy Polymers”, Journal of Polymer Science Part A-2-Polymer Physics, Vol. 4, p. 527 (1966).

[16] S. Newman. “Fracture of Polymers and Polyblends”, Polymer-Plastics Technology and Engineering, Vol. 2, p. 67-88 (1973).

[17] H. Breuer, F. Haaf and J. Stabenow. “Stress Whitening and Yielding Mechanism of Rubber-Modified PVC”, Journal of Macromolecular Science-Physics, Vol. B14, p. 387-417 (1977).

[18] S. Wu. “Impact Fracture Mechanisms in Polymer Blends: Rubber-Toughened Nylon”, Journal of Polymer Science Part B: Polymer Physics, Vol. 21, p. 699-716 (1983).

[19] D. S. Parker, H. J. Sue, J. Huang and A. F. Yee. “Toughening Mechanisms in Core Shell Rubber Modified Polycarbonate”, Polymer, Vol. 31, p. 2267-2277 (1990).

[20] W. D. Bascom, R. E. Cottington, R. L. Jones and P. Peyser. “Fracture of Epoxy-Modified and Elastomer-Modified Epoxy Polymers in Bulk and as Adhesives”, Journal of Applied Polymer Science, Vol. 19, p. 2545-2562 (1975).

[21] A. M. Donald and E. J. Kramer. “Plastic-Deformation Mechanisms in Poly(Acrylonitrile-Butadiene Styrene) [ABS], Journal of Materials Science, Vol. 17, p. 1765-1772 (1982).

[22] A. F. Yee and R. A. Pearson. “Toughening Mechanisms in Elastomer-Modified Epoxies. 1. Mechanical Studies”, Journal of Material Science, Vol. 21, p. 2462-2474 (1986).

[23] R. A. Pearson and A. F. Yee. “Toughening Mechanisms in Elastomer-Modified Epoxies. 2. Microscopy Studies”, Journal of Material Science, Vol. 21, p. 2475-2488 (1986).

[24] R. A. Pearson and A. F. Pearson. “Toughening Mechanisms in Elastomer-Modified Epoxies. 3. The Effect of Cross-Link Density”, Journal of Materials Science, Vol. 24, p. 2571-2580 (1989).

[25] R. A. Pearson and A. F. Yee. “Influence of Particle-Size and Particle-Size Distribution on Toughening Mechanisms in Rubber-Modified Epoxies”, Journal of Material Science, Vol. 26, p. 3828-3844 (1991).

[26] R. A. Bubeck, D. J. Buckley, E. J. Kramer and H. Brown. “Modes of Deformation in Rubber-Modified Thermoplastics during Tensile Impact”, Journal of Material Science, Vol. 26, p. 6249-6259 (1991).

[27] E. H. Merz, G. C. Claver and M. Baer. “Studies on Heterogeneous Polymeric Systems”, Journal of Polymer Science, Vol. 22, p. 325-341 (1956).

[28] S. Kunz-Douglas, P. W. R. Beaumont and M. F. Ashby. “A Model for the Toughness of Epoxy-Rubber Particulate Composites”, Journal of Materials Science, Vol. 15, p. 1109-1123 (1980).

[29] C. G. Bragaw. “Theory of Rubber Toughening of Brittle Polymers”, Advances in Chemistry Series, Issue 99, p. 86 (1971).

[30] Bucknall, C. B. “Toughened Plastics”, Applied Science Publication, London (1977).

[31] G. H. Michler and C. B. Bucknall. “New Toughening Mechanisms in Rubber Modified Polymers”, Plastics Rubber and Composites, Vol. 30, p. 110 (2001).

[32] C. B. Bucknall. “Quantitative Approaches to Particle Cavitation, Shear Yielding, and Crazing in Rubber-Toughened Polymers”, Journal of Polymer Science Part B-Polymer Physics, Vol. 45, p. 1399-1409 (2007).

[33] K. Takahashi. “Rapid Healing of Crazes in Ruptured Rubber-Toughened Plastics”, Journal of Polymer Science Part B-Polymer Physics, Vol. 12, p. 1697-1705 (1974).

[34] C. Cheng, A. Hiltner, E. Baer, P. R. Soskey and S. G. Mylonakis. “Cooperative Cavitation in Rubber-Toughened Polycarbonate”, Journal of Materials Science, Vol. 30, p. 587-595 (1995).

[35] B. J. P. Jansen, S. Rastogi, H. E. H. Meijer and P. J. Lemstra. “Rubber-Modified Glassy Amorphous Polymers Prepared via Chemically Induced Phase Separation. 3. Influence of the Strain Rate on the Microscopic Deformation Mechanism”, Macromolecules, Vol. 32, p. 6283-6289 (1999).

[36] B. Z. Jang. “Rubber-Toughening in Polypropylene”, Journal of Applied Polymer Science, Vol. 30, p. 2485-2504 (1985).

[37] S. T. Wellinghoff and E. Baer. “Microstructure and its Relationship to Deformation Processes in Amorphous Polymer Glasses”, Journal of Applied Polymer Science, Vol. 22, p. 2025-2045 (1978).

[38] J. U. Starke, R. Godehardt, G. H. Michler and C. B. Bucknall. “Mechanisms of Cavitation over a Range of Temperatures in Rubber-Toughened PSAN Modified with Three-Stage Core-Shell Particles”, Journal of Materials Science, Vol. 32, p. 1855-1860 (1997).

[39] P. Y. B. Jar, R. Y. Wu, T. Kuboki, K. Takahashi and T. Shinmura. “Toughness of SMI-Modified ABS Alloys and the Associated Deformation Behavior”, Journal of Applied Polymer Science, Vol. 71, p. 1543-1553 (1999).

[40] B. J. P. Jansen, S. Rastogi, H. E. H. Meijer and P. J. Lemstra. “Rubber-Modified Glassy Amorphous Polymers Prepared via Chemically Induced Phase Separation. 2. Mode of Microscopic Deformation Studied by In-Situ Small-Angle X-Ray Scattering during Tensile Deformation”, Macromolecules, Vol. 34, p. 4007-4018 (2001).

[41] C. Zhou, X. Y. Bao, Z. Y. Tan, S. L. Sun, Y. H. Ao, H. D. Yang and H. X. Zhang. “Transition from Crazing to Shear Deformation in ABS/PVC Blends”, Journal of Polymer Science Part B-Polymer Physics, Vol. 44, p. 687-695 (2006).

[42] C. B. He, A. M. Donald and M. F. Butler. “In-Situ Deformation Studies of Rubber Toughened Poly(methyl methacrylate): Influence of Rubber Particle Concentration and Rubber Cross-Linking Density”, Macromolecules, Vol. 31, p. 158-164 (1998).

[43] B. J. Cardwell and A. F. Yee. “Rate and Temperature Effects on the Fracture-Toughness of a Rubber-Modified Epoxy”, Polymer, Vol. 34, p. 1695-1701 (1993).

[44] Y. Nanzai. “Plastic-Deformation Mechanism in PMMA under Creep Stress”, JSME International Journal Series A-Mechanics and Material Engineering, Vol. 37, p. 149-154 (1994).

[45] S. Barre, T. Chotard and M. L. Benzeggagh. “Comparative Study of Strain Rate Effects on Mechanical Properties of Glass Fibre-Reinforced Thermoset Matrix Composites”. Composites Part A-Applied Science and Manufacturing, Vol. 27, p. 1169-1181 (1996).

[46] K. Ravi-Chandar, J. Lu, B. Yang and Z. Zhu. “Failure Mode Transitions in Polymers under High Strain Rate Loading”, International Journal of Fracture, Vol. 101, p. 33-72 (2000).

[47] P. Compston, P. Y. B. Jar, P. J. Burchill and K. Takahashi. “The Effect of Matrix Toughness and Loading Rate on the mode-II Interlaminar Fracture Toughness of Glass-Fibre/Vinyl-Ester Composites”, Composites Science and Technology, Vol. 61, p. 321-333 (2001).

[48] C. L. Wu, M. Q. Zhang, M. Z. Rong and K. Friedrich. “Tensile Performance Improvement of Low Nanoparticles Filled-Polypropylene Composites”, Composites Science and Technology, Vol. 62, p. 1327-1340 (2002).

[49] G. C. Jacob, J. M. Starbuck, J. F. Fellers, S. Simunovic and R. G. Boeman. “The Effect of Loading Rate on the Fracture Toughness of Fiber Reinforced Polymer Composites”, Journal of Applied Polymer Science, Vol. 96, p. 899-904 (2005).

[50] S. D. Park, M. Todo, K. Arakawa and M. Koganemaru. “Effect of Crystallinity and Loading-Rate on Mode I Fracture Behavior of Poly(lactic acid)”, Polymer, Vol. 47, p. 1357-1363 (2006).

[51] J. Liu, H. J. Sue, Z. J. Thompson, F. S. Bates, M. Dettloff, G. Jacob, N. Verghese and H. Pham. “Strain Rate Effect on Toughening of Nano-Sized PEP-PEO Block Copolymer Modified Epoxy”, Acta Materialia, Vol. 57, p. 2691-2701 (2009).

[52] J. Milios, G. C. Papanicolaou and R. J. Young. “The Effect of Loading Rate and Crack-Tip Blunting on Crack-Propagation in Rubber-Toughened PMMA”, Plastics and Rubber Processing and Applications, Vol. 11, p. 37-43 (1989).

[53] P. Beguelin and H. H. Kausch. “Loading Rate Dependence of the Deformation and Fracture Mechanisms in Impact Modified Poly(methyl methacrylate)”, Journal de Physique IV, Vol. 7, p. 933-938 (1997).

[54] D. Raghavan, J. He, D. Hunston and D. Hoffman. “Strain Rate Dependence of Fracture in a Rubber-Toughened Epoxy System”, Journal of Adhesion, Vol. 78, p. 723-739 (2002).

[55] J. G. Williams, J. M. Hodgkinson. “Crack-Blunting Mechanisms in Impact Tests on Polymers”, Proceedings of the Royal Society of London Series A-Mathematical Physical and Engineering Sciences, Vol. 375, p. 231-247 (1981).

[56] T. Vukhanh and Z. Yu. “Mechanisms of Brittle-Ductile Transition in Toughened Thermoplastics”, Theoretical and Applied Fracture Mechanisms, Vol. 26, p. 177-183 (1997).

[57] T. Vu-Khanh. “Time-Temperature Dependence in Fracture Behavior of High Impact Polystyrene”, Theoretical and Applied Fracture Mechanics, Vol. 29, p. 75-83 (1998).

[58] J. P. F. Inberg, A. Takens and R. J. Gaymans. “Strain Rate Effects in Polycarbonate and Polycarbonate/ABS Blends”, Polymer, Vol. 43, p. 2795-2802 (2002).

[59] L. A. Utracki, “Polymer Blends Handbook”, Dordrecht, Boston, Kluwer Academic Publishers (2002).

[60] A. C. Steenbrink, H. Janik and R. J. Gaymans. “Deformation and Fracture of Styrene-Acrylonitrile Copolymer-Rubber Blends-Microscopy Studies of Deformation Zones”, Journal of Materials Science, Vol. 32, p. 5505-5511 (1997).

[61] C. B. Bucknall. “Applications of Microscopy to the Deformation and Fracture of Rubber-Toughened Polymers”, Journal of Microscopy-Oxford, Vol. 201, p. 221-229 (2001).

[62] T. K. Chen and Y. H. Jan. “Effect of Rubber Matrix Interfacial Modifications on the Properties of a Rubber-Toughened Epoxy-Resin”, Polymer Engineering and Science, Vol. 31, p. 577-585 (1991).

[63] E. J. Moskala. “Fracture-Behavior of Rubber-Toughened Polymer Blends”, Journal of Materials Science, Vol. 27, p. 4883-4889 (1992).

[64] J. Jancar, A. Dianselmo, A. T. Dibenedetto and J. Kucera. “Failure Mechanisms in Elastomer Toughened Polypropylene”, Polymer, Vol. 34, p. 1684-1694 (1993).

[65] C. R. Bernal, P. M. Frontini, M. Sforza and M. A. Bibbo. “Microstructure, Deformation, and Fracture-Behavior of Commercial ABS Resins”, Journal of Applied Polymer Science, Vol. 58, p. 1-10 (1995).

[66] S. A. Xu, M. Jiang and J. S. Shen. “Morphology and Deformation Mechanisms of Polystyrene Low-Density Polyethylene Blends Studied by TEM”, Polymer Journal, Vol. 27, p. 607-613 (1995).

[67] M. Schneider, T. Pith and M Lambla. “Toughening of Polystyrene by Natural Rubber-Based Composite Particles. 1. Impact Reinforcement by PMMA and PS Grafted Core-Shell Particles”, Journal of Materials Science, Vol. 32, p. 6331-6342 (1997).

[68] J. Takahashi, H. Watanabe and J. Nakamot. “Failing Weight Impact Strength and Transparency of Rubber-Modified Methylmethacrylate-Butadiene-Styrene Resin/Emulsion Graft Polymer Blends”, Kobunshi Ronbunshu, Vol. 61, p. 114-121 (2004).

[69] R. Lach, R. Adhikari, R. Weidisch, T. A. Huy, G. H. Michler, W. Grellmann and K. Knoll. “Crack Toughness Behavior of Binary Poly(styrene-butadiene) Block Copolymer Blends”, Journal of Materials Science, Vol. 39, p. 1283-1295 (2004).

[70] J. H. Lin and A. C. M. Yang. “Crazing Micromechanism in Glassy Atactic Polystyrene and its Blends with Poly(2, 6-dimethyl-1, 4-diphenyl oxides) by AFM”, Macromolecules, Vol. 34, p. 3698-3705 (2001).

[71] K. Porfyrakis, H. E. Assender and I. M. Robinson. “The Interrelationship Between Processing Conditions, Microstructure and Mechanical Properties for Injection Moulded Rubber-Toughened Poly(methyl methacrylate) (RTPMMA) Samples”, Polymer, Vol. 43, p. 4769-4781 (2002).

[72] C. Marieta, P. M. Remiro, G. Garmendia, I. Harismendy and I. Mondragon. “AFM Approach toward Understanding Morphologies in Toughened Thermosetting Matrices”, European Polymer Journal, Vol. 39, p. 1965-1973 (2003).

[73] H. R. Brown and E. J. Kramer. “Craze Microstructure from Small-Angle X-Ray-Scattering (SAXS)”, Journal of Macromolecular Science-Physics, Vol. B19, p. 487-522 (1981).

[74] Y. Ijichi, T. Kojima, Y. Suzuki, T. Nishio, M. Kakugo and Y. Amemiya. “Synchrotron Radiation Small-Angle X-ray-Scattering Study on the Deformation Mechanisms of a Toughened Nylon-6 Poly(phenylene ether) Blend and High-Impact polystyrene”, Macromolecules, Vol. 26, p. 829-835 (1993).

[75] A. M. L. Magalhaes and R. J. M. Borggreve. “Contribution of the Crazing Process to the Toughness of Rubber-Modified Polystyrene”, Macromolecules, Vol. 28, p. 5841-5851 (1995).

[76] C. He and A. M. Donald. “Morphology of a Deformed Rubber Toughened Poly(methyl methacrylate) Film under Tensile Strain”, Journal of Materials Science, Vol. 32, p. 5661-5667 (1997).

[77] C. B. He, A. M. Donald, M. F. Butler and O. Diat. “Small Angle X-ray Scattering Analysis of Crazing in Rubber Toughened Polymers: Influence of Particle Deformation”, Polymer, Vol. 39, p. 659-667 (1998).

[78] M. Sferrazza, J. Crawshaw, A. M. Donald and T. Narayanan. “Evidence of Highly Localized Failure within Core-Shell Toughening Particles from In-Situ Small-Angle Scattering”, Macromolecules, Vol. 34, p. 6708-6718 (2001).

[79] P. Y. B. Jar, D. C. Creagh, K. Konishi and T. Shinmura. “Mechanical Properties and Deformation Mechanisms in High Thermal Resistant Poly(acrylonitrile-butadiene-styrene) under Static Tension and Izod impact”, Journal of Applied Polymer Science, Vol. 85, p. 17-24 (2002).

[80] P. Y. B. Jar, R. Lee, D. C. Creagh, K. Konishi and T. Shinmura. “Identification of Deformation Behavior in High-Thermal-Resistant Poly(acrylonitrile-butadiene-styrene) (ABS)”, Journal of Applied Polymer Science, Vol. 81, p. 1316-1321 (2001).

[81] C. B. Bucknall and D. Clayton. “Dilatometric Studies of Crazing in Rubber-Toughened Plastics”, Nature-Physical Science, Vol. 231, p. 107 (1971).

[82] M. A. Maxwell and A. F. Yee. “The Effect of Strain Rate on the Toughening Mechanisms of Rubber-Modified Plastics”, Polymer Engineering and Science, Vol. 21, p. 205-211 (1981).

[83] S. I. Naqui and I. M. Robinson. “Tensile Dilatometric Studies of Deformation in Polymeric Materials and Their Composites”, Journal of Materials Science, Vol. 28, p. 1421-1429 (1993).

[84] P. Francois, J. M. Gloaguen, B. Hue and J. M. Lefebvre. “Volume Strain-Measurements by Optical Extensometry-Application to the Tensile Behavior of RT-PMMA”, Journal de Physique III, Vol. 4, p. 321-329 (1994).

[85] S. V. Nair, S. C. Wong and L. A. Goettler. “Fracture Resistance of Polyblends and Polyblend Matrix Composites. 1. Unreinforced and Fibre-Reinforced Nylon 6, 6/ABS Polyblends”, Journal of Materials Science, Vol. 32, p. 5335-5346 (1997).

[86] S. A. Xu and S. C. Tjong. “Deformation Mechanisms and Fracture Toughness of Polystyrene/High-Density Polyethylene Blends Compatibilized by Triblock Copolymer”, Journal of Applied Polymer Science, Vol. 77, p. 2024-2033 (2000).

[87] R. Schirrer, R. Lenke and J. Boudouaz. “Study of Mechanical Damage in Rubber-Toughened Poly(methyl methacrylate) by Single and Multiple Scattering of Light”, Polymer Engineering and Science, Vol. 37, p. 1748-1760 (1997).

[88] S. Gehant and R. Schirrer. “Multiple Light Scattering and Cavitation in Two Phase Tough Polymers”, Journal of Polymer Science Part B-Polyer Physics, Vol. 37, p. 113-126 (1999).

[89] Robert Abernethy. “The New Weibull Handbook”, Fifth Edition, North Palm Beach, Fla (2006).

[90] L. G. Johnson. “The Median Ranks of Sample Values in their Population with an Application to Certain Fatigue Studies”, Bulletin of the American Mathematical Society, Vol. 56, p. 247 (1950).

[91] S. H. Zanakis. “A Simulation Study of Some Simple Estimators for the Three-Parameter Weibull Distribution”, Journal of Statistical Computation and Simulation, Vol. 9, p. 101-116 (1979).

[92] J. E. Shigley and C. R. Mischke. “Mechanical Engineering Design”, Fifth Edtion, McGraw-Hill Inc., New York (1989).

[93] http://www.weibull.com/LifeDataWeb/lifedataweb.htm, ReliaSoft Corporation, June 11, 2009.

[94] J. A. Nelder, R. Mead. “A Simplex-Method for Function Minimization”, Computer Journal, Vol. 7, p. 308-313 (1965).

[95] “Characteristics of the Weibull Distribution”, http://www.weibull.com/hotwire/issue14/relbasics14.htm, ReliaSoft Corporation, June 11, 2009.

[96] “Mixed Weibull Parameter Estimation”, http://www.weibull.com/LifeDataWeb/the_mixed_weibull_distribution.htm#parameters, ReliaSoft Corporation, June 11, 2009.

[97] J. J. More, “The Levenberg-Marquardt Algorithm: Implementation and Theory,” in Numerical Analysis, G. A. Watson, Ed. Berlin, Germany: Springer-Verlag, Vol. 630, Lecture Notes Math., p. 105-116 (1977).

[98] “Acrylonitrile butadiene styrene-Monomers in ABS poymer”, http://en.wikipedia.org/wiki/Acrylonitrile_butadiene_styrene, Wikipedia, The Free Encyclopedia, June 12, 2009.

[99] “More about Performance Plastics”, http://www.mcmaster.com/#8747kac, McMaster-Carr, June 12, 2009.

[100] H. W. Haslach Jr and R. W. Armstrong. “Deformable Bodies and their Material Behavior”, John Wiley & Sons, Inc., U.S.A. (2003).

Appendix 1 Derivation of Weibull Mean and Variance

It is well known for a discrete uniform distribution with the sample size of N, the expected value or the arithmetic mean and the sample variance can be defined by the equations [92]

$$\overline{x} = \frac{x_1 + x_2 + x_2 + \cdots + x_N}{N} = \frac{1}{N}\sum_{i=1}^{N} x_i \tag{A1-1}$$

$$s^2 = \frac{\left(x_1 - \overline{x}\right)^2 + \left(x_2 - \overline{x}\right)^2 + \left(x_3 - \overline{x}\right)^2 + \cdots + \left(x_N - \overline{x}\right)^2}{N} = \frac{1}{N}\sum_{1}^{N}\left(x_i - \overline{x}\right)^2 = \frac{1}{N}\sum_{1}^{N} x_i{}^2 - \overline{x}^2 \tag{A1-2}$$

For a discrete probability distribution, if there is a weight of percentage or probability f_i specified for each x_i, the weighted mean and variance can be expressed with the satisfaction of $\sum_{i=1}^{N} f_i = 1$, namely

$$\overline{x} = f_1 x_1 + f_2 x_2 + f_3 x_2 + \cdots + f_N x_N = \sum_{i=1}^{N} f_i x_i \tag{A1-3}$$

$$s^2 = f_1\left(x_1 - \overline{x}\right)^2 + f_2\left(x_2 - \overline{x}\right)^2 + f_3\left(x_3 - \overline{x}\right)^2 + \cdots + f_N\left(x_N - \overline{x}\right)^2 = \sum_{i=1}^{N} f_i\left(x_i - \overline{x}\right)^2 = \sum_{i=1}^{N} f_i x_i{}^2 - \overline{x}^2 \tag{A1-4}$$

Generalized from the above, the mean and variance of a continuous distribution of a positive variable can be formulated as

$$\mu = \int_0^\infty t f\left(t\right) dt \tag{A1-5}$$

$$Var = \int_0^\infty t^2 f\left(t\right) dt - \mu^2 \tag{A1-6}$$

where $f\left(t\right)$ is the probability density function of the continuous distribution.

Based on the above understanding, the Weibull mean and variance can be derived based on the concept of the r th moment of a distribution [89].

The r th moment of the distribution about the origin is defined by the following integral

$$\mu_r = \int_0^\infty t^r f(t)\,dt \tag{A1-7}$$

Obviously, the case of $r = 1$ represents the mean of the distribution, namely

$$\mu = \mu_1$$

And the calculation of the variance contains both 1st and 2nd moments of the distribution

$$Var = \mu_2 - \mu_1^2$$

In general, for the two-parameter Weibull distribution, by substituting the corresponding probability density function in the r th moment we have

$$\mu_r = \int_0^\infty t^r \left(\frac{\beta}{\eta}\right)\left(\frac{t}{\eta}\right)^{\beta-1} \exp\left[-\left(\frac{t}{\eta}\right)^\beta\right] dt$$

$$= \frac{\beta}{\eta^\beta}\int_0^\infty t^{r+\beta-1} \exp\left[-\left(\frac{t}{\eta}\right)^\beta\right] dt$$

Let $y = \left(\frac{t}{\eta}\right)^\beta$ and $dy = \frac{\beta}{\eta^\beta} t^{\beta-1} dt$, we have

$$t = \eta y^{1/\beta} \qquad \text{and} \qquad dt = \frac{\eta^\beta}{\beta t^{\beta-1}} dy = \frac{\eta^\beta}{\beta\left(\eta y^{1/\beta}\right)^{\beta-1}} dy$$

Substituting t with y yields

$$\mu_r = \frac{\beta}{\eta^\beta}\int_0^\infty \left(\eta y^{1/\beta}\right)^{r+\beta-1} \exp\left[-\left(\frac{\eta y^{1/\beta}}{\eta}\right)^\beta\right] \frac{\eta^\beta}{\beta\left(\eta y^{1/\beta}\right)^{\beta-1}} dy$$

$$= \eta^r \int_0^\infty y^{\frac{r}{\beta}} \exp(-y)\,dy$$

Noticing the integration can be expressed by a Gamma function (see Eqn. (2-8)), we have

$$\mu_r = \eta^r \Gamma\left(1 + \frac{r}{\beta}\right) \tag{A1-8}$$

Therefore, for the two-parameter Weibull distribution, the Weibull mean and variance can be calculated as

$$\mu = \mu_1 = \eta\Gamma\left(1+\frac{1}{\beta}\right) \tag{A1-9}$$

$$Var = \mu_2 - \mu_1^{\,2} = \eta^2\Gamma\left(1+\frac{2}{\beta}\right) - \left[\eta\Gamma\left(1+\frac{1}{\beta}\right)\right]^2 = \eta^2\left[\Gamma\left(1+\frac{2}{\beta}\right) - \Gamma^2\left(1+\frac{1}{\beta}\right)\right] \tag{A1-10}$$

And for the continuous distribution of Weibull, the condition $\int_0^\infty f(t)\,dt = 1$ can be easily verified

$$\int_0^\infty f(t)\,dt = F(\infty) - F(0) = \left[1-\exp(-\infty)\right] - \left[1-\exp(0)\right] = 1.$$

Appendix 2 Monotonic Test Results

The test data were subjected to processing based on the mean value and standard deviation. A range with a lower bound of average minus two times deviation and a higher bound of average plus two times deviation was determined. The test data that fall in the range were considered reasonable and retained. The data out of this range were eliminated for being considered as affected by defects. The data presented here are after this processing.

Table A2.1 Ultimate tensile strength at 5mm/min

failure order	ultimate strength (MPa)	failure order	ultimate strength (MPa)	failure order	ultimate strength (MPa)
1	36.2643	17	36.5369	33	36.8479
2	36.3142	18	36.5633	34	36.8507
3	36.3588	19	36.5972	35	36.8665
4	36.3804	20	36.64	36	36.8825
5	36.3881	21	36.6471	37	36.8941
6	36.3942	22	36.6518	38	36.9603
7	36.3965	23	36.6606	39	36.9617
8	36.4187	24	36.6799	40	36.9651
9	36.4264	25	36.7087	41	36.9681
10	36.4456	26	36.7177	42	37.008
11	36.4538	27	36.7413	43	37.0323
12	36.4604	28	36.8122	44	37.0336
13	36.4951	29	36.8152	45	37.0502
14	36.4985	30	36.8195	46	37.0744
15	36.5106	31	36.838	47	37.1493
16	36.5158	32	36.8453	48	37.1823

Table A2.2 Extension at break at 5mm/min

failure order	extension at break (mm)	failure order	extension at break (mm)	failure order	extension at break (mm)
1	5.93097	15	10.4634	29	14.2403
2	6.59109	16	10.7091	30	14.3528
3	6.64756	17	10.9477	31	14.4287
4	6.73394	18	11.1308	32	14.4301
5	7.22538	19	11.2225	33	14.7548
6	8.13065	20	11.4051	34	14.8135
7	8.28179	21	11.4433	35	15.2141
8	9.27965	22	11.9352	36	15.3506
9	9.36899	23	12.0554	37	15.3868
10	9.66293	24	12.3566	38	15.4133
11	10.1011	25	12.834	39	15.4199
12	10.1309	26	13.0265	40	15.4715
13	10.2663	27	13.1336	41	15.8972
14	10.298	28	13.7872	42	16.0082

Table A2.3 Toughness at 5mm/min

failure order	toughness (J)	failure order	toughness (J)	failure order	toughness (J)
1	6.5982	15	12.178	29	16.303
2	7.2749	16	12.318	30	16.456
3	7.2918	17	12.623	31	16.798
4	7.3239	18	13.158	32	16.893
5	7.8194	19	13.299	33	17.022
6	9.2191	20	13.434	34	17.217
7	9.3356	21	13.473	35	17.293
8	10.593	22	13.515	36	17.946
9	10.716	23	14.236	37	18.061
10	10.987	24	14.393	38	18.302
11	11.689	25	15.09	39	18.351
12	11.705	26	15.232	40	18.571
13	11.906	27	15.452	41	18.591
14	11.94	28	16.183	42	18.804

Table A2.4 Ultimate tensile strength at 30mm/min

failure order	ultimate strength (MPa)	failure order	ultimate strength (MPa)	failure order	ultimate strength (MPa)
1	38.6204	17	39.0407	33	39.3754
2	38.7036	18	39.0937	34	39.3856
3	38.7116	19	39.1133	35	39.4305
4	38.736	20	39.1307	36	39.4524
5	38.7404	21	39.1646	37	39.4594
6	38.8128	22	39.1669	38	39.4825
7	38.8144	23	39.1966	39	39.4912
8	38.8294	24	39.2398	40	39.5116
9	38.837	25	39.2488	41	39.5128
10	38.8418	26	39.2943	42	39.5912
11	38.854	27	39.3116	43	39.6001
12	38.9073	28	39.3172	44	39.6039
13	38.9213	29	39.3399	45	39.6083
14	38.9322	30	39.3465	46	39.6116
15	38.9659	31	39.3665	47	39.7319
16	39.0292	32	39.3754	48	39.7413

Table A2.5 Extension at break at 30mm/min

failure order	extension at break (mm)	failure order	extension at break (mm)	failure order	extension at break (mm)
1	3.566156	16	14.00889	31	17.79727
2	4.374799	17	14.80712	32	19.42128
3	5.135317	18	14.85395	33	20.19232
4	6.652604	19	15.04722	34	20.20932
5	6.766976	20	15.26609	35	20.40141
6	7.502906	21	15.55825	36	23.75348
7	7.901703	22	15.60379	37	23.80051
8	8.287311	23	15.83693	38	24.1665
9	9.446812	24	16.21384	39	24.37481
10	9.568541	25	16.42909	40	25.56533
11	10.26565	26	16.51426	41	28.53137
12	10.92506	27	16.57435	42	29.65664
13	11.85891	28	16.80078	43	30.03277
14	13.62051	29	17.60049	44	31.7165
15	13.68914	30	17.70278	45	32.06041

Table A2.6 Toughness at 30mm/min

failure order	toughness (J)	failure order	toughness (J)	failure order	toughness (J)
1	3.7113	16	16.589	31	21.045
2	4.672	17	17.549	32	23.42
3	5.6069	18	17.557	33	23.843
4	7.3872	19	17.679	34	24.672
5	7.7274	20	17.766	35	24.769
6	8.5927	21	18.451	36	28.974
7	9.4166	22	19.14	37	29.168
8	9.5257	23	19.158	38	29.335
9	11.153	24	19.712	39	30.127
10	11.329	25	19.837	40	30.592
11	12.377	26	19.86	41	34.428
12	13.136	27	19.925	42	35.815
13	14.183	28	20.227	43	36.756
14	16.433	29	20.945	44	39.043
15	16.451	30	21.005	45	39.135

Table A2.7 Ultimate tensile strength at 60mm/min

failure order	ultimate strength (MPa)	failure order	ultimate strength (MPa)	failure order	ultimate strength (MPa)
1	39.6985	17	40.1447	33	40.267
2	39.7099	18	40.1529	34	40.2737
3	39.8263	19	40.1541	35	40.2792
4	39.8776	20	40.1633	36	40.2819
5	39.883	21	40.1808	37	40.2887
6	39.9059	22	40.1884	38	40.3148
7	39.9194	23	40.189	39	40.3359
8	39.9272	24	40.1898	40	40.3394
9	39.9292	25	40.225	41	40.3671
10	39.9936	26	40.2363	42	40.424
11	40.0298	27	40.2365	43	40.4311
12	40.0929	28	40.2385	44	40.4635
13	40.1075	29	40.2508	45	40.4701
14	40.1195	30	40.2561	46	40.5017
15	40.1206	31	40.2569	47	40.5234
16	40.1294	32	40.2656		

Table A2.8 Extension at break at 60mm/min

failure order	extension at break (mm)	failure order	extension at break (mm)	failure order	extension at break (mm)
1	4.67564	18	19.5133	35	28.2602
2	5.52413	19	19.5806	36	28.476
3	8.73402	20	20.0554	37	28.4865
4	8.79665	21	20.1165	38	28.5696
5	9.58697	22	20.2991	39	29.4841
6	10.6381	23	21.1272	40	30.0211
7	11.1604	24	21.2784	41	30.0408
8	11.4852	25	21.5768	42	31.9061
9	12.9608	26	22.3142	43	32.8713
10	13.4181	27	22.8709	44	33.8656
11	14.0248	28	23.762	45	34.361
12	15.6411	29	24.1994	46	34.66566
13	16.2346	30	24.64	47	39.81953
14	19.0358	31	25.5956	48	41.54877
15	19.0912	32	25.813	49	41.69999
16	19.1555	33	26.8109	50	42.6171
17	19.4563	34	27.0813		

Table A2.9 Toughness at 60mm/min

failure order	toughness (J)	failure order	toughness (J)	failure order	toughness (J)
1	5.2635	18	24.194	35	34.793
2	6.4165	19	24.371	36	34.796
3	10.468	20	24.52	37	34.813
4	10.613	21	25.19	38	35.368
5	11.68	22	25.437	39	35.676
6	12.913	23	25.852	40	36.7
7	13.762	24	26.208	41	36.938
8	14.16	25	26.649	42	39.213
9	15.535	26	27.565	43	40.428
10	16.323	27	28.162	44	42.435
11	17.068	28	29.733	45	42.727
12	18.998	29	29.863	46	43.197
13	19.715	30	30.775	47	48.017
14	23.507	31	31.034	48	50.628
15	23.51	32	31.642	49	51.026
16	23.781	33	31.736	50	51.639
17	23.829	34	32.792		

Appendix 3 Multi-stage Test Results

The test data of multi-stage tests are subjected to the same processing as in the monotonic tests. For each scenario and each predetermined stroke, mechanical properties of total elongation, total energy, second stage elongation and second stage toughness are determined. For the first scenario, the maximum strength in the second stage is also presented.

Table A3.1 Second stage maximum strength for scenario 1 and the predetermined stroke of 2.563mm

failure order	2nd stage maximum strength (MPa)	failure order	2nd stage maximum strength (MPa)	failure order	2nd stage maximum strength (MPa)
1	35.7185	10	35.9042	19	36.0719
2	35.7535	11	35.9245	20	36.1073
3	35.7735	12	35.9256	21	36.126
4	35.8062	13	35.936	22	36.1265
5	35.8139	14	35.9555	23	36.1387
6	35.8362	15	35.9754	24	36.18
7	35.8399	16	36.0094	25	36.1937
8	35.8675	17	36.0157	26	36.2998
9	35.8683	18	36.042		

Table A3.2 Total elongation for scenario 1 and the predetermined stroke of 2.563mm

failure order	total elongation (mm)	failure order	total elongation (mm)	failure order	total elongation (mm)
1	5.531637	10	11.02245	19	13.78502
2	6.465037	11	11.06517	20	14.91458
3	6.787982	12	11.19905	21	15.30853
4	7.346274	13	11.4694	22	15.37265
5	8.362756	14	12.28441	23	15.64961
6	9.968201	15	12.48512	24	16.40117
7	10.78397	16	12.68827	25	19.13147
8	10.82672	17	12.89959		
9	10.87293	18	13.38374		

Table A3.3 Total energy for scenario 1 and the predetermined stroke of 2.563mm

failure order	total energy (J)	failure order	total energy (J)	failure order	total energy (J)
1	6.6444	10	13.877	19	17.785
2	7.8784	11	14.122	20	19.145
3	8.4487	12	14.146	21	19.773
4	9.0921	13	14.602	22	19.783
5	10.509	14	15.874	23	19.84
6	12.7	15	15.976	24	21.358
7	13.523	16	16.267	25	24.449
8	13.699	17	16.577		
9	13.73	18	16.947		

Table A3.4 Second stage elongation for scenario 1 and the predetermined stroke of 2.563mm

failure order	2nd stage elongation (mm)	failure order	2nd stage elongation (mm)	failure order	2nd stage elongation (mm)
1	5.021272	10	10.52495	19	13.27506
2	5.991291	11	10.56369	20	14.45303
3	6.289451	12	10.70568	21	14.82177
4	6.857181	13	10.95566	22	14.88128
5	7.881111	14	11.81529	23	15.15126
6	9.536123	15	11.94423	24	15.90521
7	10.27576	16	12.17441	25	18.67028
8	10.34095	17	12.38856		
9	10.37331	18	12.86573		

Table A3.5 Second stage toughness for scenario 1 and the predetermined stroke of 2.563mm

failure order	2nd stage toughness (J)	failure order	2nd stage toughness (J)	failure order	2nd stage toughness (J)
1	5.6618	10	12.9078	19	16.7813
2	6.9707	11	13.1371	20	18.226
3	7.4359	12	13.1737	21	18.8108
4	8.13814	13	13.60628	22	18.81093
5	9.5613	14	14.9569	23	18.87363
6	11.8444	15	14.9733	24	20.3728
7	12.5903	16	15.2695	25	23.516
8	12.6975	17	15.5703		
9	12.7726	18	15.9321		

Table A3.6 Second stage maximum strength for scenario 1 and the predetermined stroke of 3.129mm

failure order	2nd stage maximum strength (MPa)	failure order	2nd stage maximum strength (MPa)	failure order	2nd stage maximum strength (MPa)
1	35.0434	10	35.1812	19	35.3234
2	35.0547	11	35.2	20	35.3437
3	35.0594	12	35.2083	21	35.3537
4	35.0678	13	35.2093	22	35.3658
5	35.1102	14	35.2236	23	35.4039
6	35.1284	15	35.258	24	35.4364
7	35.1405	16	35.2837	25	35.4663
8	35.173	17	35.2879		
9	35.1791	18	35.3192		

Table A3.7 Total elongation for scenario 1 and the predetermined stroke of 3.129mm

failure order	total elongation (mm)	failure order	total elongation (mm)	failure order	total elongation (mm)
1	6.050342	10	10.79564	19	14.46915
2	7.016129	11	11.08013	20	14.61561
3	8.774771	12	11.1465	21	14.74689
4	9.31294	13	11.62757	22	14.84583
5	9.463529	14	11.62885	23	14.94671
6	9.722652	15	11.64965	24	17.39906
7	10.11134	16	12.27336	25	18.01389
8	10.11957	17	12.76496		
9	10.37969	18	13.10906		

Table A3.8 Total energy for scenario 1 and the predetermined stroke of 3.129mm

failure order	total energy (J)	failure order	total energy (J)	failure order	total energy (J)
1	7.4722	10	13.232	19	18.264
2	8.4486	11	14.058	20	18.555
3	10.721	12	14.076	21	18.724
4	11.566	13	14.273	22	18.97
5	11.58	14	14.875	23	19.324
6	11.762	15	14.934	24	22.159
7	12.468	16	16.101	25	22.797
8	13.093	17	16.238		
9	13.227	18	16.871		

Table 3.9 Second stage elongation for scenario 1 and the predetermined stroke of 3.129mm

failure order	2nd stage elongation (mm)	failure order	2nd stage elongation (mm)	failure order	2nd stage elongation (mm)
1	5.070172	10	9.828942	19	13.50245
2	6.049429	11	10.1041	20	13.65068
3	7.80556	12	10.17535	21	13.77714
4	8.328304	13	10.64351	22	13.87913
5	8.496829	14	10.66215	23	13.98075
6	8.755952	15	10.69131	24	16.43236
7	9.15287	16	11.30828	25	17.04719
8	9.154778	17	11.80556		
9	9.393514	18	12.1658		

Table A3.10 Second stage toughness for scenario 1 and the predetermined stroke of 3.129mm

failure order	2nd stage toughness (J)	failure order	2nd stage toughness (J)	failure order	2nd stage toughness (J)
1	5.657	10	11.4426	19	16.4796
2	6.6642	11	12.2916	20	16.7706
3	9.0098	12	12.3147	21	16.9615
4	9.7956	13	12.4886	22	17.1669
5	9.8345	14	13.1123	23	17.5515
6	9.9776	15	13.1163	24	20.3746
7	10.6836	16	14.2785	25	21.0126
8	11.2795	17	14.4824		
9	11.4399	18	15.1235		

Table A3.11 Second stage maximum strength for scenario 1 and the predetermined stroke of 6mm

failure order	2nd stage maximum strength (MPa)	failure order	2nd stage maximum strength (MPa)	failure order	2nd stage maximum strength (MPa)
1	34.2221	11	34.406	21	34.53
2	34.2223	12	34.4127	22	34.5406
3	34.304	13	34.4358	23	34.5685
4	34.3145	14	34.4416	24	34.5894
5	34.324	15	34.4485	25	34.591
6	34.3512	16	34.4875	26	34.6051
7	34.3562	17	34.5009	27	34.6223
8	34.3614	18	34.5082	28	34.623
9	34.365	19	34.511	29	34.6251
10	34.3773	20	34.5182	30	34.6342

Table A3.12 Total elongation for scenario 1 and the predetermined stroke of 6mm

failure order	total elongation (mm)	failure order	total elongation (mm)	failure order	total elongation (mm)
1	6.690795	10	10.21633	19	12.83628
2	8.926355	11	10.46625	20	13.4129
3	9.062793	12	10.69111	21	13.70593
4	9.251951	13	10.70906	22	14.51928
5	9.817981	14	10.99739	23	14.65541
6	9.989012	15	11.6602	24	16.38213
7	10.15139	16	11.98683	25	16.83725
8	10.17606	17	12.3624		
9	10.1823	18	12.79815		

Table A3.13 Total energy for scenario 1 and the predetermined stroke of 6mm

failure order	total energy (J)	failure order	total energy (J)	failure order	total energy (J)
1	8.106	10	13.206	19	16.693
2	11.287	11	13.319	20	17.148
3	11.381	12	13.33	21	17.262
4	11.464	13	13.56	22	18.809
5	12.36	14	14.093	23	19.067
6	12.526	15	15.392	24	21.133
7	12.811	16	15.57	25	22.08
8	12.97	17	16.019		
9	13.032	18	16.07		

Table A3.14 Second stage elongation for scenario 1 and the predetermined stroke of 6mm

failure order	2nd stage elongation (mm)	failure order	2nd stage elongation (mm)	failure order	2nd stage elongation (mm)
1	3.57636	10	7.075776	19	9.703359
2	5.826311	11	7.3526	20	10.28882
3	5.905658	12	7.514675	21	10.5673
4	6.151213	13	7.594045	22	11.42085
5	6.660487	14	7.87424	23	11.54515
6	6.883718	15	8.572904	24	13.26913
7	7.048734	16	8.845878	25	13.73286
8	7.06546	17	9.268672		
9	7.073437	18	9.626355		

Table A3.15 Second stage toughness for scenario 1 and the predetermined stroke of 6mm

failure order	2nd stage toughness (J)	failure order	2nd stage toughness (J)	failure order	2nd stage toughness (J)
1	2.8736	10	7.8856	19	11.3448
2	6.0154	11	8.0632	20	11.9892
3	6.1807	12	8.0723	21	12.0443
4	6.272	13	8.3888	22	13.5193
5	7.1126	14	8.8089	23	13.7719
6	7.455	15	10.0815	24	15.8833
7	7.6119	16	10.1397	25	16.7346
8	7.6433	17	10.7547		
9	7.7248	18	10.8488		

Table A3.16 Total elongation for scenario 2 and the predetermined stroke of 2.998mm

failure order	total elongation (mm)	failure order	total elongation (mm)	failure order	total elongation (mm)
1	9.943757	9	13.84606	17	21.26836
2	10.98492	10	15.97827	18	21.65437
3	11.36583	11	16.21851	19	23.41202
4	11.78402	12	16.44245	20	24.17927
5	12.57585	13	16.63897	21	25.03148
6	12.76981	14	16.95782	22	25.19191
7	12.83753	15	16.96632		
8	13.01892	16	20.46207		

Table A3.17 Total energy for scenario 2 and the predetermined stroke of 2.998mm

failure order	total energy (J)	failure order	total energy (J)	failure order	total energy (J)
1	11.847	9	16.402	17	25.365
2	13.003	10	19.252	18	25.866
3	13.579	11	19.453	19	28.11
4	13.818	12	19.876	20	28.526
5	15.05	13	19.917	21	29.725
6	15.302	14	20.169	22	30.151
7	15.611	15	20.255		
8	15.714	16	24.643		

Table A3.18 Second stage elongation for scenario 2 and the predetermined stroke of 2.998mm

failure order	2nd stage elongation (mm)	failure order	2nd stage elongation (mm)	failure order	2nd stage elongation (mm)
1	9.255592	9	13.08213	17	20.54636
2	10.26319	10	15.2574	18	20.95161
3	10.65288	11	15.51245	19	22.73684
4	11.06042	12	15.7132	20	23.48783
5	11.87953	13	15.90717	21	24.31281
6	12.04586	14	16.22485	22	24.53044
7	12.14347	15	16.27625		
8	12.30384	16	19.78094		

Table A3.19 Second stage toughness for scenario 2 and the predetermined stroke of 2.998mm

failure order	2nd stage toughness (J)	failure order	2nd stage toughness (J)	failure order	2nd stage toughness (J)
1	10.2572	9	14.7298	17	23.7646
2	11.4283	10	17.5973	18	24.281
3	11.9634	11	17.8697	19	26.5372
4	12.2041	12	18.224	20	26.9695
5	13.4642	13	18.2696	21	28.1293
6	13.6633	14	18.5857	22	28.6022
7	14.0141	15	18.6497		
8	14.1233	16	23.0568		

Table A3.20 Total elongation for scenario 2 and the predetermined stroke of 3.432mm

failure order	total elongation (mm)	failure order	total elongation (mm)	failure order	total elongation (mm)
1	13.35514	8	17.18789	15	24.36631
2	14.59449	9	17.41679	16	24.57571
3	14.9178	10	18.50116	17	25.23091
4	14.9541	11	21.0522	18	26.55145
5	14.97152	12	21.3196	19	26.59066
6	15.61759	13	21.523	20	27.90137
7	16.41766	15	22.97493	21	35.49294

Table A3.21 Total energy for scenario 2 and the predetermined stroke of 3.432mm

failure order	total energy (J)	failure order	total energy (J)	failure order	total energy (J)
1	16.177	8	20.391	15	29.564
2	17.705	9	20.821	16	30.038
3	17.722	10	22.446	17	30.298
4	17.874	11	24.858	18	31.522
5	18.105	12	25.991	19	32.341
6	18.696	13	26.076	20	33.91
7	19.663	15	27.31	21	42.767

Table A3.22 Second stage elongation for scenario 2 and the predetermined stroke of 3.432mm

failure order	2nd stage elongation (mm)	failure order	2nd stage elongation (mm)	failure order	2nd stage elongation (mm)
1	12.28456	8	16.1577	15	23.30864
2	13.55577	9	16.35349	16	23.5332
3	13.88696	10	17.43895	17	24.17776
4	13.90334	11	19.96671	18	25.51155
5	13.91686	12	20.27037	19	25.5296
6	14.57629	13	20.4587	20	26.85597
7	15.3409	15	21.93888	21	34.44654

Table A3.23 Second stage toughness for scenario 2 and the predetermined stroke of 3.432mm

failure order	2nd stage toughness (J)	failure order	2nd stage toughness (J)	failure order	2nd stage toughness (J)
1	13.9034	8	17.4019	15	27.3147
2	15.4769	9	18.2214	16	27.7505
3	15.5061	10	20.1926	17	28.0591
4	15.5831	11	22.6354	18	29.3134
5	15.6498	12	23.7134	19	30.0989
6	15.8292	13	23.8182	20	31.6541
7	16.4749	15	25.0963	21	40.5582

Table A3.24 Total elongation for scenario 2 and the predetermined stroke of 6mm

failure order	total elongation (mm)	failure order	total elongation (mm)	failure order	total elongation (mm)
1	7.408214	10	15.13706	19	21.42921
2	7.989113	11	15.78058	20	21.63443
3	10.67399	12	17.02187	21	23.59611
4	10.76922	13	17.651	22	26.7046
5	12.20426	14	19.93676	23	28.25987
6	14.34993	15	20.15165	24	28.73548
7	14.74184	16	20.15603	25	31.65313
8	14.84864	17	20.47836	26	32.41518
9	15.09692	18	21.20758		

Table A3.25 Total energy for scenario 2 and the predetermined stroke of 6mm

failure order	total energy (J)	failure order	total energy (J)	failure order	total energy (J)
1	9.3537	10	19.009	19	26.412
2	10.101	11	19.451	20	26.629
3	13.042	12	21.394	21	29.017
4	13.453	13	21.877	22	32.732
5	14.971	14	24.629	23	34.278
6	17.526	15	24.775	24	35.38
7	17.732	16	24.795	25	38.149
8	18.397	17	25.485	26	39.477
9	18.617	18	25.757		

Table A3.26 Second stage elongation for scenario 2 and the predetermined stroke of 6mm

failure order	2nd stage elongation (mm)	failure order	2nd stage elongation (mm)	failure order	2nd stage elongation (mm)
1	4.47607	10	12.16896	19	18.52713
2	5.045163	11	12.84288	20	18.69058
3	7.655111	12	14.0731	21	20.66496
4	7.802237	13	14.6631	22	23.80362
5	9.25201	14	16.99089	23	25.29434
6	11.40113	15	17.21698	24	25.80726
7	11.795	16	17.22439	25	28.79135
8	11.92667	17	17.55527	26	29.51853
9	12.14567	18	18.24023		

Table A3.27 Second stage toughness for scenario 2 and the predetermined stroke of 6mm

failure order	2nd stage toughness (J)	failure order	2nd stage toughness (J)	failure order	2nd stage toughness (J)
1	3.7708	10	13.3854	19	20.9026
2	4.5024	11	13.9246	20	21.1061
3	7.5809	12	15.7372	21	23.4954
4	7.868	13	16.3001	22	27.2082
5	9.4794	14	19.1326	23	28.8007
6	12.1641	15	19.198	24	30
7	12.2617	16	19.2694	25	32.7194
8	12.8481	17	19.8896	26	33.9399
9	13.0927	18	20.2638		